Towards Quantum gas microscope for ^{87}Rb^{133}Cs Molecules

Apichayaporn Ratkata

This thesis reports on a new apparatus for a quantum gas microscope for ultracold molecules to study dipolar physics in lattices. The setup is capable of creating two species of quantum degenerate bi-alkali molecules in the absolute ground state: ^{87}RbCs and KCs.

We describe the setup of vacuum chambers, magnetic coils and laser systems to produce Bose-Einstein condensates (BEC) of Cs and Rb. We start with an optimisation of the Cs BEC. A cold sample is prepared with a two-dimensional magneto-optical trap (2D-MOT$^+$) which is then loaded to form a three-dimensional MOT (3D-MOT) in a separated "main" chamber. Next, we compress the 3D-MOT to increase the density and further cool and polarise atoms using 3D degenerate Raman sideband cooling (dRSC). Then, to increase the phase-space density (PSD) to reach quantum degeneracy we employ evaporative cooling by loading the atomic cloud into a a large volume dipole trap (reservoir trap) followed by a tighter dipole trap (dimple trap).

Then, we demonstrate the laser system that combines two wavelengths for Cs and Rb Raman lattice on one optical fiber for each path of the lattice light. The Rb lattice light is generated using an injection locking technique to yield adequate power. We investigate two methods to stabilise the laser frequency which are digital beat locking using an optical phase-lock loop and off-resonance frequency locking using the Faraday effect. The latter method is ultimately implemented because it has the potential to stabilise the frequency far from the transition up to 19 GHz.

Finally, we utilise the Cs BEC to perform a measurement of the tune-out wavelength at 880 nm. We measure the polarisability as a function of wavelength using Kapitza-Dirac scattering of the Cs BEC exposed by a pulse of a one-dimensional optical lattice.

The next steps to make the lowest vibrational ground-state molecules will carry on from the work presented in this thesis. Those are optical transport of the two-species atomic clouds from the main chamber to the science cell, magnetoassociation and stimulated Raman adiabatic passage.

Towards Quantum gas microscope for ^{87}Rb^{133}Cs Molecules

Apichayaporn Ratkata

A thesis submitted in partial fulfilment
of the requirements for the degree of
Doctor of Philosophy

Department of Physics
Durham University

October 2024

Contents

Page

Abstract **i**

Contents **ii**

List of Figures **iv**

List of Tables **vi**

Declaration **vii**

Acknowledgements **viii**

1 Introduction **1**
- 1.1 Why ultracold molecules? . . . 1
- 1.2 Overview of Bose-Einstein condensate (BEC) . . . 2
- 1.3 Feshbach resonances . . . 3
- 1.4 Outline of the thesis . . . 5
- 1.5 Contributions of the Author . . . 5
- 1.6 Publications . . . 6

2 Experimental Setup **7**
- 2.1 Experimental Overview . . . 7
- 2.2 Vacuum system . . . 9
  - 2.2.1 $2D^+$-MOT chamber . . . 9
  - 2.2.2 Main chamber . . . 11
  - 2.2.3 Science cell . . . 12
- 2.3 Magnetic field generation . . . 18
  - 2.3.1 2D-MOT coils . . . 20
  - 2.3.2 Main chamber . . . 21
- 2.4 Laser systems for cooling and trapping . . . 23
  - 2.4.1 Cs laser system . . . 23
- 2.5 Diagnosis and Detection . . . 24
  - 2.5.1 Absorption imaging . . . 24

3 Characterisation of Laser cooling **29**
3.1 Realisation of the 2D$^+$-MOT 29
3.1.1 Optical setup 30
3.1.2 Optimisation 32
3.2 3D-MOT 33
3.2.1 Optimisation 33
3.3 Compressed-MOT 36
3.3.1 Optimisation 36

4 Degenerate Raman Sideband Cooling **38**
4.1 Cooling mechanism of Degenerate Raman sideband cooling . . 39
4.2 Experiment in 3D lattice for Cs 42
4.2.1 Laser system 43
4.2.2 Optimisation procedures and results 44
4.3 Experiment in 3D lattice for ^{87}Rb 48
4.3.1 Two-color lattice laser system 51
4.3.2 Laser frequency stabilisation for master laser 52

5 Bose-Einstein condensate of Cs in an optical dipole trap **61**
5.1 Evaporative cooling in an optical dipole trap 61
5.1.1 Reservoir trap 61
5.1.2 Magnetic Levitation 64
5.1.3 Dimple trap 64

6 Measurement of the tune-out wavelength for ^{133}Cs at 880 nm **65**
6.1 Motivation 66
6.2 Theory 68
6.2.1 Polarisability 68
6.2.2 Kapitza-Dirac Scattering 71
6.3 Overview of the apparatus and BEC production 73
6.4 Analysis of results 78
6.4.1 Corrections to Measurements 79
6.4.2 Ratio of Matrix Elements 80
6.5 Summary and Outlook 81

List of Figures

Figure Page

1.1 Illustration of a Feshbach resonance 4

2.1 A summary of the cooling and trapping procedures for the production of Cs and ^{87}Rb Bose-Einstein condensates 8
2.2 Vacuum chamber overview 10
2.3 Overview of the 2D$^+$-MOT chamber 12
2.4 Schematic of a main chamber 13
2.5 Optical transimission profiles for AR-coated viewports of the main chamber 15
2.6 Theoretical coating performance of the ColdQuanta AR coating of the science cell 17
2.7 Simulation of electric fields in the science cell 19
2.8 A cross-section of the main chamber 21
2.9 Schematic of hyperfine structures of ^{87}Rb and cs. 26
2.10 Overview of laser system for Cs and ^{87}Rb 27

3.1 Schematic of 2D$^+$-MOT 31
3.2 Optical layout of the 2D$^+$-MOT 32
3.3 Dependence of the fluorescence light level associated with atom number of the 3D-MOT on the 2D-MOT cooling detuning 33
3.4 Optimisation of the shim field for the 3D-MOT 34
3.5 Optimisation of push beam's parameters 34
3.6 Optimisation of the cooling and repumping light 35
3.7 Optimisation of the cooling and repumping light in the cMOT phase 36
3.8 Optimisation of the magnetic field gradient and cooling detuning 37

4.1 Schematic of Degenerate Raman sideband cooling for ^{133}Cs . 41
4.2 Experimental setup of DRSC 43
4.3 Absorption images of ^{133}Cs 46
4.4 Dependence of trapped atoms on the lattice alignment and the polarisation of the incoming standing wave 46
4.5 Stern-Gerlach imaging 47
4.6 Optimisation of polariser parameters 48
4.7 Optimisation of lattice duration 49

4.8 Summary of energy levels and relevant frequencies for dual-species DRSC 50
4.9 Schematic of optics used for the two-color DRSC lattice light . 53
4.10 Simplied layout of digital beat locking using an optical phase-lock loop (OPLL) 54
4.11 Error signal derived from the digital-beat locking 55
4.12 frequency stability of the slave laser 56
4.13 Simplified layout of off-resonance frequency locking using the Faraday effect 58
4.14 Temperature dependence of the Faraday signals 59
4.15 Long-term frequency stability using the Faraday effect 60

5.1 Experimental sequence for the formation of a Cs BEC. 63

6.1 Calculated scalar polarisability of ground state Cs in the vicinity of the D_1 and D_2 transitions 70
6.2 Schematic of the apparatus highlighting the optical beam layout 74
6.3 Schematic of the apparatus for the preparation of the lattice light 75
6.4 Example of a Kapitza-Dirac measurement 77
6.5 Trap depth measurements using Kapitza-Dirac scattering . . . 78

List of Tables

2.1 Description of the viewport coatings and the relevant beams . 14
2.2 Proposed specification of the AR coating of the science cell . . 16
2.3 Summary of coil characterisation 22
2.4 Summary of detunings of Cs laser beams 25

3.1 Summary of optimal experimental parameters for ^{133}Cs laser cooling 35

6.1 Theoretical contributions to the $6S$ scalar polarisability of Cs at $\lambda_0^{th} = 880.2456$ nm 82

Declaration

I confirm that no part of the material offered has previously been submitted by myself for a degree in this or any other University. Where material has been generated through joint work, the work of others has been indicated.

Apichayaporn Ratkata

Durham, October 2024

Acknowledgements

I would like to thank everyone who have supported me and contributed to the project over my PhD period. First of all I am grateful for my supervisor Simon Cornish who explain key concepts of atomic, molecular and optical physics that are fundamental principles to build up our experiment and give me constructive advice on how to develop, organise, and achieve each measurement logically. I deeply appreciate all suggestions and feedback on my work.

I must thank all of talented colleagues in the Microscope lab for their contributions to the project from the beginning. Thank you for answering my questions and sharing their experimental techniques. In particular I would like to thank Sarah Bromley who leads and dedicates herself to the microscope project. Owing to her expertise in atomic experiments, she teaches me how to properly set up a laser system for lattice lasers and optimise the experiments. More importantly, she supports me in carrying out the measurement of a Cs tune-out wavelength during the pandemic lockdown. Also, I thank Philip Gregory, Danielle Pizzey, and Elizabeth Bridge who involve in vacuum chamber and microscope designs. I am grateful for Lewis McArd who designs and builds magnetic coils and patiently give me advice on magnetic field characterisations. I thank to Alex Alampounti for his help with a home-built laser. My thanks also go to all fellow PhD students Andrew Innes, Jonathan Mortlock, and Jonas Matthies for sharing their thoughts, enthusiasm and hard work in both theory and experiment. I would like to express my deep sense of gratitude to everyone for their feedback on this thesis.

I am grateful for everyone in Cornish's group: Alexander Guttridge, Kali Wilson, Oliver Wales, Jacob Blackmore, Stephan Spence, Vincent Brooks for sharing their knowledge and suggestions and enjoying the cake club. Moreover, I am pleased to be part of QLM group that have provided a supportive atmosphere to work and discuss. My work could not have been finished without the staff in the Durham physics department, those in financial and administrative support and in the mechanical and electronic workshops in particular Stephan Lishman, and Andrew Hunter.

Thank you to the Thai government for funding the DPST scholarship for my PhD research.

I have enjoyed my life in Durham over the years because of my friends and fantastic housemates. Thank you to Nawapon, Nipada, Ting, Wanchalerm and Supanat for their laughter, wonderful meals, exciting trips, and deep conversation in life.

Last but not least, the largest thanks must go to my family. I need to express my deep sense of gratitude to dad, mom, sister and my niece for their love and emotional support that heals me when being far apart across a continent.

Chapter 1

Introduction

Ultracold dipolar molecules offer to study a wide range of applications, for example, ultracold chemistry [1], precision measurement of fundamental physics [2], quantum simulation [3], and many-body physics [4]. Our research aims towards quantum simulation of strongly interacting many-body quantum systems to understand high-temperature superconductivity and exotic states of quantum magnetism [5]. Ultracold molecules facilitate exploration of these magnetic phenomena since they possess a permanent electric dipole moment [6] which can be controlled in the laboratory frame via external fields and their couplings are mediated by long-range dipole-dipole interactions (DDIs).

1.1 Why ultracold molecules?

Unlike ultracold atoms, ultracold molecules offer long-range dipole-dipole interactions (V_{dd}) in addition to contact interactions (V_{c}) as shown in eq. 1.1. Dipolar interaction is also anisotropic and tunable using electric and microwave fields. Moreover, molecules have a rich of degrees of freedom accessing via their internal structure including hyperfine, rotational, vibrational, and electronic levels. A high degree of flexibility in state selection is beneficial in quantum information processing [7]. Rotational states of polar molecules are also proposed to used as a synthetic dimensions [8].

In our experiment, we aim to build a molecular microscope that enables a preparation of two candidates of heteronuclear bi-alkaline molecules and

have a capability to detect and address individual molecules in a 2D quantum array. Trapping ultracold gases of dipolar molecules in a two-dimensional optical lattice in the presence of an electric field so that they are aligned side-by-side suggests a suppression of intralayer ultracold molecules collisions. Within a single 2D layer, we may realise topological superfluid phases [7] by applying microwave fields. When considering multi layer, the dipolar interactions between molecules in different layers provides a possibility to study quantum phase transitions from superfluid to Cooper pairs [4, 9].

$$H_{\text{int}} = V_{\text{c}} + V_{\text{dd}} \tag{1.1}$$

$$= \frac{4\pi\hbar^2 a}{m}\delta(\mathbf{r}) + \frac{1}{4\pi\epsilon_0}\frac{d^2}{r^3}(1 - 3\cos^2\theta) \tag{1.2}$$

1.2 Overview of Bose-Einstein condensate (BEC)

For a gas of N atoms with in a volume V, an average atomic density (n) is determined by the number of atoms per unit volume: $n = N/V$. Therefore, the mean interatomic separation of the atomic gas is scaled as n^{-3}. Atoms in a thermal gas at temperature T can be considered as quantum-mechanical wave packets having an associated thermal de Broglie wavelength

$$\lambda_{\text{dB}} = \sqrt{\frac{2\pi\hbar^2}{mk_{\text{B}}T}} \tag{1.3}$$

where $\hbar$ is the reduced Plank constant, k_{B} the Boltzman constant and m is the atomic mass. According to the uncertainty principle ($\Delta x \Delta p \geq \hbar/2$), the de Brogile wavelength implies the uncertainty in position associated with the thermal momentum distribution if we perform a position measurement [10]. When the atoms are cooled down, the de Brogile wavelength becomes larger as the temperature associated with their kinetic energy decreases. Quantum effects emerge when λ_{dB} is comparable to the interatomic spacing and the atomic wave packets start to overlap and become indistinguishable particles [10]. At the temperature below a critical temperature (T_{c}) and the number density that satisfies the phase-space density (PSD) condition given by:

$$n_0\lambda_{\text{dB}}^3 \geq 2.612, \tag{1.4}$$

where n_0 is the peak number density, the cloud of bosonic atoms undergoes a phase transition and reach quantum degeneracy. A Bose-Einstein condensate (BEC) is formed in which all atoms occupy the same lowest single-particle state and have a common phase so it becomes a coherent matter wave and can be represented by a macroscopic wavefunction [10].

1.3 Feshbach resonances

In the low-energy regime, the interaction between two atoms in elastic collisions can be described by a single parameter: s-wave scattering length (a). Fig.1.1(a) illustrates the principle of a Feshbach resonance. Consider an open and closed channels having different magnetic moments at zero-magnetic field, at large interatomic distance the energy of each channels is the total energy of individual atoms in its hyperfine spin state $|F, m_F\rangle$. The incoming scattering state in the open channel has a small energy (E) above the dissociation threshold. A Feshbach resonance occurs when there exists a molecular bound state in the closed channel whose energy (E_{C}) can be tuned via a specific applied magnetic field and becomes degenerate with the energy of the scattering state in the open channel. This generates an avoided crossing between molecular bound and atomic scattering states as shown in fig. 1.1(c): the energy as a function of magnetic fields . The scattering length varies with the magnetic field expressed in the equation 1.3, where a_{bg} is the background scattering length in the absence of the resonance and Δ is the resonance width in magnetic field. Fig.1.1(b) shows that the scattering length tends to $\pm\infty$ at the centre of the resonance B_0 and to both positive and negative around the neighbouring fields, depending on how we sweep the magnetic field. The scattering length can also be tuned to zero when it requires to suppress the interaction. We exploits this field-dependent characteristic in many stages of cooling such as the evaporative cooling where we operate at the magnetic field associated with the moderate scattering length so that good elastic collisions dominate over bad inelastic collisions.

$$a(B) = a_{\mathrm{bg}}\left(1 - \frac{\Delta}{B - B_0}\right) \tag{1.5}$$

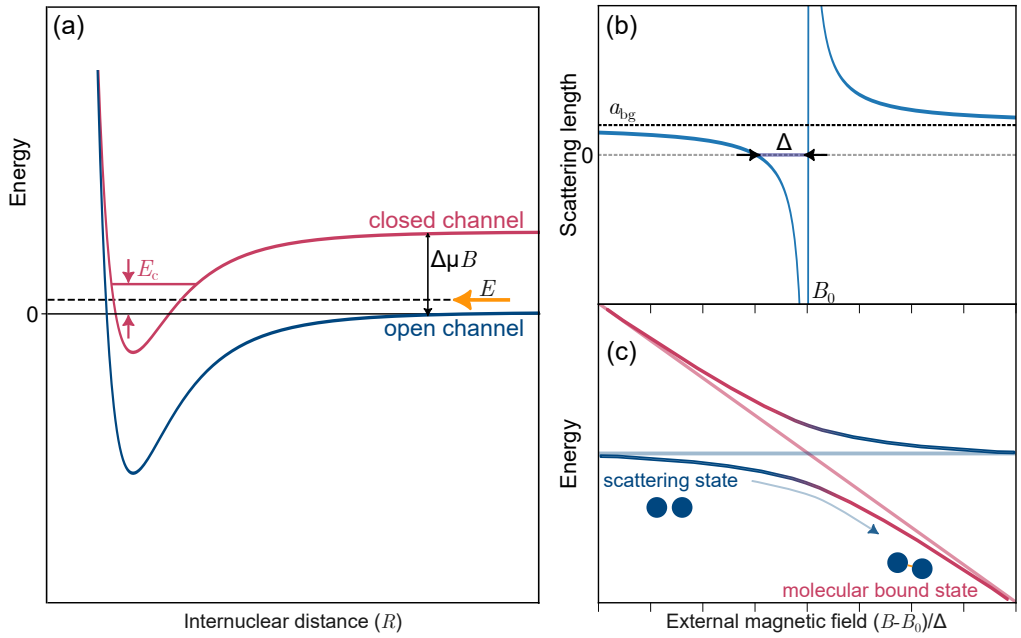

Figure 1.1: Illustration of a Feshbach resonance for two channels. (a) The potential energy curves of elastic collisions between two atoms as a function of the interatomic distance (R). The lower curve is an open (entrance) channel and the upper curve is a closed channel. Two atoms starts a collision in the scattering state with small energy (E) above the the asymptotic energy of the open-channel. This asymptotic energy is set to zero and referred as the dissociation threshold. The binding energy of a molecular bound state (E_C) supported by the closed channel can be tuned via external magnetic fields to become degenerate with the energy of the scattering state in the entrance channel. Their energy difference is due to the difference between the magnetic moment ($\Delta\mu$) of the scattering state of separated atoms and the bound state. (b) The variation of scattering lengths around a Feshbach resonance with a positive background scattering length described by equation 1.3. (c) An avoiding crossing occurs at the Feshbach resonance.

1.4 Outline of the thesis

This thesis explains an apparatus to build a quantum gas microscope for RbCs molecules. It is structured as follows:

- **Chapter 2**: The experimental apparatus and laser systems used for cooling and trapping are detailed.
- **Chapter 3**: We demonstrate optimisations of laser cooling of Cs atoms.
- **Chapter 4**: We explain Degenerate Raman sideband cooling (DRSC) and detail how to optimise this cooling technique. We present the method to stabilise the laser frequency of Rb lattice light.
- **Chapter 5**: We detail the evaporative cooling to create Bose-Einstein condensate of Cs in an optical dipole trap
- **Chapter 6**: We report the measurement of the tune-out wavelength for Cs at 880 nm.

1.5 Contributions of the Author

My previous project of creation of ultracold KCs mixtures in a single science cell [11] was merged with the microscope project so all optical and electrical apparatus were transferred to build the microscope experiment from scratch. Before I joined the team, many postdoctoral researchers have involved in vacuum chamber designs including Phil Gregory, Sarah Bromley, Lewis McArd, Danielle Pizzey, Elizabeth Bridge, and Alex Alampounti. Simon Cornish has supervised the project throughout.

The vacuum chamber of the main chamber and science cell presented in Chapter 2 were designed by Phil. The 2D-MOT chamber were designed by Dani. The vacuum assembly were mainly managed by Dani and Lewis. I

learned pumping and baking procedures from them. I involved in an alteration of new dispensers. The magnetic coils were designed by Lewis and Liz. The coils were wound by Lewis and I characterised the coils. The water cooling system for magnetic coils were connected by Lewis and myself. The laser systems were designed and constructed by Sarah. The optimisation Cs MOTs presented in Chapter 3 were carried out by Sarah. The optimisations of the DRSC of Cs were done by Sarah and myself. The laser system for frequency stabilisation of Rb lattice light used in the DRSC step presented in Chapter 4 was designed, constructed, and characterised by myself. The lattice light delivered by a Ti:Sapphire laser was prepared by myself. The laser layout for generating a one-dimensional lattice used for Kapitza-Dirac scattering on the experimental table was setup by Sarah and myself. The measurement data of the tune-out wavelength presented in Chapter 5 was carried out by Sarah which occurred during the national lockdown. I was responsible to do the analysis from home. Theory support for the transition matrix elements which are important to determine the error of the tune-out wavelength was provided by Marianna S. Safronova.

1.6 Publications

The following publication has reported from the work presented in this thesis:

Measurement of the tune-out wavelength for ^{133}Cs at 880 nm
A. Ratkata, P. D. Gregory, A. D. Innes, A. J. Matthies, L. A. McArd, J. M. Mortlock, M. S. Safronova, S. L. Bromley, and Simon L. Cornish

Phys. Rev. A 104, 052813 (2021)

Chapter 2

Experimental Setup

2.1 Experimental Overview

This chapter describes the experimental apparatus needed for a molecular microscope that integrates three alkali-metal atomic species: Cs, Rb, and K. Our project aims to investigate a route towards the flexible production of two kinds of ultracold molecule: KCs or RbCs. Creating high phase-space density atomic mixtures is the first step towards this goal. Of the three atomic species, Cs is the most complicated to condense as the lowest ground state is a high-field seeking state, thus magnetically untrappable. For this reason, the cooling and trapping strategy and design of the apparatus is based around Cs. Our plan is then to integrate the other two species into a similar scheme. For Rb we can also implement three-dimensional degenerate Raman sideband cooling (DRSC). For K our strategy will be to use sympathetic cooling in a bichromatic potential.

To begin with Cs, there are many groups worldwide have demonstrated production of Cs Bose-Einstein condensates [12–16]. In our experiment, we follow the well-established route [12, 13] developed in the pioneering group of Nägerl in Innsbruck, although a different method is used to generate the cold atomic source. Fig. 2.1 shows the procedure to achieve Cs BECs. We exploit the $2D^+$-MOT [17] to create an intense slow atomic beam, that facilitates the fast loading of the 3D-MOT in another chamber. Then, further cooling of Cs atoms is performed using a compressed-MOT, optical molasses and DRSC.

After that, atoms are transferred into a large volume optical dipole trap, namely the reservoir trap, for phase space matching, followed by a tightly confined dipole trap, namely the dimple trap, to increase the phase-space density. Finally, efficient evaporative cooling is carried out in the dimple trap to reach quantum degeneracy.

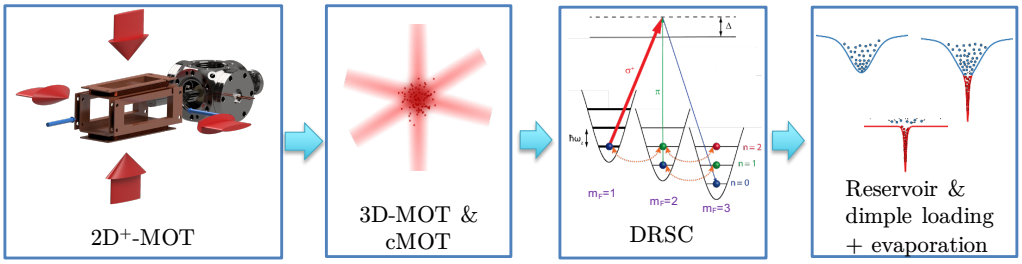

Figure 2.1: A summary of the cooling and trapping procedures for the production of Cs and Rb Bose-Einstein condensates (adapted from [16]). A 2D$^+$-MOT offers fast loading of cold atomic beam. Then, the atoms are captured in the 3D-MOT. Following this, further cooling techniques are performed: compressed MOT and DRSC. After that the atomic cloud is transferred to the reservoir trap followed by transfer to the dimple trap. Evaporation is carried out in the dimple trap to achieve BEC.

To follow this cooling strategy to create quantum degenerate gases, the atomic gases need to be isolated from the laboratory environment. This is achieved by keeping them under ultrahigh vacuum (UHV) conditions. The vacuum apparatus is designed to have multiple chambers where the atomic source and laser-cooling of the atoms can be performed in a separate chamber from the optical lattice, high resolution imaging and molecule production.

The experimental setups are divided into two optical tables. The first table, referred to as the "laser table", houses the laser systems for the early-stage laser-cooling and imaging of all three species. On the laser table, the frequency stabilisation is carried out using atomic spectroscopy in vapour cells. The different frequencies, hence detunings at each cooling stage are generated by acousto-optic modulators (AOMs). The light is coupled into polarisation-maintaining single-mode optical fibres and transported over to the main experiment. The light intensity is controlled by the RF power to the AOMs, as well as optical shutters via a LabVIEW experimental control

software. The second table, referred to as the "main experimental table", has the vacuum system, the magnetic field coil system, and the optical trapping laser systems.

The structure of the remainder of this chapter is as follows. Sec. 2.2 presents the complete vacuum system. Sec. 2.3 describes in detail how we generate the magnetic fields needed for all the cooling stages. Sec. 2.4 outlines the laser systems for trapping and cooling Cs and Rb in particular. Sec. 2.5 explains how we detect and measure the atomic gases using fluorescence imaging and absorption imaging.

2.2 Vacuum system

The vacuum apparatus shown in Fig. 2.2 consists of four chambers with two sections at different vacuum levels connected via differential pumping tubes. Two of the chambers in the high vacuum (HV) regime require a large vapour pressure to generate slow atomic beams in the 2D magneto-optical traps (MOTs): one is for Cs and the other is for Rb and K. Then, atoms are further cooled and trapped in the ultra high vacuum (UHV) regime in the "main chamber", where the collisions with background gas are suppressed to prevent atom loss. Finally, the ultracold atoms are transported to the AR coated "science cell", loaded into the optical lattice and associated into molecules. A multi-element microscope objective lens with a large numerical aperture of 0.7 is mounted below the cell to allow imaging and addressing of the molecules with single-site resolution and, ultimately, to observe quantum phases associated with polar molecules in optical lattices.

2.2.1 2D$^+$-MOT chamber

The 2D$^+$-MOT chamber is shown in Fig. 2.3. It consists of a spherical cube (Kimball Spherical cube MCF275-SphCube-C6) mounted on the customized mount with a spacer for tilting the atomic beam by 2 degree to counteract the influence of gravity. A cuboid glass cell, where the 2D+-MOT takes place, from Precision Glassblowing is connected to one side of the cube. There is an all-metal valve in conjunction with an up-to-air valve attached at the

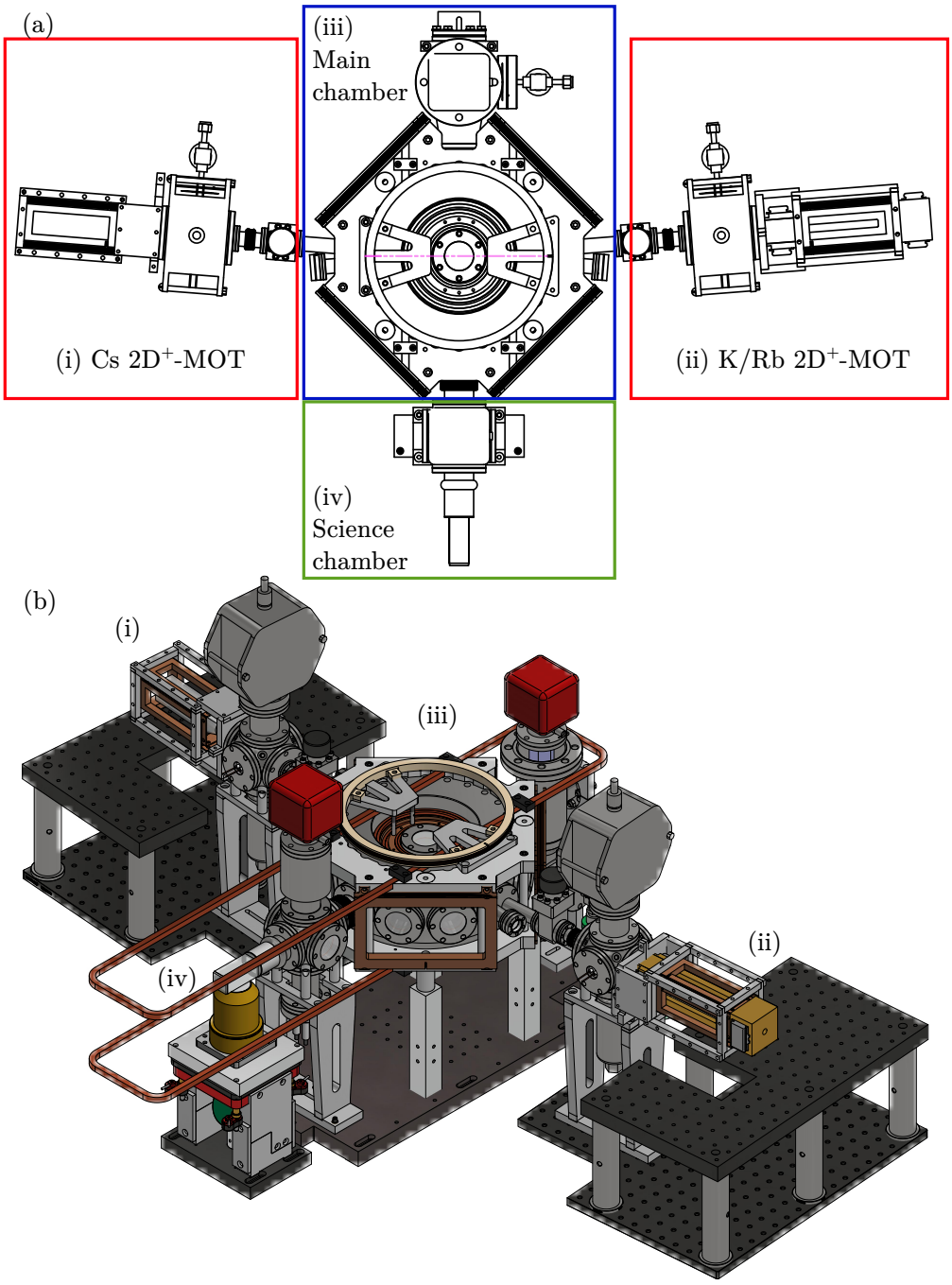

Figure 2.2: Vacuum chamber overview. (a) A top view schematic of the whole vacuum apparatus comprising of four sections: (i) $2D^+$-MOT chamber for Cs, (ii) $2D^+$-MOT chamber for K and Rb, (iii) the main vacuum chamber, and (iv) the science chamber. (b) A side view 3D drawing of the chambers illustrates additional pumps in each chamber and magnetic coils. A pair of long rectangle coils, namely racetrack coils, is used to transport the ultracold atomic clouds to the science chamber. A microscope is set up in the science chamber section (iv).

bottom of the spherical cube. These valves, together with roughing and turbo pumps, allow us to perform standard vacuum pumping procedures to reduce the pressure from atmospheric pressure into the pressure to the order of 10^{-8} mbar. A 10 L/s pump (Vaclon from Agilent Technologies) is connected at the top of the spherical cube for pumping in the HV regime. The alkali-metal atomic gases are released from AlfaVakuo dispensers: two for Cs (AS-CsBi25-0100-3F) in one of the 2D-MOT chambers; and 1 Rb (AS-RbBi40-0100-3F) and 1 K (AS-KBi40-0100-3F) in the other. They are held inside the spherical cube by two MACOR discs, connected by M3 studding, vented washers and nuts (see Fig. 2.3). The dispensers are spot-welded onto two two-pin electrical feedthroughs (Lesker EFT0123052). The HV section of the $2D^+$-MOT chamber is connected to the UHV section of the main chamber via a differential pumping tube. A 45 degrees polished stainless steel mirror with a 1-mm aperture is attached at the end of the tube. The mirror is polarisation-dependent where the circularly polarised light is reflected by 67%. Flexible edge-welded bellows facilitate the alignment of the 2D MOT chamber to the center of the main chamber and reduce the mechanical stress on a flange of a gate valve. Gate valves separate the HV sections from the UHV section and therefore allow us to bake the sections separately.

2.2.2 Main chamber

For multi-species experiments, the main vacuum chamber requires a lot of optical access as shown in Fig. 2.4. Our experiment uses a 10-inch spherical dodecagon vacuum chamber from Kimball Physics, made out of non-magnetic stainless steel. Eight of the flanges along the horizontal plane of the chamber and the two on top and bottom attach to CF40 viewports with different anti-reflection (AR) coatings optimised for particular wavelength ranges. Consequently, this needs an appropriate plan for beam paths required for laser cooling and optical dipole trapping. Table 2.1 summarises the viewport coatings and the associated suppliers, along with the usage of each port of the chamber. The specification of the AR coatings is characterised via optical transmission profiles shown in Fig. 2.5. For the other two horizontal flanges (no. 3 and 9), customised DN40 - 2xDN16 adapters are attached. One of

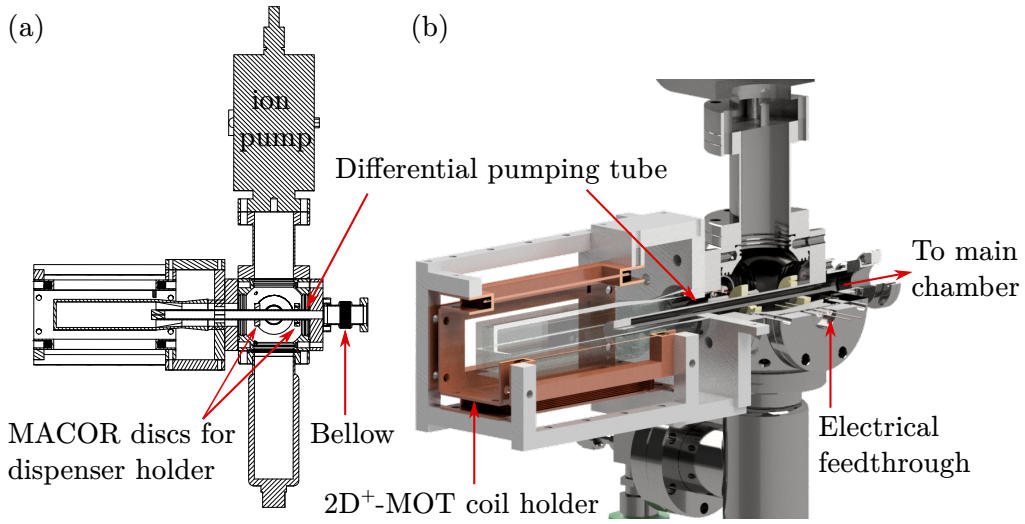

Figure 2.3: A cross-cut overview of the $2D^+$-MOT chamber. (a) A CAD drawing shows a dispenser holder and a connection between a differential pumping tube and a bellow, which is then attached to the gate valve. (b) A 3D drawing shows an additional coil mount around the cell and the electric feedthrough.

these DN16 flanges is connected to the gate valve connecting to the 2D MOT chamber and the other is for MOT fluorescence imaging. The flange no. 12 is connected with a custom elbow chamber for an optical transport access. In addition, the NexTorr pump, which is the ion pump combined with NEG, is connected to the chamber via a zero length DN40 - DN63 reducer. The flange no. 6 is connected to the bellow and the a spherical cube (Kimball DN40 Cube MCF275-SphCube-C6) inthe science cell section.

2.2.3 Science cell

The final chamber is an anti-reflection (AR) coated fused silica glass cell with outer dimension of $2.5 \times 2.5 \times 3$ cm^3. Each surface of the glass cell is 3 mm thick to avoid bowing when under vacuum, which is important for the high resolution imaging. We refer to this glass cell as the "science cell", where we aim to perform molecular quantum gas microscopy to detect the effect of long-range dipole-dipole interactions between individual molecules in an optical lattice. Therefore, the requirement of AR coatings of each glass surface are

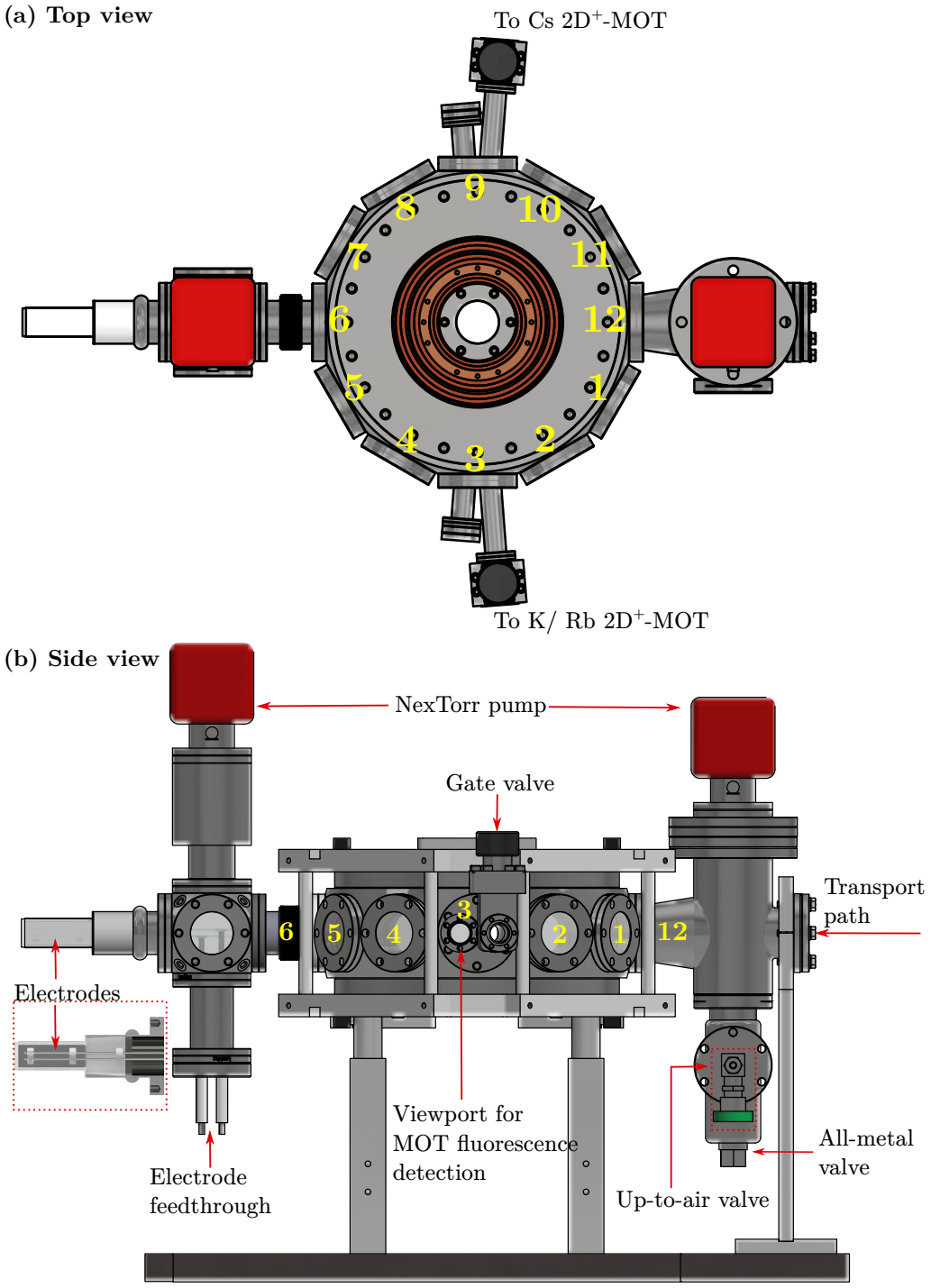

Figure 2.4: (a) A top view schematic of a main chamber. All flanges in the horizontal direction are numbered such that they can be referenced in Table 2.1. (b) A side view schematic of a main chamber in conjunction with the science cell.

Flange	Viewport coating	Beams or Connection
1	LaserOptik	Reservoir trap, absorption imaging
2	LaserOptik	MOT, Raman lattice
3	—	K/ Rb Gate valve, K/ Rb Fluorescence imaging
4	LaserOptik	Reservoir trap
5	VP5	MOT, Raman lattice
6	—	to a spherical cube with electrode holders
7	LaserOptik	Reservoir trap, absorption imaging
8	VP8	MOT, Raman lattice
9	—	Cs Gate valve, Cs Fluorescence imaging
10	LaserOptik	Reservoir trap
11	VP11	MOT, Raman lattice
12	—	to NexTorr pump
Top	LaserOptik	MOT, Raman lattice, polariser
Bottom	LaserOptik	MOT, Raman lattice

Table 2.1: Description of the viewport coatings and the relevant beams accessing each port around the main chamber. Corresponding optical transmission profiles of all viewport coatings in the second column are shown in Fig. 2.5 as a function of wavelength from 200 - 1600 nm.

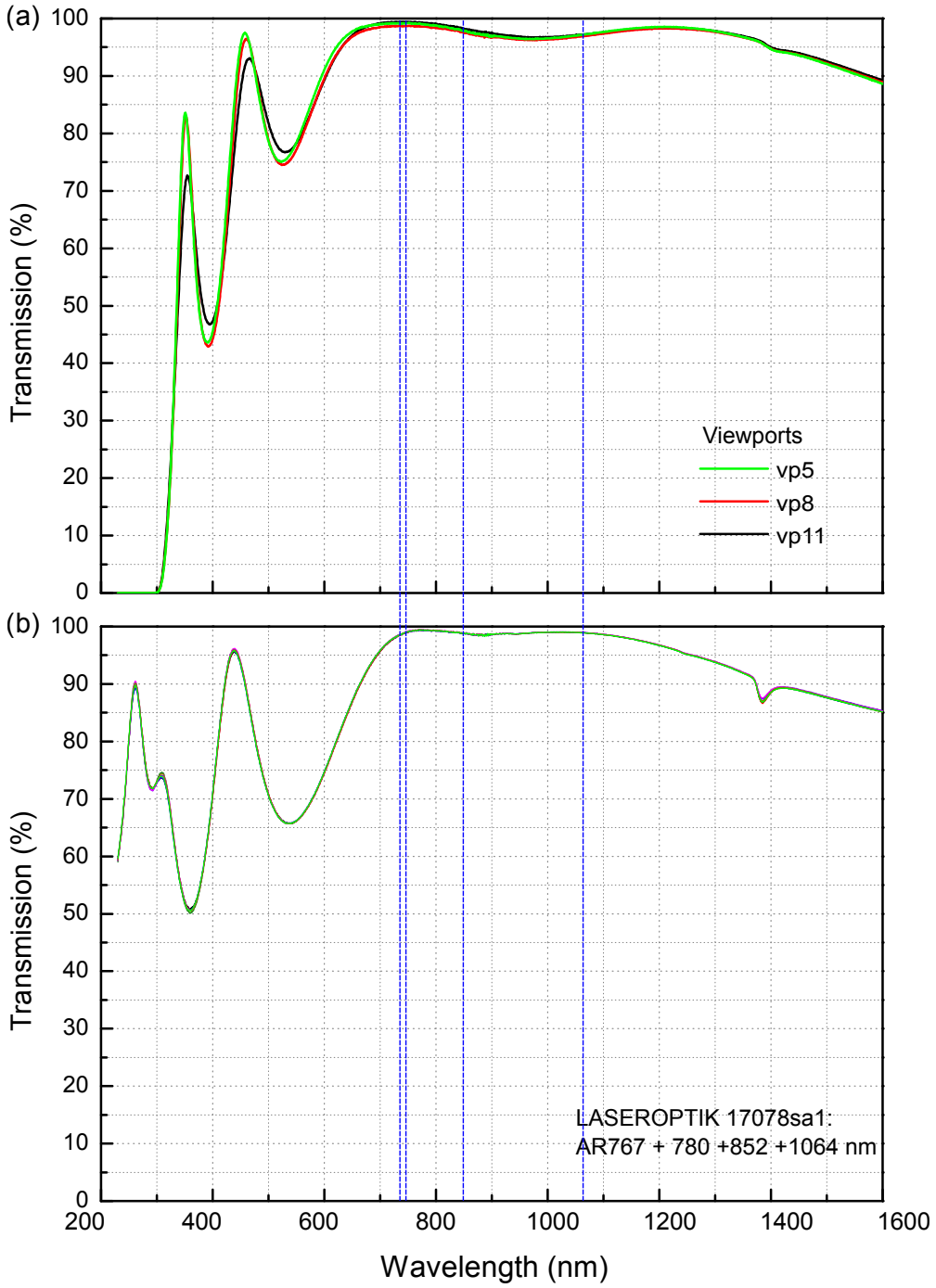

Figure 2.5: A measurement of optical transimission profiles for AR-coated viewports of the main chamber. (a) Characterisation of viewports that attach to flange 5, 8, and 11 and transmit the MOT and Raman beams. (b) Characterisation of viewports from Laseroptik that attach to the rest of the flanges. The blue dashed vertical lines indicate the wavelengths of resonant light and optical trapping light, i.e. 767, 780, 852, and 1064 nm, respectively.

specified according to the relevant wavelengths for cooling, imaging, and trapping of three species, corresponding to 767, 780, 852, and 1064 nm. Table 2.2 summarises the specifications of the AR coatings we requested that the cell manufacturer, ColdQuanta, deliver. The characteristic performance of the coatings at 0°and 45° angle of incidence (AOI) are shown in Fig. 2.6. Interestingly, the reflectivity of the 1064 nm light, which is used to generate a 3D-lattice, at 45°AOI is significantly out of the requested range, more than 1 %. As a consequence, one of the lattice axis is limited to be aligned along the length of the cell, which is along the transport path. This could make an impact on the stability of the lattice due to a long total distance of lattice beam propagation.

Species	Wavelength (nm)	Angle of incidence (AOI) (degree)	Reflectivity (%)
^{39,41}K	767	±10°	< 0.2
		±10 - 45°	< 0.8
^{87}Rb	780	±10°	< 0.1
		±10 - 45°	< 0.5
Cs	852	±10°	< 0.2
		±10 - 45°	< 0.8
Optical lattice	1064	±10°	< 0.2
Dipole trap	790	±10°	< 0.5
	795	±10°	< 0.5

Table 2.2: The proposed specification of the AR coating per surface sent to ColdQuanta prior to the manufacture of the UHV cell. It mainly aims to achieve the best optical transmission, i.e. minimise the reflectivity.

In-vacuum electrodes

The uniformity of the electric field over the region of the diatomic molecules is critical to observe resonant dipole-dipole interactions across the lattice. We need to put electrodes for generating electric fields in vacuum to minimise charge build up on the wall of the science cell due to its dielectric properties. As analysed in [18], we implement an array of 4 in-vacuum electrodes which

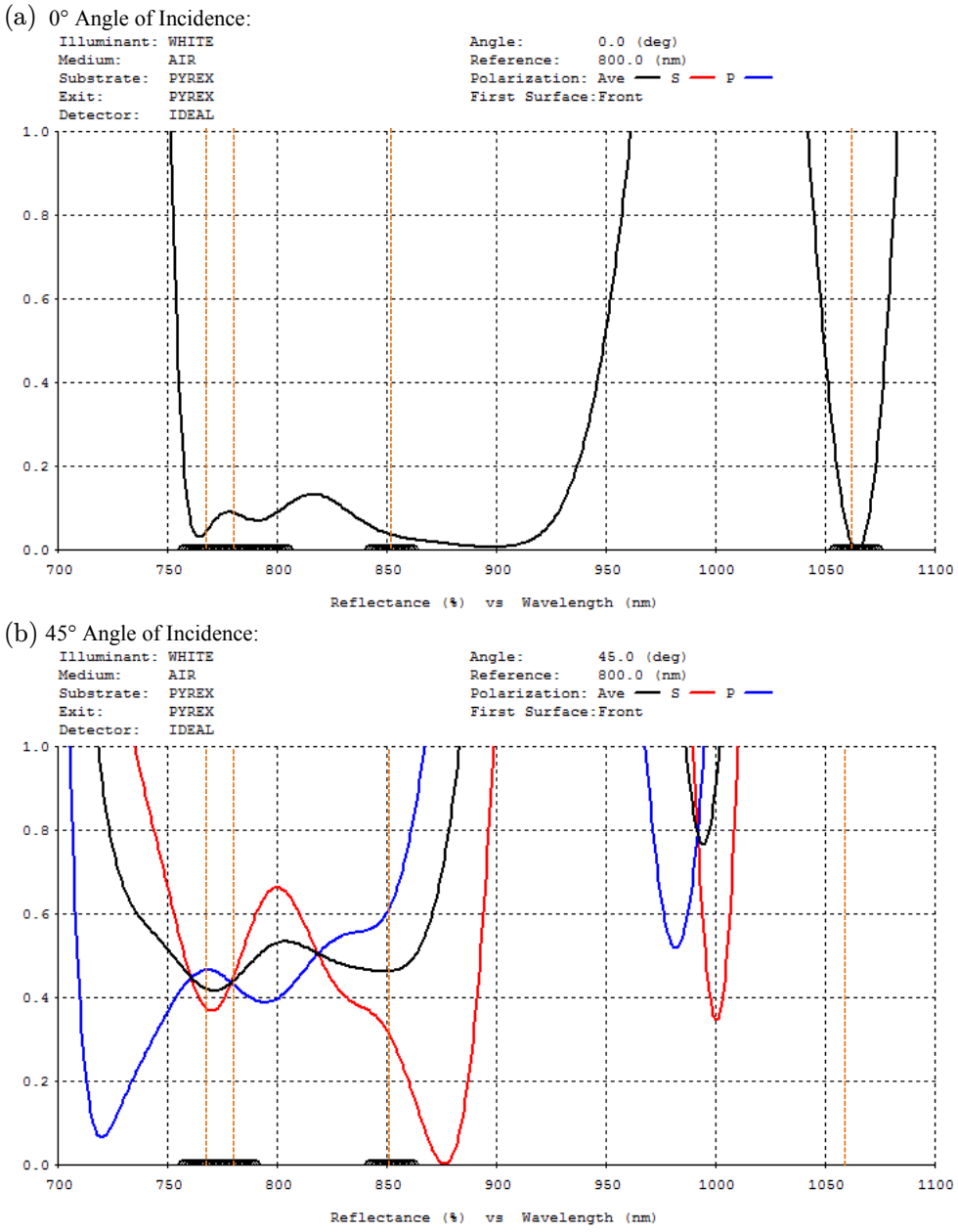

Figure 2.6: Theoretical coating performance of the ColdQuanta AR coating of the science cell per surface at (a) 0 °and (b) 45°angle of incidence. The orange dashed lines indicate the wavelengths of interest: 767, 780, 852, and 1064 nm.

can be used to generate a uniform electric field in the plane of the lattice with full control of dipole moment's strength. Full analysis of the effect of the electric fields on trapped molecules from [18] shows that the curvature of the electric field diminishes the total confining potential at molecular samples and hence must be eliminated. However, it is unfeasible that two curvatures along the vertical and horizontal directions are simultaneously minimised using just four electrodes [18]. Fig. 2.7(a) considers electrode rods extending in the y direction and they are arranged in the $x-z$ plane with a horizontal and vertical spacing of $2l_1$ and $2l_2$, respectively. Fig. 2.7 demonstrates that the ratios of the curvature to magnitude of the horizontal fields, $E_{2,v}/E_{0,v}$ normalised by the vertical electrode spacing l_2, vary with the vertical to horizontal electrode spacing ratio l_1/l_2. Our electrode configuration is chosen such that the curvature of the horizontal field is zero, i.e. spacing ratio $l_1/l_2 = 1.71$. The 2 mm diameter electrode rods each have a length of 205 mm with horizontal and vertical spacing of $2l_1 = 0.96$ cm and $2l_2 = 0.56$ cm, respectively. The inset illustrates the simulation of the electric field within the science cell, in particular being produced in the same plane as an inter-molecular axis. Quantitatively, we can produce the electric field value of 1.5 kV cm^{-1} at molecules by applying potential $V = \pm$ 5 kV to the electrodes, i.e a potential difference of 10 kV. The "X" in Fig. 2.7(a) inset represents the centre of the cell which is the location of the molecular sample. Fig. 2.7(b) - (d) show the magnitude of the electric field, the gradient and the curvature of the electric field in $x-z$ plane through the centre of the science cell. The background electric field is homogeneous over the area of 0.5×0.5 cm^2. It confirms that the curvature of the vertical field is minimised to zero with small residual curvature of the horizontal field.

2.3 Magnetic field generation

Fast and precise control over magnetic fields is required for the manipulation of ultracold atoms. For instance, at the MOT stage it is important to generate a quadrupole field, providing a magnetic field gradient in which a zero magnetic field overlaps with the location of beams' intersection to achieve a spatially dependent trapping force. The magnetic field gradient can also

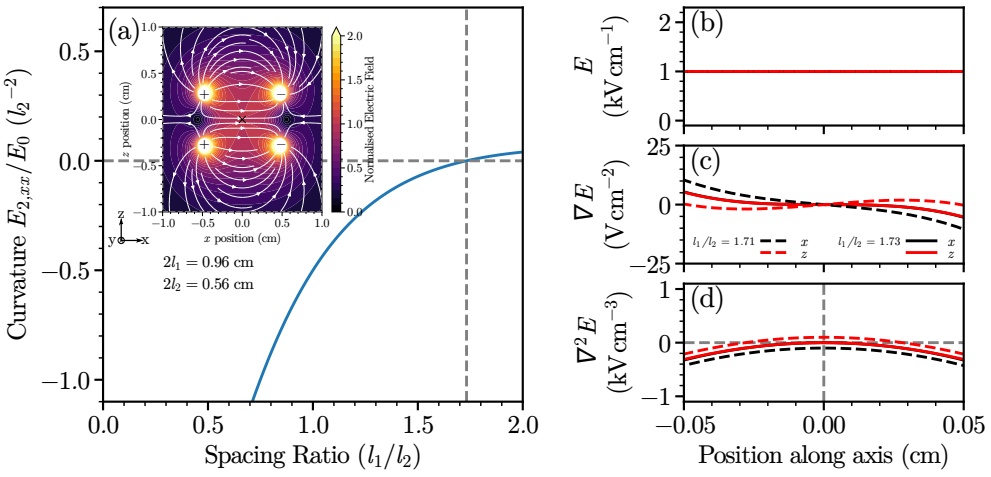

Figure 2.7: (a) Curvature-to-magnitude ratios of electric field in the case of four infinite long rods in the y-direction. The horizontal and vertical spacing for the electrodes are $2l_1$ and $2l_2$, respectively. Blue solid line shows the curvature-to-magnitude ratios of the vertical fields, $E_{2,v}/E_{0,v}$ normalised by the vertical electrode spacing l_2, as a function of the vertical to horizontal electrode spacing ratio l_1/l_2. At $l_1/l_2 = 1.73$ the curvature of a horizontal field vanishes [18]. The inset depicts the simulation of the electric field for our apparatus in the situation that the field is in plane of molecules, i.e. the horizontal field. The spacing are $2l_1 = 0.96$ cm and $2l_2 = 0.56$ cm. The signs of the electrodes, indicated as '+' or '−', denote the polarity of the electrode with respect to the common ground, hence infer the field directions. (b)-(d) show a comparison between the calculation for the spacing ratio at zero crossing in (a) ($l_1/l_2 = 1.73$) and for our apparatus ($l_1/l_2 = 1.71$), represented by solid and dashes lines respectively. (b) The magnitude of the electric field along x (red) and z (black) axes through the centre of the science cell indicated by the X in (a). (c) As in (b) but showing the electric field gradient. (d) As in (b) but showing the curvature of the electric field.

used to levitate atoms in the dipole trap against gravity, and perform Stern-Gerlach separation on atoms to characterise a spin population. Furthermore, homogeneous bias magnetic fields are used to compensate residual magnetic fields particularly from the Earth while laser cooling. We also exploit such fields to define a quantisation axis for degenerate Raman sideband cooling and an absorption imaging. In addition, larger magnetic field strengths are crucial as we are able to tune intraspecies scattering length to minimise three-body losses of Cs in a optical dipole trap and tune or search for interspecies scattering length that transfer ultracold mixtures into a particular molecular state. Considering these reasons, our experiment includes six sets of coils. Each $2D^{+}$-MOTs of Cs and Rb/ K has two pairs of coils around the cell, where the MOT and shim coils are wound onto the same rectangular Tufnol formers, yet being controlled independently. The other three sets of circular coils for the main chamber are namely "*MOT, Jump*" and "*Feshbach*" coils which are assembled in one coil frame. They are mounted around the top and bottom viewports directly onto re-entrant flanges, therefore are placed close to the atoms as possible while maintaining optical access [19]. The last set comprises of three pairs of shim coils. Two pairs of rectangular coils (shim x/ y) in the horizontal plane are attached to the posts around the main chamber mount. One pair of circular coils (shim z) in the vertical plane are secured on top of the re-entrant flanges.

2.3.1 2D-MOT coils

The 2D-MOT coils have a rectangular shape and consist of 6×6 winding for quadrupole coils and 6×1 winding for shim coils. The coils are made of 1.1 mm diameter copper wire wound onto the Tufnol coil holders which are then attached to an aluminium mounting frame as shown in Fig. 2.3(b). The coil holders are designed to have an inner dimension larger than the glass cell, thus the installation is convenient by sliding the frame over the cell and able to remove if either diagnostic or implementation is required. The quadrupole coils are operated in a anti-Helomholtz configuration where the carrying current is running in the opposite direction therefore it creates a line of zero magnetic field gradient axially along the length of the 2D-MOT

glass cell and a gradient of ~ 4.4 G cm^{-1}A^{-1} along the x- and y-axes. The shim coils are operated in a Helmholtz configuration with parallel carrying current and produce a broad spatially uniform magnetic field of ~ 0.9 G A^{-1} near the centre of the chamber.

2.3.2 Main chamber

The MOT coils are made of copper tubes with a rectangular cross section of 4.4×4.4 mm^2 while the one of jump and Feshbach coils are 3.5×3.5 mm^2. Each turn is glued together with a thermally conductive epoxy adhesive. Fig. 2.8(a) illustrates the coil geometry around the main vacuum chamber. All coils are attached to G10 coil formers which go inside the re-entrant flanges. As they are run at high currents, water flows inside the tubes parallel with the current to help dissipate heat [20]. The MOT coils produce an axial magnetic field gradient up to 0.31 G cm^{-1}A^{-1} The jump coils have a smaller diameter and number of turns compared to the Feshbach coils. As a result, they have a quicker switching time, allowing for fast sweeps without the undesirable eddy-currents associated with the mutual inductance of the larger bias coils.

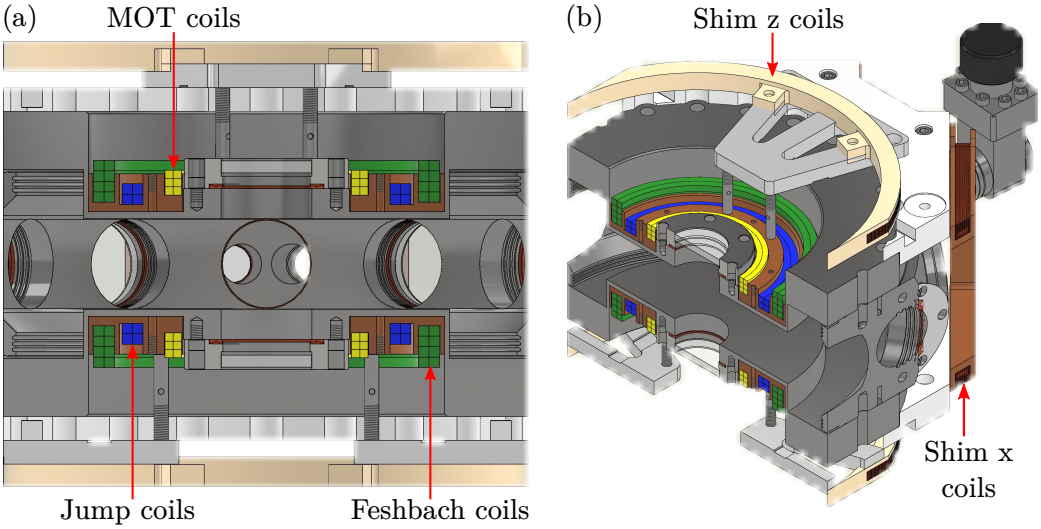

Figure 2.8: (a) A cross-section of the main chamber shows the location of the coils. The MOT (yellow) coils produces, jump (blue), and Feshbach (green) coils. (b) A side view of the main chamber shows the shim x and z coils.

Three pairs of shim coils are incorporated to produce homogeneous magnetic fields constructively in the three Cartesian directions. Two pairs of rectangular coils (shim x/y) in the horizontal plane and one pair of circular coils (shim z) in the vertical plane a magnetic field gradient of 1 G $cm^{-1}A^{-1}$ at the origin. These coils are also known as compensation coils as they produce the fields to null the stray fields that can hinder an optimisation of molasses and misalign the quatisation axis during dRSC and absorption imaging. Similar to the 2D-MOT coils, they are made of 1.1 mm diameter copper wires and wound onto Tufnol formers.

Parameters	MOT	Jump	Feshbach	Shim z
Number of turns	2 × 3	2 × 2	2 × 4	6× 6
Tubing size (mm)	3.5	4.4	4.4	1.1
Inner diameter (mm)	35.95(3)	51.88(1)	63.70(6)	115.1(1)
Outer diameter (mm)	43.14(1)	61.2(3)	72.5(1)	122.4(1)
Inner separation (mm)	55.1(3)	49.0(4)	52.2(4)	169.7(3)
Outer separation (mm)	76.6(2)	66.9(4)	87.56(4)	177.2(4)
Resistance of a pair (mΩ)	17.71(4)	12.9(3)	19.65(4)	493.65 (Theory)
Magnetic field strength (G A^{-1})	–	0.606(6)	1.040(2)	2.06(3)
Field gradient (G $cm^{-1}A^{-1}$)	0.312(5)	–	–	–
Field curvature (G $cm^{-2}A^{-1}$)	–	0.046(8)	0.056(15)	0.03(1)
Third derivative (G $cm^{-3}A^{-1}$)	0.002(6)	–	–	–
Equivalent coil radius (mm)	40(1)	56(1)	66(2)	115(3)
Equivalent coil separation (mm)	68.9(4)	60.4(4)	68.3(8)	176(3)

Parameters	Shim x	Shim y
Number of turns	8 × 10	8 × 10
Tubing size (mm)	1.1	1.1
Magnetic field strength (G A^{-1})	1.091(9)	1.12(2)
Equivalent coil length 2a (mm)	183(2)	
Equivalent coil length 2b (mm)	111(1)	
Equivalent coil separation (mm)	319.0(8)	321(1)

Table 2.3: Summary of coil characterisation

All parameters of the coils used in the experiment have been characterised

and summarised in Table 2.3. For those coils in the He*/ lmholtz configuration, the most important parameter is the peak bias field in the unit of G A^{-1} at the centre of the coil pair, i.e the centre of the main chamber. We characterise it by measuring the transverse magnetic field at the centre of the coil pair using an axial Hall probe as function of current. The slope of the linear least-square fit implies the the peak bias field. For the quadrupole coils, we need to know the magnetic field gradient as well as a small curvature at the centre of the chamber.

For simplicity, we also approximate the magnetic coil assembly as an "*equivalent coil*". Each coil of N turns carrying a current of I is substituted with a single turn of infinitesimal thickness carrying a current $I' = N \times I$ [21].

2.4 Laser systems for cooling and trapping

Laser systems provide the light to cool, trap and image each species. The near-resonant laser beams requires power and frequency stabilisation as well as frequency-tunability close to the relevant transitions. The hyperfine structure of both species is depicted in Fig. 2.9.
The wavelengths of the light are 780.2 nm, and 852.3 nm for ^{87}Rb , and Cs respectively.

2.4.1 Cs laser system

This section describes an optical setup to deliver, manipulate and monitor the frequencies and power of the light used in Cs laser cooling to prepare cold spin polarised atoms before loading into an optical dipole trap for evaporation to a Bose-Einstein condensate (BEC). All the laser beams that have been used in the experiment are illustrated in Fig. 2.10 and corresponding frequencies are summarised in Table 2.4. Two lasers provide the 852 nm light for cooling, trapping, and imaging. The first one is a Toptica TA-Pro tapered amplifier laser generating the cooling light. It addresses the atoms in the upper hyperfine-ground state of Cs ($F = 4$) and operates near the closed transition (Cs cooling). The light out of the probe output at the back port

of the laser is coupled into an optical fiber and used to stabilise its frequency on the Cs cooling transition. An error signal is derived from a Doppler-free saturated absorption spectroscopy whereby a probe beam passes through a Cs 10-mm vapour cell at room temperature. The power output on the front port is divided into various beams: $2D^+$-MOT cooling, $2D^+$-MOT push, 3D-MOT cooling, DRSC lattice, and probe beams. For the repumping transition the light is derived from the other laser: a Toptica DL Pro diode laser. Like the spectroscopy for the cooling light, the repumping laser is stabilised and locked to the $F = 3$ to $F' = 3, 4$ crossover resonance. The repumping power is split for $2D^+$-MOT, 3D-MOT, and DRSC polariser beams. Their frequencies are manipulated near the atomic resonance mostly by double-passing through an acousto-optical modulator (AOM), which is also responsible for fast power-switching. The detunings required in different stages of laser cooling are summarised in Table 2.4. The detuning of each beam is indicated with respect to the relavant transition. It is red (blue)-tuned if the detuning is negative (positive). For laser cooling, the cooling beam is red-detuned from the closed transition. The repumping light addresses the atom in the lower hyperfine groud state ($F = 3$). For DRSC, the lattice light is on resonant with the $F = 4 \rightarrow F' = 4$ transition, which is 9.2 GHz from the optical pumping transition ($F = 3 \rightarrow F' = 2$). The polariser beam is 6 MHz blue-detuned from the optical pumping transition. For an absorption imaging, the probe beam consists of both the cooling light resonant with a cyclic transition and the repumping light to pump atoms back into the cyclic transition for accurate measurements of atom number.

2.5 Diagnosis and Detection

2.5.1 Absorption imaging

Absorption imaging is the common method to yield properties of atomic clouds, e.g atom numbers and temperatures. In this section we will describe how to extract the atom number from the density distributions and temperatures from the momentum distributions. The accuracy of these parameters is highly dependant on the absorption imaging system, so the optical system

	Transition	Detuning (MHz)	AOM frequency (MHz)
Cooling spectroscopy	$F = 4 \rightarrow F' = 5$	0	-100.0
Toptica TA Pro	$F = 4 \rightarrow F' = 5$	+200.0	N/A
$2D^+$-MOT cooling	$F = 4 \rightarrow F' = 5$	-10.0	-105.0
$2D^+$-MOT push	$F = 4 \rightarrow F' = 5$	+4.0	-98.0
3D-MOT cooling	$F = 4 \rightarrow F' = 5$	-10.0	-105.0
3D-MOT cMOT	$F = 4 \rightarrow F' = 5$	-30.0	-115.0
3D-MOT molasses	$F = 4 \rightarrow F' = 5$	-50.0	-125.0
DRSC lattice	$F = 4 \rightarrow F' = 4$	0.0	-225.0
Imaging probe	$F = 4 \rightarrow F' = 5$	-4.0	-102.0
Repump spectroscopy	$F = 3 \rightarrow F' = 4$	0.0	N/A
Toptica DL Pro	$F = 3 \rightarrow F' = 4$	0.0	N/A
$2D^+$-MOT repump	$F = 3 \rightarrow F' = 4$	0.0	100.6
3D-MOT repump	$F = 3 \rightarrow F' = 4$	0.0	100.6
DRSC polariser	$F = 3 \rightarrow F' = 2$	+6.0	122.8

Table 2.4: Summary of detunings of Cs laser beams with respect to the relevant transition used to prepare cold polarised atoms before loading into optical dipole traps.

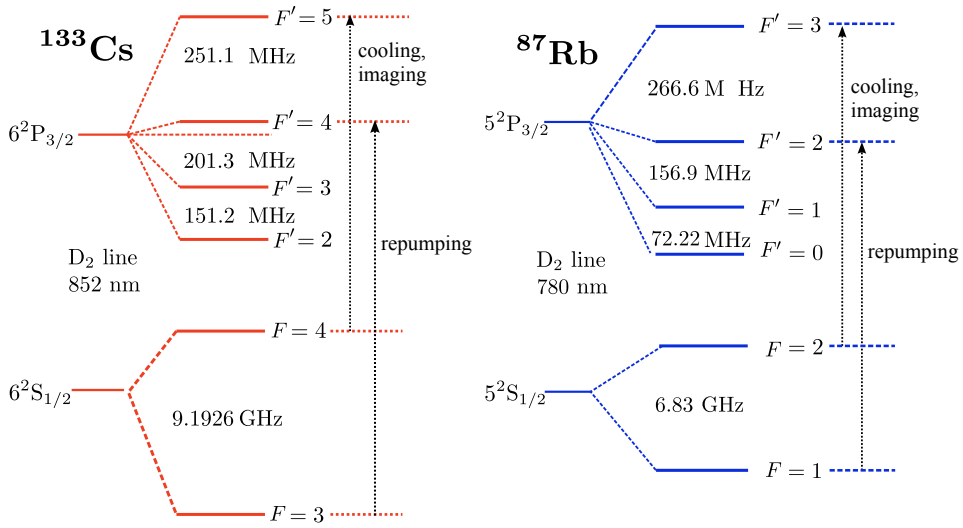

Figure 2.9: The schematic of hyperfine structures of ^{87}Rb and Cs. The arrows shows all beams used in laser cooling before evaporation in an optical dipole trap.

is crucial to be characterised and optimised, for instance, pixel size, magnification, lens position, quantisation field, and probe detuning.

Density distribution

In absorption imaging, a cold atom cloud is illuminated by a short pulse of resonant probe laser beam [16]. The atoms absorb a fraction of light and the shadow cast by the atom is then imaged onto a CCD camera (Andor iXon). In the weak probe regime, the intensity of the transmitted light decreases exponentially following the Beer-Lambert law. The intensity of the outgoing probe beam propagating along the $z-$axis through the atom column density, $n(x, y)$, and the absorption cross section, σ is described by [22]:

$$I = I_0 e^{-n(x,y)\sigma}. \tag{2.1}$$

The absorption cross section of the transition is given by:

$$\sigma = \frac{\sigma_0}{1 + 4\left(\frac{\Delta}{\Gamma}\right)^2 + \frac{I_0}{I_{sat}}} \tag{2.2}$$

where the resonant absorption cross section is $\sigma_0 = 3\lambda^2/2\pi$, Δ is the detuning of the probe beam from the atomic resonance, Γ is the decay rate of the

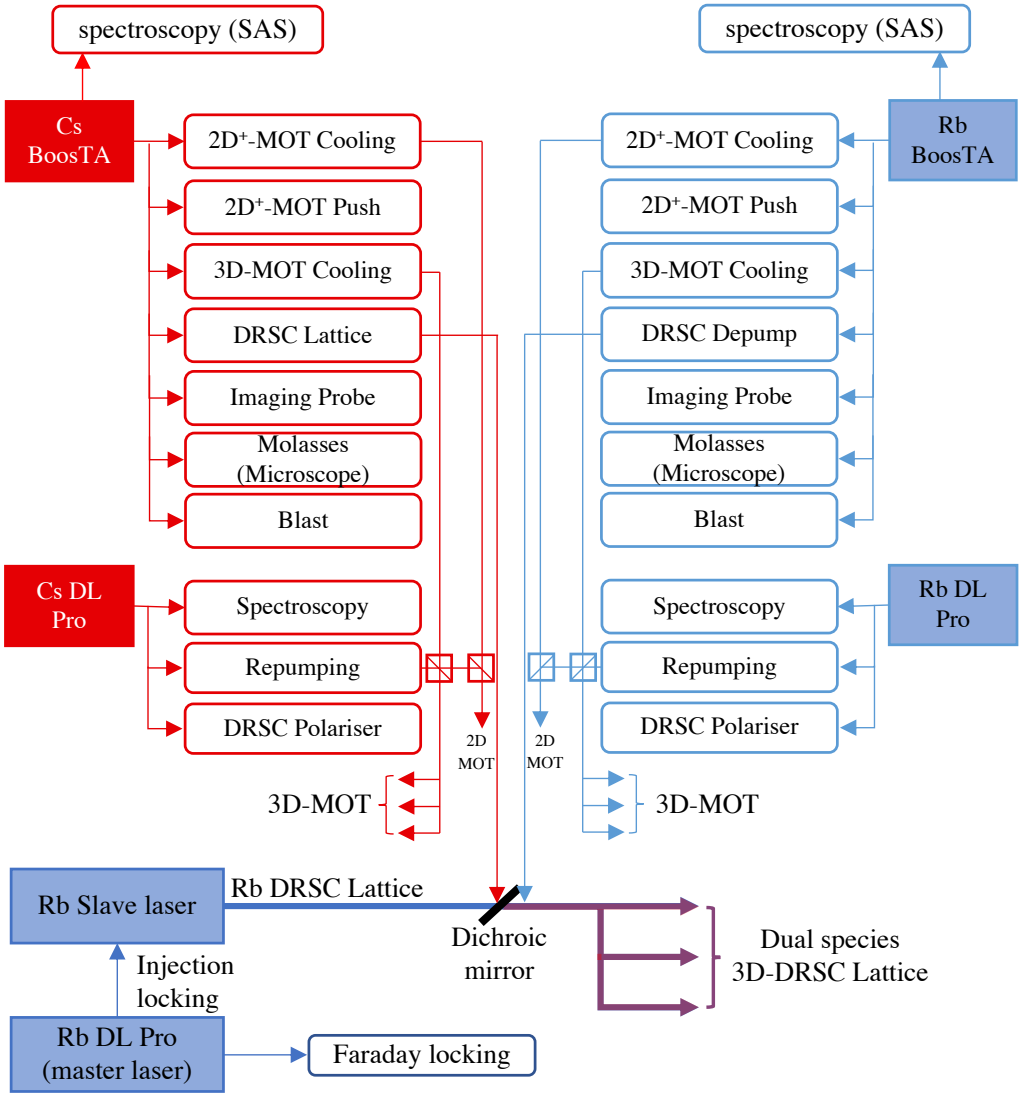

Figure 2.10: Overview of laser system for Cs and ^{87}Rb. The cooling and repumping light for the 2D$^+$-MOT and the 3D-MOT are spatially overlapped and coupled into each optical fiber. The DRSC lattice light for both species are combined on the dichroic mirror. In addition, the DRSC polariser and the imaging probe for both species are combined on the laser table (not shown).

excited state, and I_{sat} is the saturation intensity. Eq. (2.1) can also be expressed in terms of optical depth (OD), dictating the amount of absorbed light:

$$I = I_0 e^{-OD} \tag{2.3}$$

By equating Eq. (2.1) and Eq. (2.3), the optical depth is related to the atom column density as:

$$OD(x, y) = n(x, y)\sigma \tag{2.4}$$

The total atom number in the cloud is estimated by rearranging the Eq. (2.4) and integrating over the atom column density, in other words, integrating the optical depth in each camera pixel along the x and y directions.

$$N = \int_0^y \int_0^x n(x, y)\, dx\, dy = \frac{1}{\sigma_0} \int_0^y \int_0^x OD(x, y)\, dx\, dy \tag{2.5}$$

In the experiment for each shot, three consecutive images are used to measure the optical depth on each camera pixel [22, 23] as:

$$OD_{\text{meas}} = ln\left(\frac{I_{\text{light}} - I_{\text{dark}}}{I_{\text{atoms}} - I_{\text{dark}}}\right) \tag{2.6}$$

$$\begin{aligned} I_{\text{atoms}} &= \text{Probe} + \text{atoms} + \text{background} \\ I_{\text{light}} &= \text{Probe} + \text{background} \\ I_{\text{dark}} &= \text{background} \end{aligned}$$

Here I_{atoms} is the intensity of the probe beam with atoms, I_{light} is the intensity of the probe beam without atoms, and $I_{\text{background}}$ is the intensity when the camera shutter is fully open yet the probe beam is switched off. Other parameters such as the cloud centres (x_0, y_0) and cloud widths (σ_x, σ_y) of the thermal clouds can be extracted by fitting the intensity along one axis after integration of the other axis to the Gaussian distribution. For example the OD along the x-axis after y-integration is fit to a function:

$$OD = OD_{\text{peak}} \exp\left[-\frac{(\text{x} - \text{x}_0)^2}{2\sigma_{\text{x}}^2}\right]. \tag{2.7}$$

Chapter 3

Characterisation of Laser cooling

This chapter describes an experimental setup in details for a $2D^+$-MOT as an intense cold atomic source and the 3D-MOT loading around the main chamber. The setup for both ^{87}Rb is almost identical to ^{133}Cs except for a small change of a beam configuration for a retarding beam. Furthermore, subsequent sections present the characterisation of laser cooling parameters where each stage is optmised for a specific goal. First of all, for the $2D^+$-MOT we aims to maximise a flux of slow atoms being captured in the 3D-MOT with fast loading rate. Secondly, a compressed-MOT (cMOT) is optimised for an atomic density. Finally, an optical molasses is investigated to achieve the lowest temperature before further cooling and creating a polarised sample using degenerate Raman sideband cooling (DRSC) described in chapter 4. We summarise optimal experimental parameters for ^{133}Cs followed by ^{87}Rb .

3.1 Realisation of the $2D^+$-MOT

We utilised the $2D^+$-MOT method [17] to produce a high flux of slow atomic beams from background gas at high partial vapour pressure. This method allows to efficienctly load a 3D-MOT at the lower pressure region in the main UHV chamber, which is of importance for evaporative cooling to BEC. It was maintained by separating the 2D-MOT glass cell from the main chamber by a

differential pumping tube. Fig. 3.1 illustrates a beam configuration. Besides two pairs of counter propagating elliptical beams used to cool and trap atoms transversally in the conventional 2D-MOT, there are additional beams, a so-called push beam and a retarding beam, to create imbalance optical molasses in the axial direction. The imbalanced radiation pressure results from the fact that the retarding beam is a push beam that is backreflected at a 45 deg polished mirror having a 8 mm-aperture and hence this creates a shadow on the beam. The mirror is attached to the differential pumping tube. Not only the beams cause atoms having slower initial longitudinal velocity component so that they spend more time in the cooling volume and diverge less as they moves towards the end of the trap, but also turns around some atoms that initially move away from the main chamber [24, 25]. Consequently, it leads to a tighter confinement on the trap axis and enhances the atom flux. Therefore, slower atoms are separated from faster ones by the hole at the in-vacuum mirror and transferred to being captured in the 3D-MOT in the main chamber.

For compactness, two pairs of rectangular coils around the glass cell were wound so that each of which comprises of two sets of coils, whose fields are independently controlled. One set in an anti-Helmholtz configuration produces the magnetic field gradient in the transverse direction, while having the zero line of the field gradient along the axial direction towards the main chamber. The other set, the last layer of the coil in a Helmholtz configuration, generates the bias field used to shift the position of the $2D^+$ MOT to maximise the flux through the main chamber.

3.1.1 Optical setup

The optical layout of the ^{133}Cs $2D^+$-MOT source on the experiment table is illustrated in Fig.3.2. The laser system is explained in section 2.4. On the laser table, the cooling and repumping light were combined on a 50:50 beam splitter before being coupled to two separated optical fibers for a horizontal and a vertical cooling beam. The beam shape was modified to be elliptical to expand the capture volume of the 2D- MOT espectially in the axial direction. The light after the fiber was collimated by a 45-mm lens and then elongated

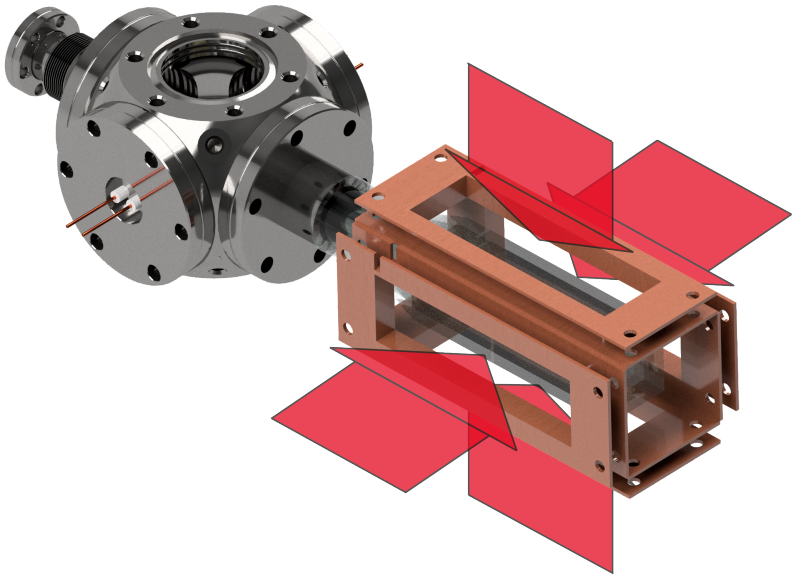

Figure 3.1: Schematic of 2D$^+$-MOT. Directions of all beams are shown: two pairs of elliptical retro-reflected cooling beams, a push beam, and retarding beam. Each of rectangular coils surrounding the glass cell contains two sets: one is responsible for generating a quadrupole magnetic field, whose zero field lies along the axial direction and the other is for magnetic shim fields to align the centre of the 2D-MOT cloud with respect to the hole of the differential pumping tube.

along the horizontal axis by a pair of cylindrical lens, which is a 13.7-mm lens followed by a 150-mm lens. As a result, the horizontal (vertical) axis of a collimated elliptical beam has a $1/e^2$ beam diameter of ~ 8.0 (78.7) mm. A $\lambda/4$ waveplate imparts circular polarisation onto each beam. Considering the horizontal cooling beam, the wide incoming beam was retro-reflected by a pyramid mirror. In this way, the beam changes helicity every reflection from the surface [26], thus two-pairs of counter-propagating beams are automatically generated having the correct polarisation to form the MOT at the zero field of the quadrupole field as in a conventional six-beam MOT. The push beam is aligned along the longitudinal axis, which is the co-axis between two chambers. A retro-reflected beam of the push beam at the in-vacuum mirror is served as a retarding beam. As the polished surface of a stainless steel mirror is polarisation-dependent, the power of the retarding beam is changed accordingly when optimising the polarisation of the push beam. The power

of the push beam was controlled by the amount of light before its fiber on the laser table.

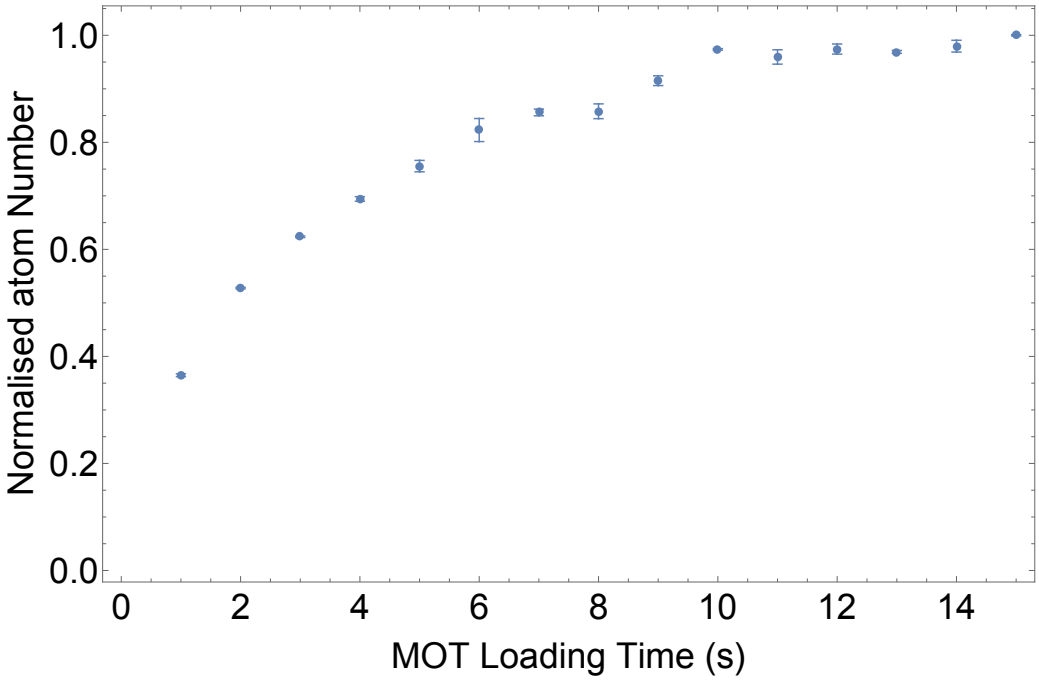

Figure 3.2: Optical layout of the 2D$^+$-MOT. A vertical cooling beam is prepared on a lower breadboard and sent to the glass cell via a periscope mirror. A horizontal cooling beam is placed on the upper breadboard. Its height is set so that the beam passes through the centre of the glass cell.

3.1.2 Optimisation

The total flux of 2D-MOT depends on various parameters and characterised by the trapped atoms in the 3D-MOT. For example, the dimension of the cooling volume affects the capture velocities, the cooling rate, and therefore the total flux [24]. Next, the vapour pressure was investigated where it is set to balance out an increase in the loading rate and the loss rate due to collisions with background gas. The dependence of 3D-MOT loading on laser power and detunings of the 2D-MOT cooling are studied as they directly relate to the spontaneous scattering force on atoms. The presence of the push and retarding beams is shown to enhance the loading rate and their power ratio seems to have an impact on the total flux. For all measurements

only one parameter was varied while all the other settings were put on their optimum values.

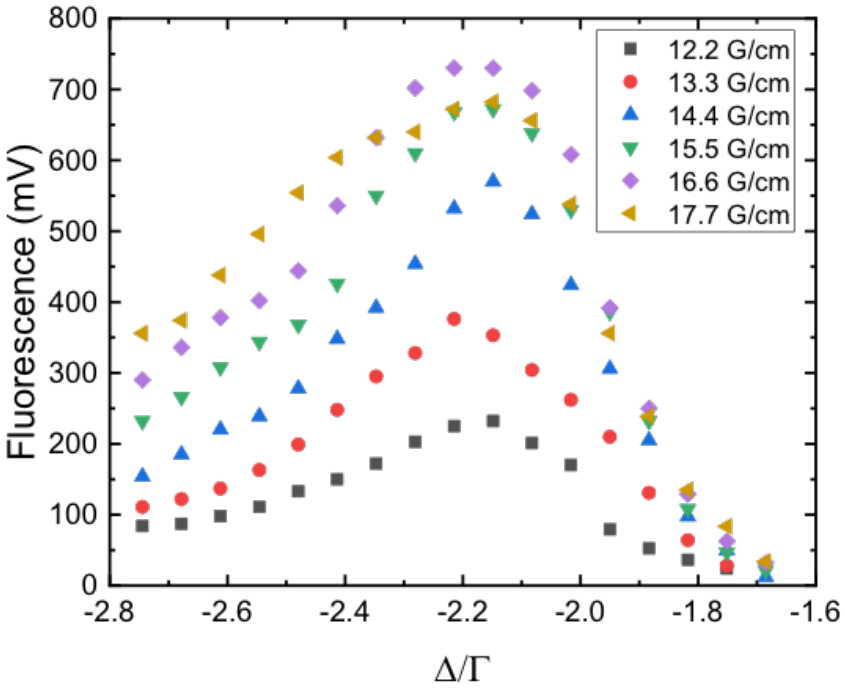

Figure 3.3: Dependence of the atom number of the 3D-MOT on the 2D-MOT cooling detuning for various axial magnetic field gradients of the 2D-MOT coils. There is small difference in the optimal detuning between the field gradient in the range of 12 - 18 $\mathrm{G\,cm^{-1}}$. However, the atom number is maximised at the field gradient of 16.6 $\mathrm{G\,cm^{-1}}$.

3.2 3D-MOT

3.2.1 Optimisation

The 3D-MOT loading was investigated as a function of the intensity. The dispenser current is initially driven at 1.2 A and the MOT field gradient of 12.6 $\mathrm{G\,cm^{-1}}$ is used. The cooling light is set to -2.32(4)Γ from the cooling transition. The impact of the detuning of the repump laser is shown in Fig. **??** (b) optimal at -1Γ . We can trap on the order of 1×10^{8} atoms. Eventually,

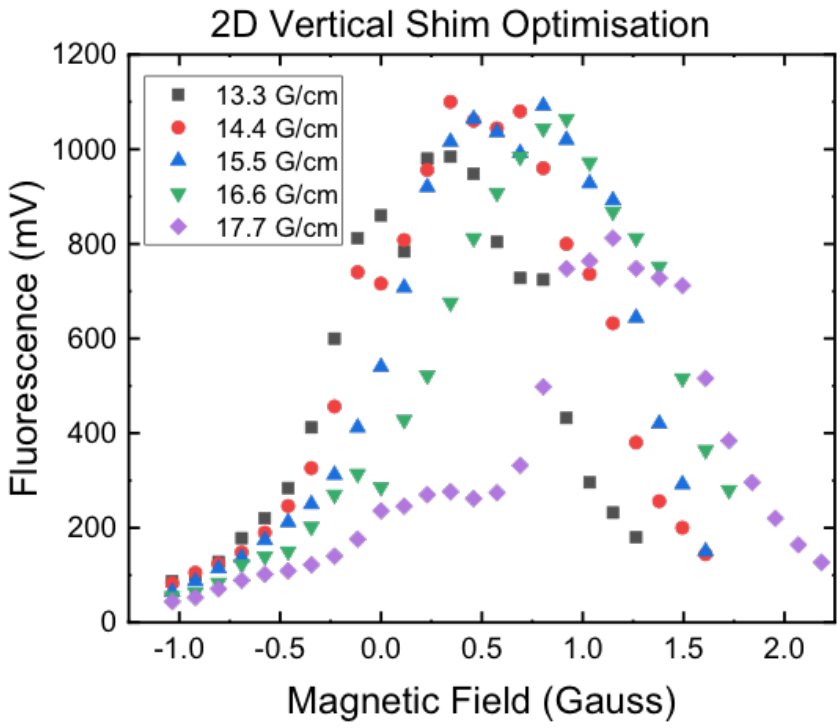

Figure 3.4: Dependence of the atom number of the 3D-MOT on the shim field. The centre of the 2D-MOT cloud was aligned with respect to the hole of the angled differential pumping surface. The data was derived at a magnetic field gradient of 12.6 G cm^{-1}.

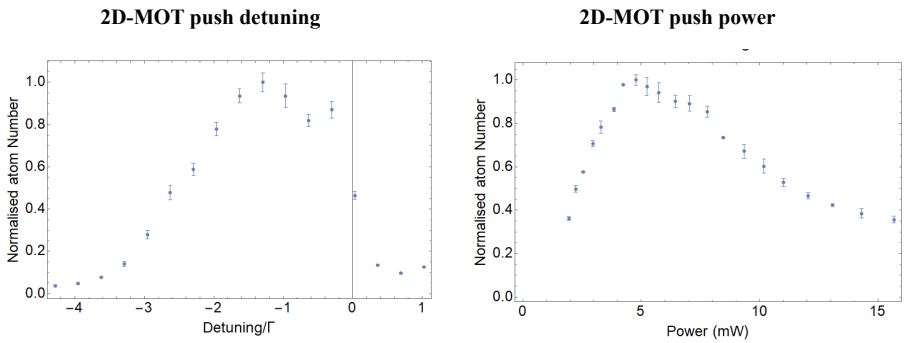

Figure 3.5: The normalised 3D-MOT atom number as a function of a push beam's (a) detuning and (b) power. The optimal power is 5 mW with the iris in place. The 2 mW comes out to the retarding beam with this input push power.

Stages	δ_C/Γ	δ_R/Γ	δ_{push}/Γ	P_{push}(mW)	γ (G/cm)
$2D^+$-MOT	-2.65		-1.46	4.7	20
3D-MOT	-1.22	-1	-	-	12.6
cMOT	-2.45	1.12	-	-	25

Table 3.1: Summary of optimal experimental parameters to operate ^{133}Cs laser cooling. $\delta_{C(push)}$ is the detuning of the cooling (push) light from the cooling transition $F = 4 \rightarrow F' = 5$. $\delta_{R)}$ is the detuning of the repumping light from the repumping transition $F = 3 \rightarrow F' = 4$. $I_{C(R)}$ is the total intensity of the cooling (repumping) beam. I_{push} is the push beam's intensity. γ is the magnetic field gradient.

we set the cooling light to maximum peak intensities of mW cm^{-2} for each beam.

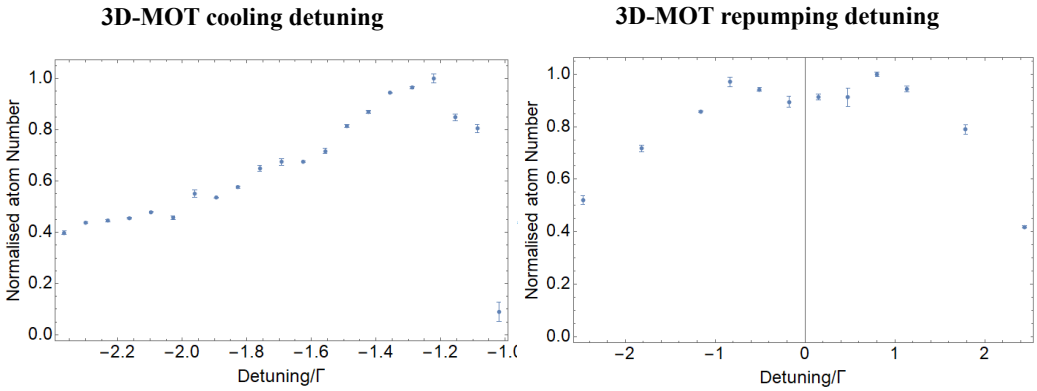

Figure 3.6: Dependence of the atom number of the 3D-MOT on the detuning of (a) cooling and (b) repumping light.

The next parameter to consider is the magnetic field gradient associated with the trapping size and hence the MOT size. All parameters remain the same values (P_{cool}= 9.0(6) mW, P_{repump} = 0.6(2) mW, Δ_{cool} = $-2\pi\times7.8(8)$ MHz), except the magnetic field. The experiment was performed by varying the current to the quadrupole coils from 5 to 25 A, corresponding to the approximate magnetic field gradients from 5 G cm^{-1} up to 20 G cm^{-1}. In fig 3.6 it is apparent that as the magnetic field gradient increases, the number of captured atoms also rises until it reaches the optimum value and then falls down. From the fact that the Zeeman energy shift is proportional

to the magnetic field gradient, as the position relative to the centre of the trap increases, the energy shift changes significantly. Therefore, the energetic atoms located further away from the trap centre hardly scatter with photons because it becomes far-off resonance to the cooling laser, and thus a smaller number of atoms are captured at higher magnetic field gradients. In addition, it can be observed that the MOT strongly depends on the detuning of the cooling beam as shown in fig 3.6. It also demonstrates the dependence between the field gradient and the cooling detuning. Finally, we can conclude that at the optimum magnetic field gradient of around 16 $\mathrm{G\,cm^{-1}}$ the red-detuning of $2\pi\times7.8(8)$ MHz from resonance for ^{133}Cs can trap the highest atom number up to 1×10^8 can be achieved.

3.3 Compressed-MOT

3.3.1 Optimisation

To increase the MOT density, one needs to increase the confinement as well as decreaseing the photon scattering rate, i.e , reducing the radiative force due to the scattered photons .

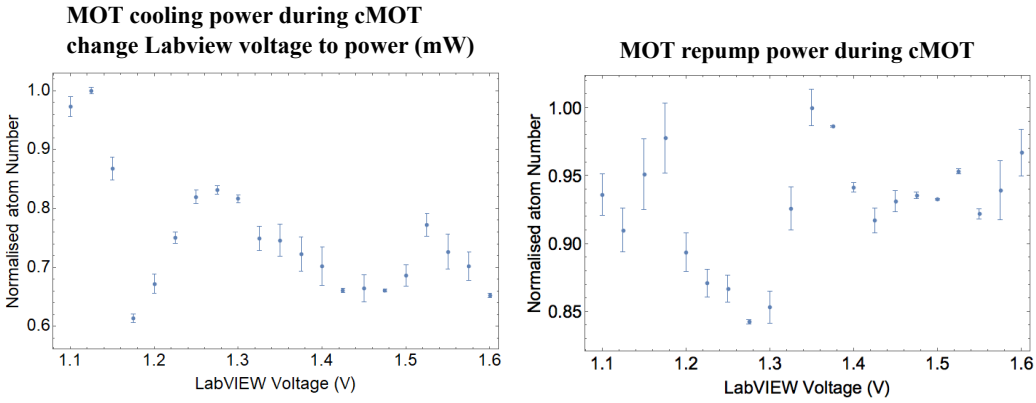

Figure 3.7: Dependence of the atom number of the 3D-MOT on the (a) cooling and (b) repumping beam during cMOT.

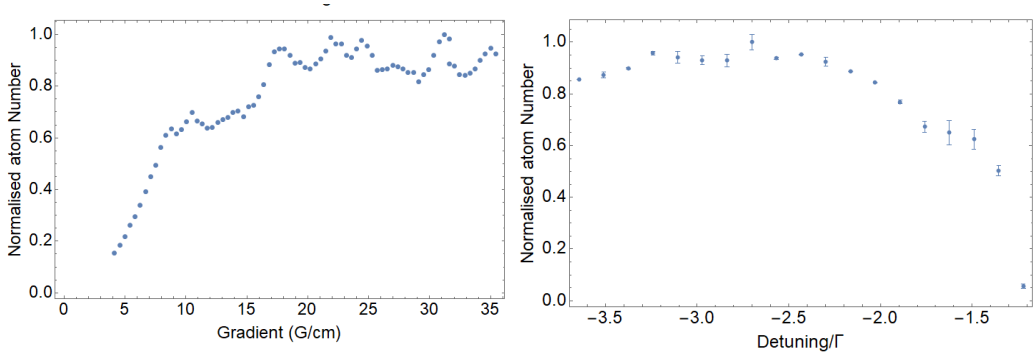

Figure 3.8: Dependence of the atom number of the 3D-MOT on (a) magnetic field gradient (b) cooling detuning.

Chapter 4

Degenerate Raman Sideband Cooling

Working towards Bose-Einstein condensation, the atoms are further cooled after molasses to achieve low temperature and high phase space density prior to evaporative cooling. However, laser cooled atoms in an magneto-optical trap followed by optical molasses has two limitations.

The first limitation of laser cooling is reabsorption, whereby a photon scattered [27] by one atom due to spontaneous emission is abosorbed by another atom before the atom escapes the atomic cloud. It creates a repulsive radiation force between the atoms. Therefore, the re-scattering events produce outward forces the compete with the inward trapping forces, this limits any further increase in density. Furthermore, this suppresses cooling owing to random emission direction of re-scattered photons.

The second limitation is light-assisted collisions between an atomic pair where one of the atom is electronically excited induced by near resonant light fields. They interact via induced dipole-dipole interaction at long range, so-called "resonant-dipole" interaction [28]. As the interatomic distance get closer, specifically at the Condon point [16], a laser frequency is resonant with one of the potential energy curves in which one of the atoms is excited. In the optical molasses stage, there is the probability where the red-detuned light field induces inelastic collisions between the atom pair. The atoms will experience an attractive molecular potential as they approach each other and

then gain kinetic energy after the excited atom spontaneously decays back to the ground state. This kinetic energy can cause both atoms escaping from the trap, i.e. trap loss.

On one hand, the red-detuned laser can couple atoms to an attractive potential of bound molecular states. On the other hand, the atoms can experience a repulsive potential in the presence of the blue-detuned laser. In either cases, the kinetic energy released to both colliding atoms after following the potential curves leads to trap loss.

One cooling technique that is able to circumvent these limiting factors by reducing the number of scattering events is degenerate Raman Sideband cooling (DRSC). With this method atoms are cooled into the target state, which is a dark-state, in other words, being decoupled from the light. In brief, it utilises optical lattices to stimulate Raman transitions in conjunction with optical pumping into the lowest vibrational ground state of the trap.
In this chapter, we present detailed experiments with DRSC for ^{133}Cs and ^{87}Rb . We have spin polarised 4.3(3) $\times$ 10^7 ^{133}Cs atoms at a temperature of 1.2(1)μK.

4.1 Cooling mechanism of Degenerate Raman sideband cooling

There are three main ingredients of the DRSC scheme: optical lattices, a static magnetic field, and optical pumping light. First of all, a cold atom in the presence of deep optical lattices is trapped in harmonic potentials ($\frac{3}{2}k_BT_{\text{atom}} \ll k_BT_{\text{trap}}$), depicted in parabolic curve as shown in Fig.4.1. The ladders reprensent vibrational states in each magnetic sublevel (m_F). Not only the potential creates tight confinement of the atoms, but also induces the coupling between the ground-state Zeeman sublevels. The two-photon stimulated Raman transitions are driven between these vibrational states by exploiting a small constant magnetic field. With an optimal magnitude of the magnetic field the Zeeman energy shift is tuned such that the energy of vibrational states of neibouring magnetic sublevels are degenerate; $|m_F, \nu\rangle \rightarrow |m_{F-1}, \nu-1\rangle \rightarrow |m_{F-2}, \nu-2\rangle$, where ν is the vibrational state quantum

number. Additionally, the atoms is illuminated with polariser light such that population in the ground state $|F, m_{F-2}, \nu - 2\rangle$ is optically pumped to the excited state $|F' = F-1, m'_F = m_F - 1\rangle$ strongly via a σ^+-transition followed by spontaneously decays back into the target m_F state. This is also known as the spontaneous Raman transition. Many cycles of cooling are accomplished until the final step where the atom with $|m_F, \nu = 1\rangle$ transferred to the $|m_F - 1, \nu = 0\rangle$ state. Here, it becomes decoupled from the polariser light, which prevents the atoms from being further cooled. This is mitigated by having a weak π component of polarisation on the polariser to keep optically pumping though a π-transition to the lowest vibrational ground state. Experimentally, it can be achieved by slightly tilting the angle of light propagation with respect to the direction of the magnetic field.

Importantly, the cooling works effectively in the Lamb-Dicke regime, whereby the recoil energy of the scattered polariser photon is smaller than the spacing of the vibrational level: $\sqrt{E_{Rec}/\hbar\omega} < 1$, where $E_{Rec} = \frac{\hbar^2 k^2}{2m}$. As a consequence, the process is less likely subject to heating due to the scattered photon since the vibrational quantum number is preserved during the decay from the excited state into the ground state and two quanta of vibrational energy are drawn out of the atom for every cycle.

Light shift in the presence of optical lattice, polariser and external magnetic field

We will briefly discuss how enery levels of an atom shifts under the influence of light and external magnetic fields as illustrated in Fig.4.1. First of all, the evoluation of the system is governed by the the associated Hamiltaonian is given by [28] :

$$\hat{H} = -\frac{\hbar^2}{2m}\nabla^2 + \left[U(\mathbf{x})\hat{\mathbf{I}} + g_F D_{FS}\mathbf{B}_{\text{eff}}(\mathbf{x}) \cdot \hat{\mathbf{F}}\right] + g_F \mu_B \mathbf{B}_{\text{ext}} \cdot \hat{\mathbf{F}}, \tag{4.1}$$

$$\text{where}\, U(\mathbf{x}) = U_0 |\epsilon(\mathbf{x})|^2 \qquad U_0 = \frac{\hbar\Gamma^2}{12\Delta_{\text{avg}}}\left(\frac{I}{I_S}\right) \tag{4.2}$$

$$\mathbf{B}_{\text{eff}}(\mathbf{x}) = U_0 \frac{i}{2\hbar}\{\epsilon^*(\mathbf{x}) \times \epsilon(\mathbf{x})\} \tag{4.3}$$

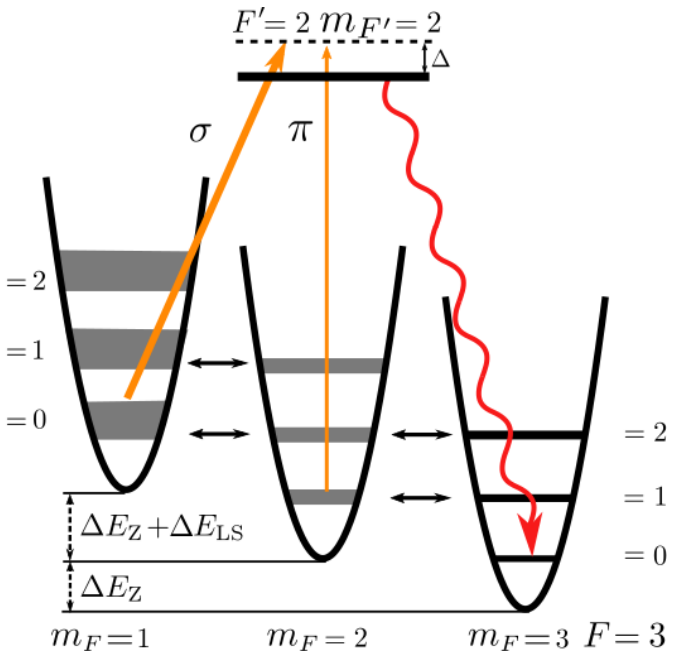

Figure 4.1: The schematic shows a cyclic cooling of Degenerate Raman sideband cooling for ^{133}Cs . A static magnetic field is applied to make the vibrational states of each magnetic sublevels ($|m_F, \nu\rangle$) in degeneracy, i.e. $|3,\nu\rangle, |2,\nu-1\rangle$, and $|1,\nu-2\rangle$ states. A two-photon stimulated Raman transition is represented by double-headed arrows. An additional polariser beam (orange arrow) drives a spotaneous Raman transition (red wavy arrow) which pumps the atom back into $|3,\nu-1\rangle$. The polarisation of the light is circularly-polarised propagating along the vertical axis at a small angle α to the quatisation axis, defined by the mangtic field direction. The optical pumping predominantly drives σ^+-transition and weakly π-transition for the atom in the $|2,0\rangle$ state into the lowest vibrational ground state $|3,0\rangle$. As a result, the polariser causes power-broadens on only the vibrational levels of the $m_F = 1$ state. Image adpated from [28]

$$\Delta_{\text{avg}} = \left(\frac{1}{2\Delta_{1/2}} + \frac{1}{2\Delta_{3/2}}\right)^{-1} \qquad D_{FS} = \left(\frac{\Delta_{3/2} - \Delta_{1/2}}{\frac{\Delta_{3/2}}{2} + \Delta_{1/2}}\right) \tag{4.4}$$

From eq.4.1 the total energy of the atom consists of kinetic energy and potential energy due to the external fields. Two terms in square brackets describe light shift due to the optical lattice. The first one is the scalar component, which depends on the light intensity and its detuning as shown in

eq.4.2 and scaled as I/Δ_{avg}. The second one is the tensor component, which arises from the coupling between the field polarisation and the electron's spin orientation (m_F). It is also known as a fictitious magnetic field as it behaves like the first order Zeeman shift. As clearly seen in eq.4.3, its magnitude and direction is associated with the local polarisation vector of the light field and proportional to $\{\epsilon^*(\mathbf{x}) \times \epsilon(\mathbf{x})\}$. Importantly, in this particular case where the lattice light also simulate the Raman transition in addtion to light shift contribution and so confining the atom, the effective field must be nonzero. This could be achieved by having nonzero light helicity. In other words, the interference of lattice light need to form either elliptically or circularly polarised light at the bottom of the lattice's trap. Lastly, the Zeeman shift is included due to an application of a uniform magnetic field B_{ext}, whose direction defines the quantisation axis.

To further investigate how the Raman coupling originates, we rearrange eq. 4.1 and utilise perturbation theory according to [28] as follows:

$$\hat{H}_0 = -\frac{\hbar^2}{2m}\nabla^2 + U(\mathbf{x})\hat{\mathbf{I}} + g_F\left[m_F\mu_B B_{ext} + D_{FS}\mathbf{B}^{\parallel}_{\text{eff}}(\mathbf{x})\cdot\hat{\mathbf{F}}\right] \tag{4.5}$$

$$\hat{H}_C = g_F D_{FS}\mathbf{B}^{\perp}_{\text{eff}}(\mathbf{x})\cdot\hat{\mathbf{F}}, \text{where} \tag{4.6}$$

Here, $\mathbf{B}_{\text{eff}}$ is decomposed into the paralle ($\mathbf{B}^{\parallel}_{\text{eff}}$) and perpendicular ($\mathbf{B}^{\perp}_{\text{eff}}$) components. Essentially, the longitudinal effective field leads to relative energy shift as well as slight spatial variation among different Zeeman sublevels shown in eq. 4.5. The $\mathbf{B}^{\perp}_{\text{eff}}$ induces the Raman transition among adjacent magnetic sublevels. In the DRSC scheme, the small amount of external magnetic field is applied to shift these levels being degenerate.

4.2 Experiment in 3D lattice for Cs

In this section we describe how we implement DRSC of ^{133}Cs for our experiments to reach a lower temperature at higher density and spin-polarised into a single lowest state $|F = 3, m_F = 3\rangle$.

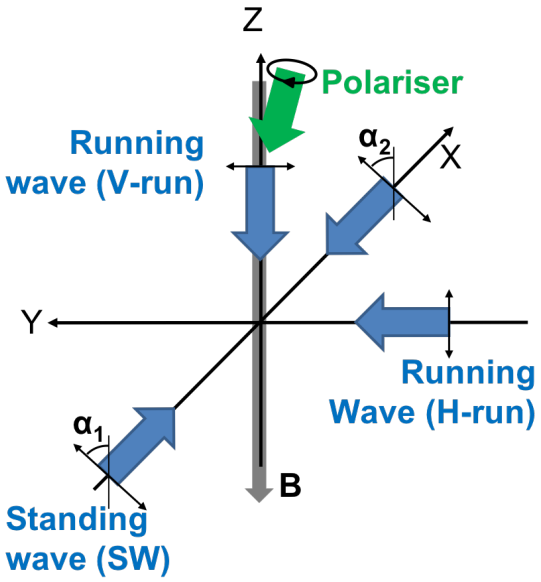

Figure 4.2: An experimental setup of DRSC. An alignment of three-dimensional lattices in four-beam configuration [29], consisting of one pair of standing wave on the x-axis and a running wave on the y-axis, and another running wave along the z-axis. All lattice light has linear polarisation, but the plane of its polarisation has been optimized experimentally to achieve a maximum trap depth along the quantisation axis, defined by the magnetic field's direction.

4.2.1 Laser system

The lattice light is required to produce non-dissipative trap therefore is tuned off from optical resonance frequency. It is linearly polarised and red-detuned by 9.2 GHz from the $F = 3$ state. The frequency is chosen to be resonant with the $F = 4 \rightarrow F' = 4$ transition as it is additionally responsible for repumping the atoms in the $F = 4$ state back into the cooling cycle in the $F = 3$ manifold. The choice of their beam size is estimated from a lattice simulation to optimise trap frequencies together with trap depths limited by the power budget of 170 mW. The lattice beams are coupled to three separated fibers having a $1/e^2$ diameter of approximately 3.2 mm on the optical table for the experiment. The power ratio between beams are controlled by a $\lambda/2$ waveplate before the PBS used to split the light before the fibers. Note that all optimisation in section 4.2.2 has been performed

at the power of 34, 49, and 86 mW for the standing, the horizontal running, and the vertical running wave respectively.

Another essential ingredient is a polariser. The polariser frequency is detuned from the $F = 3 \rightarrow F' = 2$ transition controlled by a double-passed AOM. Unlike the lattice beams, its $1/e^2$ beam diameter is 4 mm so that the whole atomic cloud experiences the same amount of light intensity. As the polarisation stability is of importance for optical pumping, its polarisation has been purified by the PBS right after the fiber and is then transformed to be circularly polarised by a $\lambda/4$ waveplate. The beam propagation points down with a small angle relative to the axis of the magnetic field vertically in order to fast drive the σ^+- transition but also a weak π-component for a final cooling step.

4.2.2 Optimisation procedures and results

For optimal cooling rate to prepare a cold and dense atomic cloud prior to loading into the conservative trap, there are various parameters to be optimised. To begin with, we would like to observe the evidence of atoms being trapped by optical lattices and investigate how the polariser involves in DRSC. The following section describes the step-by-step procedures.

Lattice and polariser alignment

Following various previous experiments implementing DRSC [16, 29], the three-dimensional lattice is configured with four beams as displayed in Fig.4.2. On the horizontal plane parallel to the optical table there is one pair of standing wave (counterpropagating) beams, one travelling beams, propagating perpendicular relative to the standing wave and having vertical polarisation, and the other travelling beam pointing down vertically and being polarised in the same direction as the beam propagation of the horizontal travelling beam.

To optimise the number of trapped atoms, the intersection of all beams need to be achieved to address the same volume of an atomic cloud as well as their relative polarisation angles. We start off by coarse alignment without

the need for the polariser beam and the retro-reflected beam blocked. Each beam is aligned individually by looking at the distortion of the steady-state 3D-MOT on the CCD camera by modulating the beam power by switching a SRS shutter with 1 MHz. Each beam is aligned further by using 5 μs pulses of the lattice light. At the end of molasses, the atoms are prepared in the $F = 4$ manifold. When the lattice beams are well-aligned to the atoms the atoms are transferred to the $F = 3$ state.The atoms are then dark to the probe beam when doing an absorption imaging in the absence of repump light. Hence, we observe an apparent reduction in atom number. Once they were aligned, introduce a retro-reflected beam, by optimising the light coupled down the fiber, and repeat the same diagnosis. At this point, we can see with all beams present, in the absence of the polariser, that the atoms feel some trapping from the lattice beams when imaging with repump light on (see Fig.4.3(c)). The polariser beam can be aligned in a similar way as described above. Once some trapping is seen in the lattice, a long lattice hold time can be used to get the polarising beam parameters approximately correct so that we can see some cooling in the lattice. The fine-tuning of the position of each running wave beam is optimised in the presence of the standing wave beam and the polariser (one running wave beam is blocked while the other is optimised).

For instance, it is clearly seen in Fig.4.4(a,b) that the beam displacement is sensitive on the order of a millimeter when adjusting the beam pointing via the last mirror's knob. After that, overlapping of all beams should enhance the maximum number of trapped atoms. Lastly, Fig.4.4(c) indicates how another tunability, the polarisation angle of the standing wave, has an impact on the trapping potential. Moreover, we have investigated an improvement of trapped atoms by adding a $\lambda/4$ in the retro-reflected beam path [16].

Optimisation

The cooling efficiency of the DRSC process is determined by number of trapped atoms in the target state and a lowest temperature. The atom number can be optimised by performing levitated absorption imaging. This method takes advantage of a Stern-Gerlach imaging [30]. This technique al-

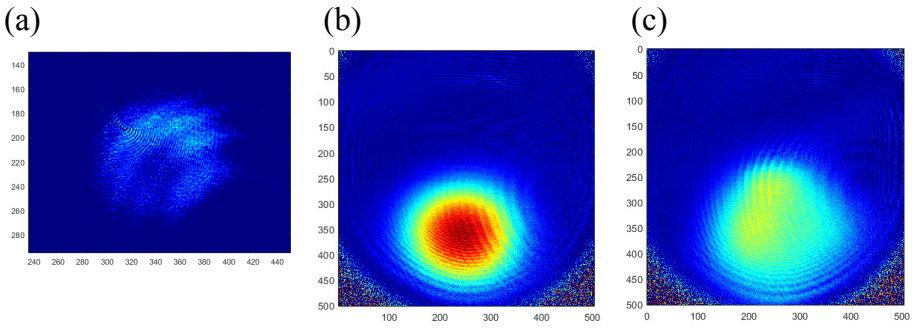

Figure 4.3: Images of ^{133}Cs cloud taken from absorption imaging. (a) Individual lattice alignment when the light hits the centre of the MOT. The reduction of the atom is observed when imaging without repump light. (b) In the absence of 3D DRSC lattice the cloud after molasses is falling down from the centre of the field of view due to free fall at a given TOF. (c) Observation of some trapped atoms in the 3D DRSC lattices after molasses. Note that no polariser has yet involved.

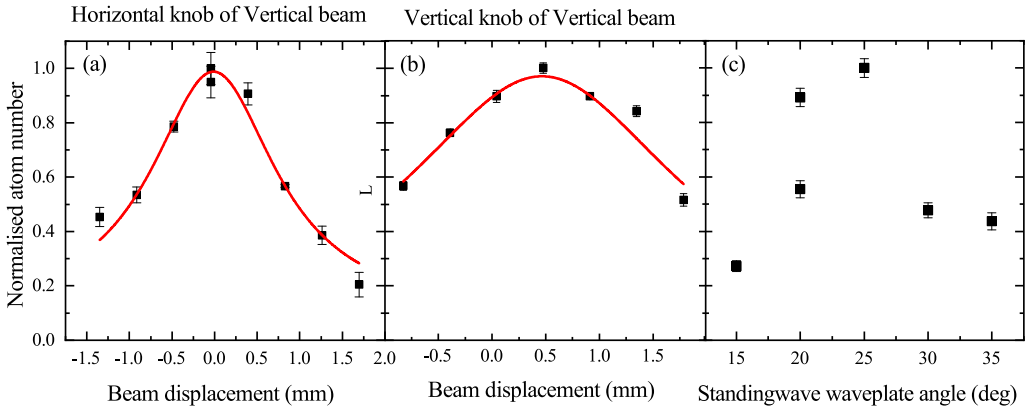

Figure 4.4: The dependence of trapped atoms on the lattice alignment and the polarisation of the incoming standing wave.

lows to resolve the distribution of the state population among magnetic sublevels. The atoms in different m_F states are exerted the spin-dependent force, thus, separate spatially due to their different magnetic moments. Atoms with the spin-stretch state are pushed up to the topmost before an image is taken, which is the state of the trapped atoms. In practice, a vertical magnetic field gradient of 37.1 G/cm was applied at the end of the DRSC stage to levitate the atomic cloud against the gravity and prevent from free falling during the time-of-flight absorption imaging. Nonetheless, the magnetic field gradient

introduces some anti-trapping potential along the horizontal axis. This effect can be reduced by applying an additional magnetic bias field in the vertical direction (67.2 G).

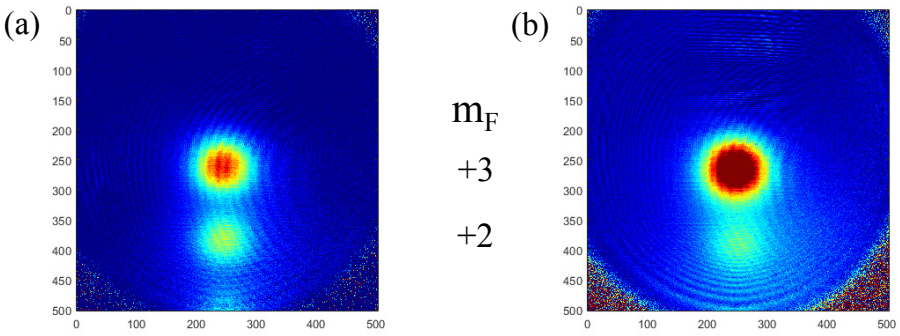

Figure 4.5: The Stern-Gerlach is used to optimise the polariser parameters during the lattice off ramp at the end of DRSC sequence. It allows to resolve population distribution among magnetic sublevels on the ground state. The applied magnetic field gradient causes the atomic cloud in each m_F states seperating from one another after a given TOF due to their different magnetic moments. The timing to switch off the polariser during the lattice off ramp is of importance. By turning off the polariser at the end of the lattice loading (b), most of the atoms are siginificantly transferred to the target state $|F = 3, m_F = 3\rangle$ and reach higher density than turning off the light during the lattice off ramp in (a).

As the polariser plays an important role in cooling and spin-polarised atoms into the $|F = 3, m_F = 3\rangle$ state, its optimal associated parameters: polarisation, frequency, and intensity are characterised for maximum atom number as shown in Fig.4.6(a). To initial search for the cooling effect, apply a few hundreds of mG of the bias magnetic field along the vertical direction to define the quantisation axis. Also, the polariser's frequency was set to moderate blue-detuned. The maximum atom number works at 8 - 9 MHz (Fig.4.6). To understand this, the polariser broadens the energy of the $m_F = 1$ state as it strongly drive the σ^+ transition in addition to the Zeeman effect. Blue-detuned light contributes to an upward light shift such that the $|m_F = 1, \nu = n - 2\rangle$ is degenerate with $|m_F = 2, \nu = n - 1\rangle$. Otherwise, the stimulated Raman coupling happens with $|m_F = 1, \nu = n-1\rangle$ when applying red-detuned polariser (providing a downward shift), resulting in some heating

effect instead of cooling. Similarly, the intensity and polarisation involving the cooling are optimised as shown in (Fig.4.6).

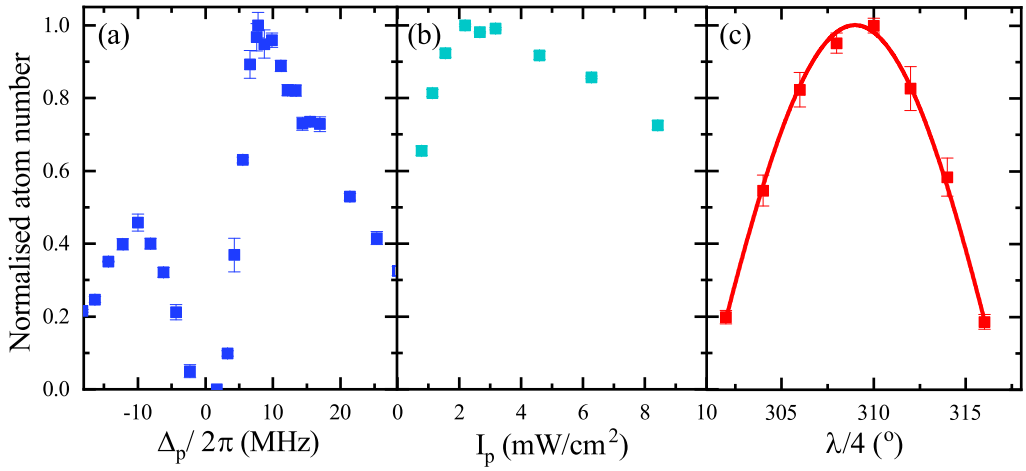

Figure 4.6: Optimisation of polariser parameters: detuning, intensity and polarisation. (a) the detuning of $+1.16\Gamma$ from the $F = 3 \rightarrow F' = 2$ transition. (b) The maximum trapped atoms occurs at the intensity of 2.6 mW/cm. The ratio of polarisation components driving between σ^+ and π-transitions are optimised by a $\lambda/4$ waveplate.

Next, the bias magnetic field is characterised to match the vibrational levels between adjacent m_F states and so increase the Raman coupling. Experimentally, we found that by ramping the field from a higher magnitude the cooling works more efficiently. For the temperature, it is opimised by the duration of the lattice light. Fig.4.7) shows that the temperature after DRSC equilibrates at $\sim 1\mu K$. In conclusion, at 4 ms lattice pulse we can achieve the maximimum atom of $4.3(3) \times 10^7$ atoms at 1.2(1) μK.

4.3 Experiment in 3D lattice for ^{87}Rb

Our machine is working towards making ^{87}Rb ^{133}Cs molecules. For fast loading it is beneficial to be able to cool both species simultaneously before loading into the optical trap. We have followed the pioneer experiment on the dual-species DRSC [31, 32]. The key concept is to figure out a method that both species fulfil the condition for two-photon stimulated Raman transitions at one magnetic field strength. The condition for degeneracy: $\delta m_F g_F \mu_B =$

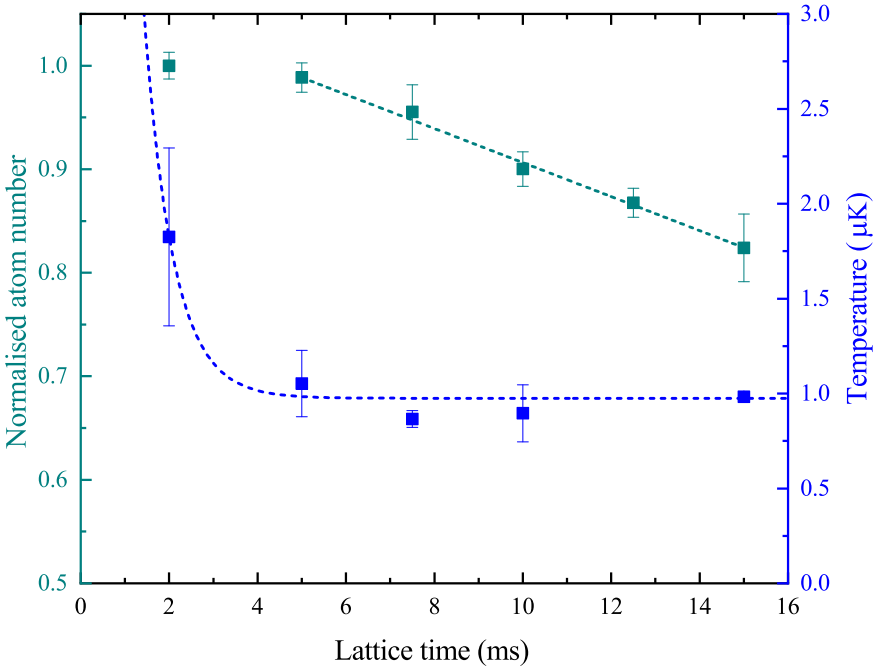

Figure 4.7: The optimisation of lattice duration is achieved to compromise between the number of trapped atoms (green) and the lowest temperature (blue). The blue dashed curve is an exponential dacay curve fitted to the data. In our experiment we apply the DRSC for 4 ms, producing $4.3(3) \times 10^7$ atoms at 1.2(1) μK.

$\hbar\omega_{\text{vib}}$. For the same B, $\frac{\omega_{\text{Rb}}}{\omega_{\text{Cs}}} = \frac{g_{F(Rb)}}{g_{F(Cs)}} = 2$. Here, the Zeeman shift for ^{133}Cs is a factor of two larger than one for ^{87}Rb owing to their different Landé g-factors: $-\frac{1}{4}\left(-\frac{1}{2}\right)$ for ^{133}Cs (^{87}Rb). However, as discussed in 4.1 the energy shift also originates from the light shift due to the lattice light, whose scalar component is proportional to its intensity, also referring as a lattice depth. Therefore, in practice they circumvented the mismatch between two species' Zeeman shifts by individually determining the optimal magnetic field for ^{133}Cs . Then, tuning the power of the ^{87}Rb lattice light, thus its lattice depth, at this field magnitude so that the vibrational states of adjacent magnetic sublevels are degenerate as shown in Fig. 4.8. Moreover, they found that the ^{87}Rb DRSC works efficiently at the lattice detuning of -18 GHz from the polariser transition $F = 1 \rightarrow F' = 0$. The reason being is that off-resonant

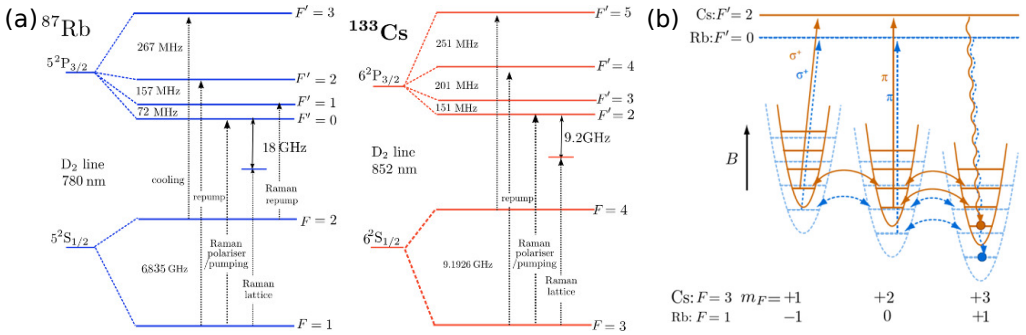

Figure 4.8: (a) A summary of energy levels and relevant frequencies for dual-species DRSC. For ^{87}Rb , the Raman lattice light is $\sim$ -18 GHz red-detuned from the polariser transition ($F = 1 \rightarrow F' = 0$ transition). The polariser is blue-detuned from the optical pumping transition. In addition, the Raman repumping light is resonant to the $F = 2 \rightarrow F' = 2$ transition. For ^{133}Cs , the Raman lattice light is $\sim$ -9.2 GHz red-detuned from the optical pumping transition ($F = 3 \rightarrow F' = 2$ transition). This beam is also responsible for repumping atoms in the $F = 4$ manifold as it is resonant to $F = 4 \rightarrow F' = 4$ transition. (b) A schematic of vibrational levels of two-color DRSC. The solid(dashed) arrows represents σ^+, π transitions of polariser (single-sided) and the degeneracy of stimulated Raman transitions (double-sided) for ^{133}Cs (^{87}Rb) case. At the optimised homogeneous magnetic field, the cooling works for both species. This is done by adjusting the lattice depth of ^{87}Rb whereby its vibrational spacing is about a factor of two larger than the one of ^{133}Cs .

excitations leading to heating are more suppressed than Raman transitions, for larger detunings [28]. As opposed to ^{133}Cs , the hyperfine splitting of ^{87}Rb is smaller than the ^{133}Cs one, which is $E_{\mathrm{HFS}}/h = 6.835$ GHz [33]. Hence, rather than simply shifting the frequency of the cooling transition controlled by an AOM as in the ^{133}Cs case, we have investigated two techinques to stabilise the frequency offset from resonance on the order of 10 - 20 GHz and offer a wide range of tunability. The method of digital beat locking [34, 35] was firstly explored in section 4.3.2(A). In the end, a simpler locking method using the Faraday effect [21] in section 4.3.2(B) has implemented in the setup as larger detuning can be achieved.

4.3.1 Two-color lattice laser system

A laser system was constructed to combine the lattice light of both species on one single mode polarisation maintaining (PM) fiber (Oz-optics) and so three fibers in total before sending them to the main experiment. We employed an injection locking technique to deliver adequate power for lattice light, aiming at least similar intensity as demonstrated in [31]. It essentially comprises of two main components: a single-frequency high power slave laser and a narrow-linewidth master laser stabilised at a desired frequency. By injecting the free-running slave laser with a few mW provided by the master laser, it enforces the slave laser to operate on the seed laser frequency.

Slave laser

A home-built slave laser provides the light for ^{87}Rb DRSC lattice. It consists of a Fabry-Perot laser diode (LD785-SE400) mounted in a temperature stabilised alumnium block at 13°. Its frequency is locked by seeding the laser diode with an optimal power of $\sim$ 3.2 mW from the stabilised master laser, which is produced by a Toptica DL Pro external cavity diode laser (ECDL) with wavelength 780.2 nm. When injection is achieved, the total optical output power of $\sim$ 360 mW is delivered at 490.64(1) mA. Fig.4.9 summarises a simplified optical layout of two-color lattice light. An elliptical beam was corrected by an anamorphic prism pair (APP). Serving as an isolator to avoid back-reflection, a half waveplate ($\lambda/2$), a rotating PBS cube, a Faraday rotator and a fixed PBS cube were used. To optimise the Faraday rotator, without the $\lambda/2$ rotate the rotating PBS until the reflected power after the fixed PBS cube is minimised. Then, insert the $\lambda/2$ and adjust its angle to maximise the transmission after the fixed PBS cube. After that, following the setup demonstrated in [14], the stability of the slave laser has improved. The small amount of reflected power from the fixed PBS cube was coupled to the fiber, referred as the leaked slave light. The injection light from the master laser was also coupled to the other end of the same fiber. In this way, by optimising the fiber coupling efficiency of the leaked slave light, the beam and alignment of the injection light is automatically optimised. The seeded power to the slave can be controlled by the half waveplate right after the

master laser.

Additionally, for intensity control of the ^{87}Rb lattice light the beam was sent to a single-pass AOM (Gooch & Housego 3110-120) operated at a fixed frequency (110 MHz). Then, it was combined with the ^{133}Cs lattice light on a dichroic mirror (part number). Finally, they were split into three paths. Specifically for ^{87}Rb , the power budget at the main experiment for a standing wave, a horizontal running wave, and a vertical running wave are $\sim$ 42, 47, and 65 mW respectively. More importantly, a 40 μW depumping beam resonant to the $F = 2 \rightarrow F' = 1$ transition was overlapped with two lattice beams.

4.3.2 Laser frequency stabilisation for master laser

(A) Digital beat locking using an optical phase-lock loop (OPLL)

Beat locking using an optical phase-lock loop [34, 35] is based on all-digital phase-sensitive detector and any beat frequency ranging from sub-MHz up to tens of GHz. This large capture range offers a capability of locking the laser frequency off-resonant from the optical transition. The key principle of this method is as follows. It applies an electronics-based negative feedback control system to track a small relative phase between two lasers and then adjust the phase associated with their frequency difference, namely beat frequency (f_{beat}), to match one of a reference oscillator (f_{ref}). To achieve this we implement an evaluation board (Analogue Devices ADF411XSD1Z) along with a USB-interfaced controller board (Analogue Devices SDP-S), having a phase-frequency discriminator chip (Analogue Devices ADF4107), which enable locking frequency up to 7 GHz. In principle, if the frequency of the master laser is referenced to the another stabilised Rb laser locked on the ^{87}Rb $F = 2 \rightarrow F' = X_{2,3}$ transition, the maximum lattice detuning can be achieved up to -13.7 GHz. However, the detuning could increase if we upgrade an additional circuit as suggested in [34]. In our slave-master laser configurement, frequency stabilisation for the master laser is translated into one for the slave laser.

Fig.4.10 illustrates a simplied concept of how the OPLL is integrated

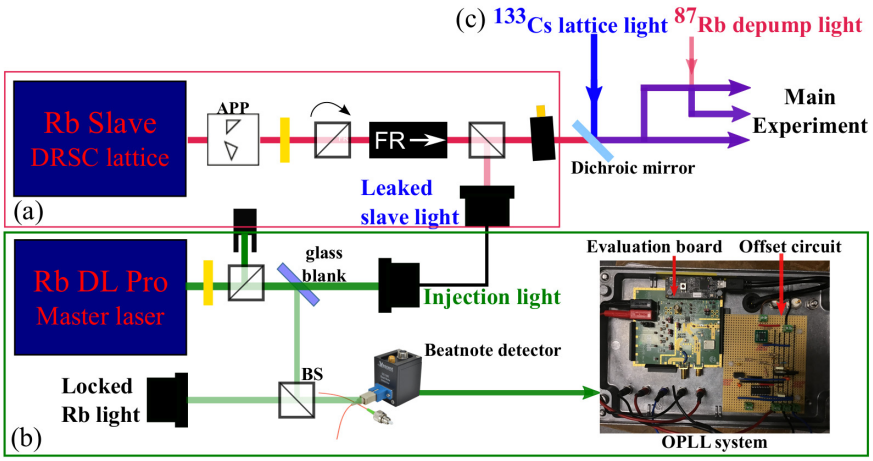

Figure 4.9: Schematic of optics used for the two-color DRSC lattice light. It consists of three main components: (a) ^{87}Rb slave-master laser system for injection locking, (b) frequency stabilisation for the master laser and (c) ^{133}Cs lattice light. (a) The injection light and leaked slave light are overlapped in one fiber from opposite ends. By optimising the fiber coupling efficiency of the leaked slave light, we ensure that the injection light are mode-matched to the laser diode in terms of beam size and alignment, leading to stable performance [14]. (b) The first locking technique (4.3.2), beat locking using an OPLL, is shown here. A beat note between two lasers, $\sim$ 100 μW each beam overlapped at a beam splitter, is sent to a the multi-mode fiber-coupled photodetector to compare it with the reference frequency on the evaluation board 4.10. (c) The fiber-coupled ^{133}Cs lattice light is overlapped on a 45°-angle dichroic mirror before splitting in to three separate PM fibers. Unlike ^{133}Cs, there is an additional depumping beam of ^{87}Rb being overlapped with lattice light into two fibers, that depumps residual atoms out of the $F = 2$ manifold back into the cooling cycle ($F = 1$). Small amount of depumping light transmitted through a first PBS is used to beat with the slave light to monitor the slave's frequency stability.

in our laser system and an error signal is derived. The beat note signal is generated by overlapping the same amount light from each laser on a fiber-coupled beat note detector (Vescent Photonics D2-160, BW = 9.3 GHz). It is of essential that they have the same polarisation and an optimal total power on the detector is ($\sim$ 200 μW). Then, the beat freqeuncy divided by

a factor N is compared to the on-board 10 MHz reference frequency divide by a factor R at the phase detector (ADF4107) mounted on the evaluation board. The evaluation board will output a signal of either 0 V when no frequency difference $\left(\frac{f_{\text{beat}}}{N} = \frac{f_{\text{ref}}}{R}\right)$ or 5 V $\left(\frac{f_{\text{beat}}}{N} \neq \frac{f_{\text{ref}}}{R}\right)$. As the locking point is normally applied at zero-crossing, it is necessary that the error signal is symmetric about 0 V. This is tackled by sending the signal to a homebuit offset circuitary, which applies a gain-two amplifier to the signal before adding a -5 V bias leading to a square-like signal as an example in Fig.4.12.

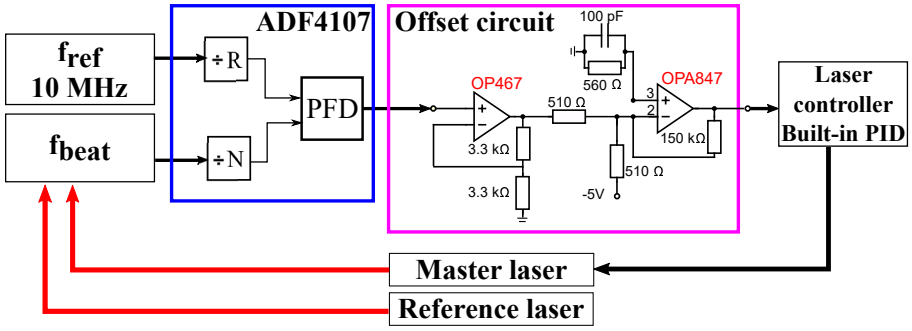

Figure 4.10: A simplied layout of feedback loop used in beat locking scheme. The scaled beat frequency between the slave and master laser (f_{beat}/N)is compared with the one of a reference oscillator (f_{ref}/R) at a phase-frequency detector (ADF4107). The output signal (0 or + 5 V) associated with the phase and frequency difference between the two divided frequencies is then amplified and adding an offset voltage of -5 V. As a result, the signal between -5 V and +5 V can be used as an error signal, where 0 V is a corresponding locking point. This is fed back to a built-in PID control in the master laser controller.

The performance of the beat locking was deduced from the stability of the slave frequency. This is achieved by conducting a beat measurement with the third reference laser, provided by the Toptica BoosTA laser. The linewidth of the injection locked slave laser determines the short-term stability. One possible characterisation is quatifying from width of the interference envelop ($f = 1/t$), which was acquired from an oscilloscope in average mode. The width can be thought as how well these two lasers are still in phase-coherence with each other. Figure 4.12(a) indicates that the slave laser has $\sim$ 500 kHz linewidth as a result of stable beat locking. Moreover, we analysed the long-

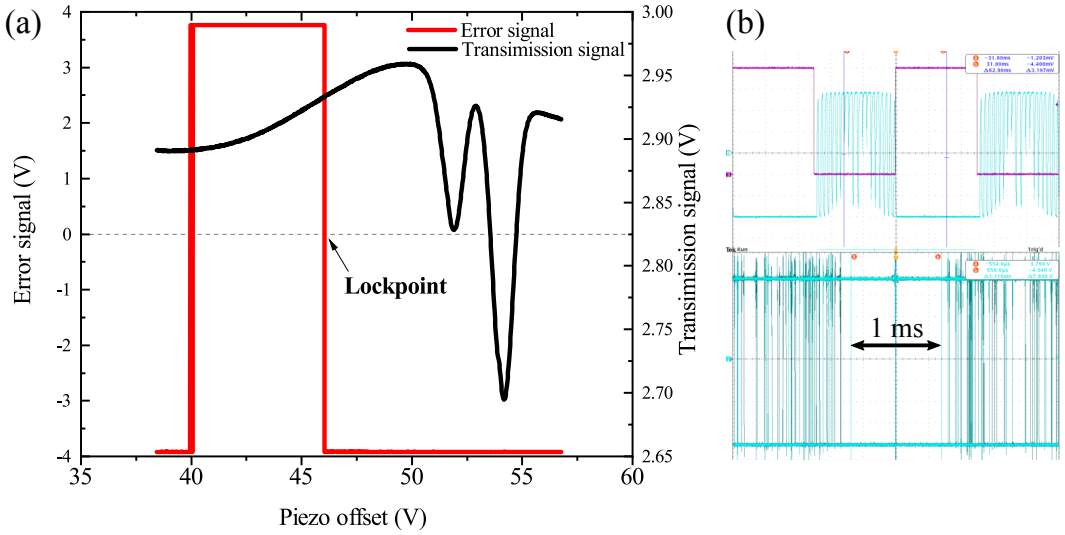

Figure 4.11: (a) An error signal derived from the digital-beat locking technique is shown in red. The locking point is engaged at the zero-crossing. Here, the lasers beat at 2.5 GHz, corresponding to a lattice detuning of ~ 9.2 GHz. The reference laser is locked to the (b) Top: Noise on the error signal (blue) occured when $f_{\text{beat}} \sim 4$ GHz introduces the frequency instability. Bottom: PID response when the locking is engaged. As clearly seen, within 1 ms in the middle where the PID fails to respond the frequency change.

term stability by an Allan deviation at $f_{\text{beat}} = 2.5$ GHz as shown in Fig.4.12. (b). The proof-of-principle of this method seems to compatible with the lattice light application. Nevertheless, we have further increased the beat frequency to 4 GHz compared at the evaluation board, corresponding to -11.7 GHz lattice detuning, and found fringes on the error signal (Fig.4.12(b)) leading to inaccurate locking points. Consequently, the laser frequency potentially drifted and became unstable. This was limited by the fact that we use the built-in PID feedback circuit, which is disable to respond faster than 1 ms (Fig.4.12(c)).

(B) Off-resonance frequency locking using the Faraday effect

To avoid the frequency jump due to the noisy error signal derived from the electronic phase-lock loop system in a previous section 4.3.2, we implemented another simpler technique for off-resonance laser frequency stabilisation

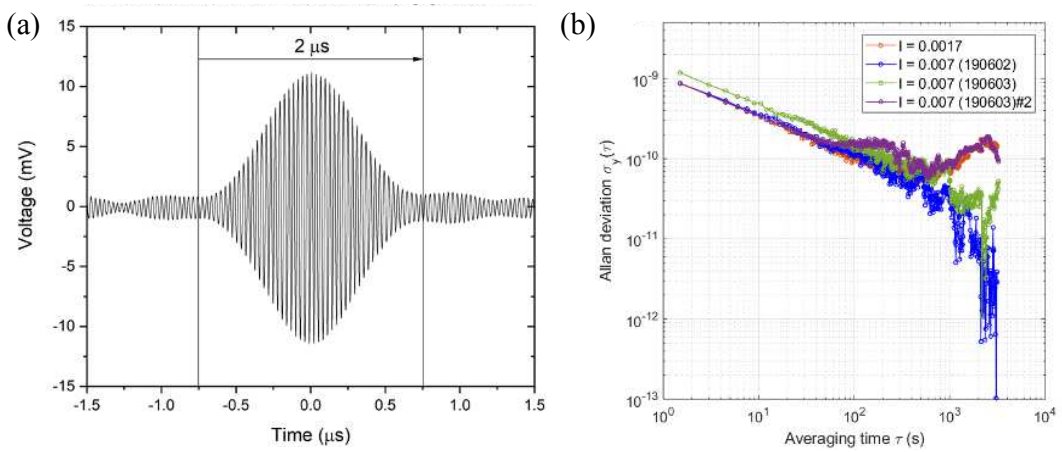

Figure 4.12: The frequency stability of the slave laser is determined by the performance of OPLL. (a) Short-term stability is inferred from its linewidth: an example of a beat note signal of 33.21 MHz between the injection locked slave laser and the reference Rb laser (Toptica BoosTA) locked on the the ^{87}Rb $F = 2 \rightarrow F' = X_{2,3}$ transition. The beat envelop, measured on an oscilloscope in average mode, shows the phase coherence betwen two lasers and implies the linewidth of $\sim$ 500 kHz. (b) An overlapped-Allan deviation analysis shows the fractional frequency stability was $\simeq 10^{-11}$ over an hour.

demonstrated by Marchant *et al* exploiting the Faraday effect [21]. In a nut shell, the rotation of light polarisation results from the magnetically induced birefringence on an atomic medium [36, 37]. In this particular geometry a direction of magnetic field, defining a qantisation axis, is oriented along the axis of light propagation. Only the $\sigma^{\pm}$ transitions are driven. The degeneracy of the Zeeman sublevels are lifted as an effect of the magnetic field. Therefore, the resonant frequencies associated with the left and right circular polarised light that stimulate the $\sigma^{\pm}$ transitions in the atomic medium are displaced in opposite direction. Furthermore, the refractive indices of the atomic medium associated with two circular components of polarised light are also shifted accordingly, i.e atoms becomes birefringent. Essentially, the left and right circularly polarised light travel at different speeds, and thus pick up a relative phase as it propagates [37]. In the experiment, atomic vapour is illuminated by light with linear polarisation, that one can be considered as a combination of an equal amount of two circular components of polarisation. For frequency away from the resonances, where the absorption

leading to a dichroism effect is negligible, the relative phase shift leads to a rotation of a polarisation' plane during passage through the atomic vapour.

Experimental method

Basically, we replaced the digital beat locking system in section 4.3.2 with the apparatus shown in Fig.4.13 to obtain the Faraday error signal. In brief, the light from a commercial ECDL at 780 (Toptica TA Pro, master laser) reflected from the glass blank was used. The light is sent through a $\lambda/2$ and a PBS cube to ensure well-defined linear horizontal polarisation. To avoid photodiode saturation, it is then attenuated to $\sim$ 50 μW with a neutral-density filter (ND) before passing through a 75-mm heated rubidium vapour cell. Heating and a uniform magnetic field were generated by a long solenoid, essentially the same cell used in [21]. The transmitted light after the Faraday cell is analysed by a polarimeter, composed of another $\lambda/2$, PBS cube, and a pair of photodiodes, which outputs the differencing signal. The $\lambda/2$ is set about 45° with respect to the input polarisation such that balanced signals incident on each photodiode in the absence of any optical rotation, i.e no applied magnetic field by turning off the current supplied to the solenoid. The Faraday error signal is fed back to a built-in PID control system of a Toptica controller (master laser). Potential locking points are observed at various zero crossings in the Faraday signal, corresponding to a π phase shift between the left and right circular components of the incident light.

The frequency tunability has been characterised by adjusting the cell temperature (current sent to the solenoid) relating to atomic density. Each zero-crossing potentially corresponds to a possible detuning. Following their method allows us to potentially lock the frequency below the $F = 1 \rightarrow F' = 0$ transition up to 19 GHz (see Fig.4.14). An overlapped-Allan deviation analysis shows the fractional frequency stability was 1.5 $\times 10^{-10}$ for a 8 s averaging time as shown in Fig.4.15. Over an hour of the measurement the frequency deviation is $\sim$ 11 MHz. This is adequate for a 4-ms DRSC lattice pulse application.

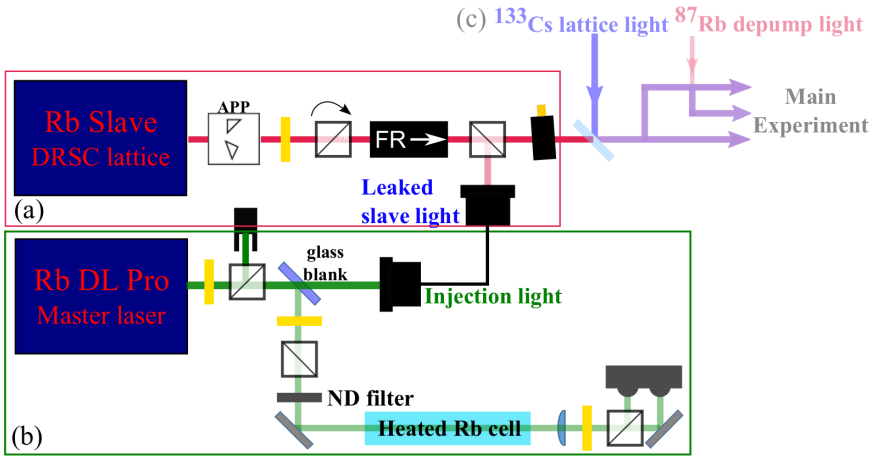

Figure 4.13: The beat locking setup is replaced with the Faraday setup. A home-built solenoid is used to heat up a 75-mm Rb cell together with providing a homogeneous magnetic field along the cell axis. The locking frequencies can be adjusted by changing the applied constant current, hence the magnitude of the magnetic field.

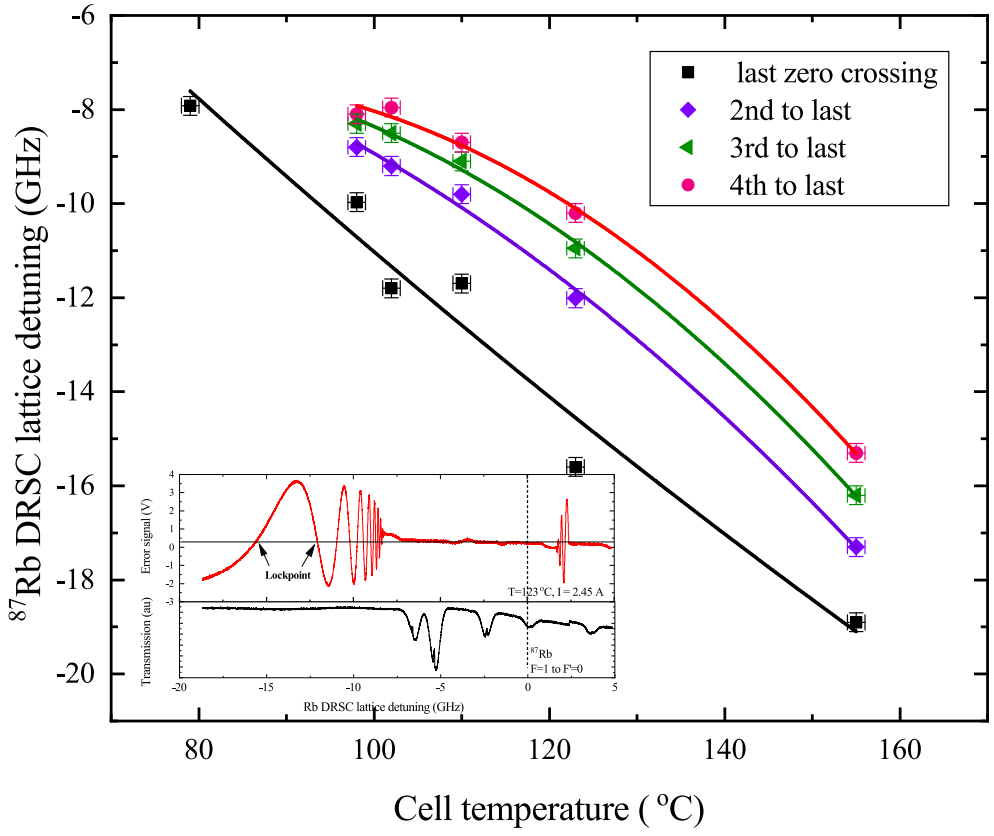

Figure 4.14: Temperature dependence of the Faraday signals at current of 2.45 A) allows the wide range of detuning tunability, from -8.0(2) to -18.9(2) GHz from the polariser's transition ^{87}Rb $F = 1 \rightarrow F' = 0$. The last, second to last, third to last, and fourth to last zero crossings are illustrated as potential locking points.Inset: An example of a normalised Faraday signal as a function of detuning from ^{87}Rb $F = 1 \rightarrow F' = 0$ transition. Specifically, the rubidium cell was heated to 123°. A Doppler-free transmission spectrum is shown as a frequency reference.

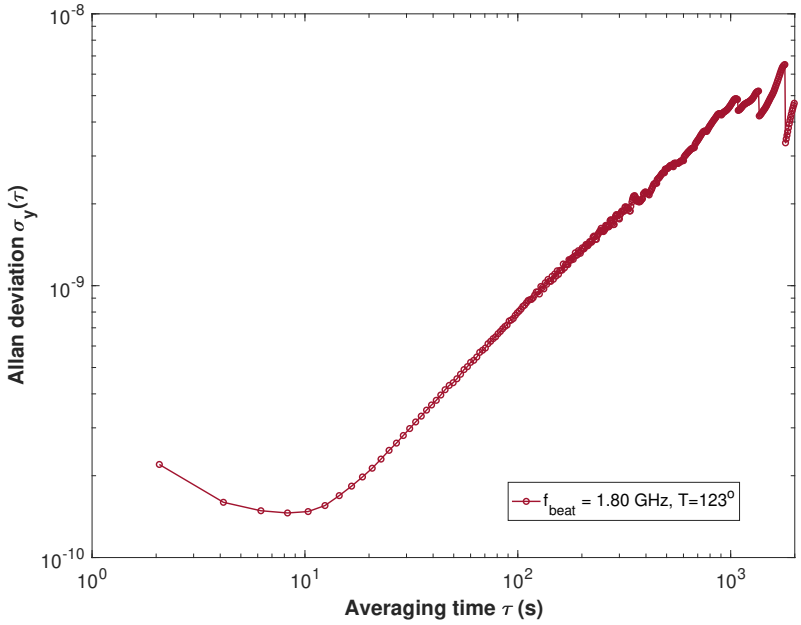

Figure 4.15: Long-term frequency stability using the Faraday effect. The overlapped Allan deviation of the beat frequency between the master laser locked by Faraday effect and the repumping laser locked by Doppler-free pump-probe spectroscopy. A curve corresponds to a single measurement using a spectrum analyser with the sampling time of 2.0(1) second. Its resolution bandwidth (RBW) was set to 30 kHz, video bandwidth (VBW) to 30 kHz, and the detector type to average: 10. It shows the fractional frequency stability was 1.5 $\times 10^{-10}$ for a 8 s averaging time.

Chapter 5

Bose-Einstein condensate of Cs in an optical dipole trap

5.1 Evaporative cooling in an optical dipole trap

After the DRSC phase, spin-polarised Cs atoms in the $|F = 3, m_F = +3\rangle$ state have an adequate phase-space density for evaporative cooling in an optical dipole trap. As they are in a high-field seeking state, they cannot be trapped in a magnetic trap. Following the method to produce the first BECs of Cs [12], atoms are loaded into two dipole traps sequentially. To begin with, atoms are loaded in a large volume reservoir trap for good mode-matching with a few millimeters Raman-cooled atomic cloud and therefore a large amount of atoms are captured. Then, atoms are transferred into the tighter dimple trap. By this way, off-axis atoms are less likely hotter as they gain a small amount of kinetic energy, converted from the potential energy of the wide reservoir trap [16].

5.1.1 Reservoir trap

The reservoir trap is generated by a broadband Ytterbium fiber laser with a wavelength around 1070 nm. It composes of two horizontal beams crossed at an angle of 90 degrees in a bow-tie configuration, which allows the recycling

of the power in both beams as well as the use of larger beam waists [16]. The beam waist at the atomic cloud is ~ 500 μm, resulting in too weak confinement in the vertical direction to hold the atoms against gravity. Therefore, to counterbalance the gravitational potential, a vertical magnetic field gradient is applied to produce an additional potential to levitate the atoms. However, according to Gauss's law for magnetism $\nabla \cdot B = 0$, it implies that there are axial components of magnetic field gradients along x and y planes in addition to the vertical direction. As a result, this creates some anti-trapping potential along the beams. The application of a large magnetic bias field in the vertical direction mitigates the effect of the anti-trapping in the axial direction. Furthermore, this offset magnetic field causes a shift of the zero magnetic field's location further from the atoms and an increased collision rate between Cs atoms due to having a large intraspecies scattering length.

Following the experimental method from [16], to transfer the Raman-cooled atoms into the levitated reservoir trap, we ramp up the reservoir trapping light during the lattice off ramp in 1 ms. Then, suddenly after the DRSC lattice are completely switched off we apply a vertical bias field produced by the vertical shim coils to maintain the atomic state and shift the zero-field position below the atomic cloud before the application of a magnetic levitation gradient. Then, we ramp the bias coil to the final value of 60 G with the corresponding scattering length of $a_{\mathrm{scatt}} \sim 1170a_0$ and turn on the quadrupole coil to levitate the atoms. Using this timing sequence, we can align the position of the first reservoir beam to the atoms by maximizing the atom number after 100 ms hold time under the condition of slight under-levitation for the second ramp. In this way, those atoms trapped in the reservoir trap are clearly separated from others with free-fall. Similarly, the position of the second beam is optimised for atom number at long time-of-flight.

During fine beam adjustment, we have observed an oscillation of atom number and atomic cloud position at different amplitudes for various magnetic field gradients. It results from the finite rise time of the quadrupole coil in practice. To minimise the center-of-mass oscillation, the magnetic field gradient is required to initially over-levitate the atoms to compensate the velocity acquired from their immediate free-fall and then back down to

the levitation gradient for atoms in the $|F = 3, m_F = +3\rangle$. After an observation, the magnetic field gradient is ramped up and then ramped down to the final levitation gradient of 31 G/cm in ms.

Other parameters such as beam power and hold time has been explored to optimise both temperature and atom number loading into the dimple trap. We ramp down the power from 30 W to 20 W and gradient from 31 G/cm to 23 G/cm to evaporate the Cs atoms from the reservoir into the dimple over a 1500 ms. With the routine summerised in Fig.5.1, we achieve the loading of $\times 10^7$ atoms at 3.1 μK into the reservoir trap. After 2 s of plain evaporation , atoms are thermalised with the reservoir trap reaching to the temperature of 1.5 μK.

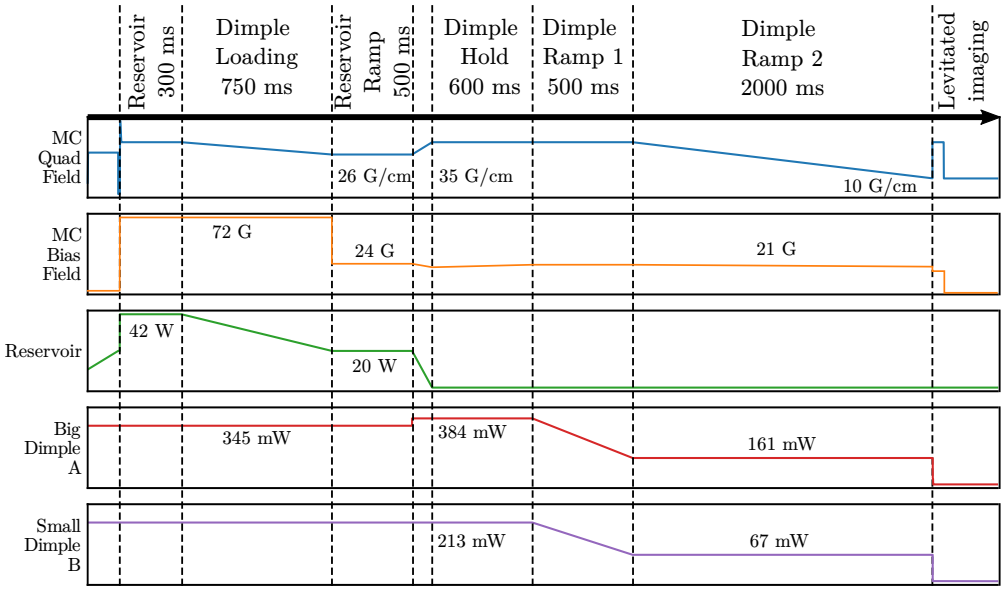

Figure 5.1: Experimental sequence for the formation of a Cs BEC.

Trap Frequency

The trap frequencies are associated with the motional frequencies of the atoms trapped in a harmonic potential. One of the method for trap frequency measurement is that we induce the atomic motion by a dynamic change of the trapping potential and observe the effect on the atom position. Here, we initiate the atom displacement using a magnetic field gradient. After the field is switched off for 1 ms while leaving atoms for a variable hold

time that the atoms are then released from the trap of interest. Then, an absorption image is acquired to determine the position of the centre-of-mass of the atomic cloud. The trap frequency is extracted from a sinusoidal fit with damping to the data. By measuring trap frequencies for different beams, the corresponding beam waist can be determined.

5.1.2 Magnetic Levitation

As a reservoir has a relatively low trap depth, due to the low trap depth of the reservoir trap, an additional potential due to gravity is dominated along the z (vertical) direction. To compensate the effect of gravity we apply a magnetic field gradient. In the vertical direction atoms in the dipole trap experience additional potential under an influence of magnetic field and gravity as follows

$$U_{tot} = U_{dipole} + U_{mag} + U_{grav} \tag{5.1}$$

The gravitational potential is linear with mass, where $U_{grav} = mgz$.

5.1.3 Dimple trap

Approximately 10% of the atoms from the reservoir are transferred to the dimple trap to increase the atomic density by evaporative cooling. The dimple trap is formed within the reservoir trap by crossing two tightly confined optical dipole traps in the horizontal plane. The laser beams are generated by 1064 nm laser which have waists of 51(1) μm and 103(2) μm. For optimised loading of the dimple trap, the scattering length of Cs atoms is kept to 1170 a_0 and then ramped down to 260 a_0 by applying the magnetic bias field of 72 G and then 24 G respectively. After 3.1 s hold time in the dimple trap, the atom number is $\sim 3 \times 10^4$. Forced evaporation is then performed towards BEC formation by ramping the power of the dimple beams in two stages with a duration of 8 ms. Simultaneously, the magnetic bias field is set to 23.4(1) G ($a_{\text{scatt}} \sim 330\ a_0$), where the ratio of elastic collisions and inelastic three-body collisions is efficient for evaporative cooling. At the end of evaporation, a pure BEC of 2×10^4 Cs atoms in the $|3, +3\rangle$ ground hyperfine state is created.

Chapter 6

Measurement of the tune-out wavelength for ^{133}Cs at 880 nm

Chapter 5 explains the recipe to produce the Cs Bose-Einstein condensate (BECs); therefore, we have a routine to make an ultrocold ensemble of Cs atoms to do the science. To make ultracold molecules, our experiment involves in trapping two species in the same dipole trap at some point. This requires us to design a non-straightforward strategy to trap both of them simultaneously due to their different dipole moment; hence experiencing different amount of force exerted by the trapping potential. Therefore, it motivates us to exploit the Cs BEC to measure its tune-out wavelength with a high precision.

This chapter is structured as follows. In Sec. 6.1 we review in details that precision measurement of tune-out wavelengths is important and beneficial to a wide range of physics applications especially in ultracold experiments. In Sec. 6.2 we discuss the theoretical calculations of polarisability including its decomposition into scalar, vector, and tensor components. We also explain how measurements of polarisability can be made using the Kapitza-Dirac scattering that results from applying a pulsed optical lattice potential to the atoms. In Sec. 6.3 we discuss the lattice setup used to measure λ_0 and present the results. In Sec. 6.4 we discuss how we extract the scalar tune-out wavelength from our measurements. We also discuss how the ratio of reduced matrix elements is extracted. We summarise the results and give an outlook

to future work in Sec. 6.5.

6.1 Motivation

Optical trapping is widely employed in experiments involving ultracold neutral atoms and molecules [38]. Optical fields can be engineered on the scale of the optical wavelength to produce various trapping geometries, including lattices [39], ring traps [40, 41], box potentials [42–44] and arrays of individual micro-traps [45, 46].

This, combined with the ability to confine any polarisable species, has resulted in numerous advances in metrology [47], control of single atoms and molecules [45, 46, 48–52], and quantum simulation of interacting many-body systems [53–56]. Refined optical trapping techniques can also lead to exciting developments that will underpin future quantum technologies [57–59].

The dipole force experienced by atoms in an optical trap is proportional to the dynamic polarisability. The polarisability varies with wavelength exhibiting poles, that tend to $\pm\infty$, whenever the wavelength of the applied optical field matches an atomic transition. This wavelength dependence gives additional control over the optical potential where, for ground state atoms, optical frequencies red detuned of a transition give rise to attractive optical potentials and those frequencies that are blue detuned give rise to repulsive optical potentials. These poles in the polarisability from transitions lead to wavelengths where the polarisability is zero and are referred to as tune-out wavelengths [60, 61] or magic-zero wavelengths [62]. Precise knowledge of the polarisability is of importance for various applications including optical lattice clocks, quantifying lattice potentials, and as benchmarks for testing theoretical methods of calculating polarisability for more complex atoms such as Er and Dy [62]. Measurements of tune-out wavelengths are important as they allow the determination of multiple atomic properties including transition dipole matrix elements, oscillator strengths, and state lifetimes [62, 63]. Transition dipole matrix elements are fundamental properties of atoms as well as being crucial parameters for determining, for example, the blackbody radiation shift of atoms which is often a limiting systematic uncertainty in

atomic clocks [64].

Tune-out wavelengths can also be used to create species-specific and state-specific optical trapping potentials [60, 61]. Species-specific traps occur due to different atomic species having different transition wavelengths. For different atomic species, the poles in the polarisability therefore occur at different wavelengths leading to different trapping potentials. Species-specific trapping is useful in multi-species experiments and has allowed for studies of scattering in mixed dimensions [65] and the transfer of entropy between different atomic species to demonstrate novel cooling schemes [66]. Within the same atomic species, atoms in different electronic states will experience different trapping potentials due to the different transition frequencies from the different states. Even within the same electronic state it is possible to engineer state-specific potentials as the polarisability also depends on the polarisation of the light interacting with the atom and the orientation of the atomic spin. The light polarisation and atomic spin will determine the transitions that are allowed by selection rules and hence make polarisability depend on both the total electronic angular momentum and its spin projection $|F, m_F\rangle$. In general, the polarisability is therefore composed into scalar, vector, and tensor polarisabilities where the scalar polarisability is the polarisability when averaging over all m_F levels. State-specific potentials can be used to engineer multi-particle entanglement [67], spatiotemporal control of intraspecies interactions [68], and state-selective manipulation of quantum states [69, 70].

Tune-out wavelengths have been experimentally measured both directly and indirectly. Direct measurements are made by performing polarisability measurements around the tune-out wavelength, with experimental techniques including atom diffraction [62], parameteric heating [70], and atom interferometry [71]. Indirect measurements can be made by inferring tune-out wavelengths from measurements of state lifetimes, but can be limited by knowledge of branching ratios [62].

Previous experiments have directly measured tune-out wavelengths, using linearly polarised light, for different alkali metal atoms including Li [72, 73], K [63, 74], and Rb [62, 66, 71, 75], as well as for other atomic species including He [76], Sr [70], and Dy [77] and also for ground state NaK mo-

lecules [78]. However, despite many theoretical studies of ^{133}Cs polarisability [79–82], so far no measurements of ^{133}Cs scalar tune-out wavelength have been performed. And yet ^{133}Cs atoms are used in a wide range of applications including the definition of the second [83], the search for variations in fundamental constants, and tests of the standard model.

6.2 Theory

6.2.1 Polarisability

Our experiments are performed using Cs atoms prepared in $|F = 3, m_F = +3\rangle$ in a magnetic field of 23.4(1) G. We calculate the polarisability including hyperfine structure following the methods described in detail elsewhere [79, 82, 84]. Below we summarise the main results.

The quantum state, $|i\rangle$, of an alkali atom can be defined in terms of the quantum numbers $|i\rangle = |\gamma, F, m_F\rangle \equiv |F, m_F\rangle$. $\mathbf{F} = \mathbf{I} + \mathbf{J}$, with $\mathbf{I}$ the nuclear spin, and $\mathbf{J}$ the electronic angular momentum. For Cs, the nuclear spin $I = 7/2$. γ represents the other quantum numbers used to define the state but we will drop γ from the notation for simplicity.

For an alkali atom in $|i\rangle$ interacting with light of wavelength λ, with associated angular frequency, ω,

the general form of the frequency dependent polarisability can be decomposed as [71]

$$\begin{aligned}\alpha_i(\omega) = \alpha_i^{(0)}(\omega) - \xi\hat{\mathbf{k}}\cdot\hat{\mathbf{B}}\frac{m_F}{2F}\alpha_i^{(1)}(\omega) \\ + \left[\frac{3(\hat{\boldsymbol{\epsilon}}\cdot\hat{\mathbf{B}})^2 - 1}{2}\right]\frac{3m_F^2 - F(F+1)}{F(2F-1)}\alpha_i^{(2)}(\omega).\end{aligned} \tag{6.1}$$

Here α_i^K are the scalar ($K = 0$), vector ($K = 1$), and tensor ($K = 2$) components of the polarisability, $\xi = (I_+ + I_-)/I_0$ is the fourth Stokes parameter [85] and quantifies the degree of circularity of the polarisation with $I_\pm$ being the intensities of the different circular components and I_0 is the total intensity, $\hat{\mathbf{B}}$ is a unit vector in the direction of the magnetic field, and $\hat{\boldsymbol{\epsilon}}$ and $\hat{\mathbf{k}}$ are unit vectors in the direction of the polarisation vector and wavevector,

respectively, of the light interacting with the atoms.

This scalar polarisability can be further decomposed into [86]

$$\alpha_i^{(0)}(\omega) = \alpha_{\text{core}} + \alpha_{\text{vc}} + \alpha_{\text{v},i}^{(0)}(\omega), \tag{6.2}$$

where there is a contribution to the polarisability from the core electrons, α_{core}, a core modification due to the valence electron, α_{vc}, and a contribution from the valence electron $\alpha_{\text{v},i}^{(0)}(\omega)$. The excitation frequencies of the core electrons are far detuned from the laser frequencies considered here and so α_{core} and α_{vc} are treated as frequency independent. Calculations in the random-phase approximation yield for Cs, $\alpha_{\text{core}} = 15.84(32) \times 4\pi\epsilon_0 a_0^3$ and $\alpha_{\text{vc}} = -0.673 \times 4\pi\epsilon_0 a_0^3$ [81].

The scalar polarisability contribution from the valence electrons is calculated by summing over contributions from all other states $|k\rangle = |F', m'_F\rangle$ [79]

$$\begin{aligned}\alpha_{\text{v},i}^{(0)}(\omega) = \frac{2}{\hbar}\frac{(2F+1)}{\sqrt{3(2F+1)}}\sum_{k\neq i}\frac{\omega_{k,i}|d_k|^2}{\omega_{k,i}^2-\omega^2}(-1)^{F'+F+1} \\ \times (2F'+1)\begin{Bmatrix} F & 1 & F' \\ 1 & F & 0 \end{Bmatrix}\begin{Bmatrix} F' & I & J' \\ J & 1 & F \end{Bmatrix}^2,\end{aligned} \tag{6.3}$$

where $\omega_{k,i} = \omega_k - \omega_i$ is the transition frequency between $|k\rangle$ and $|i\rangle$, $\hbar$ is the reduced Planck constant, $d_k = \langle J||d||J'\rangle$ is the reduced dipole matrix element between $|i\rangle$ and $|k\rangle$, and the terms in curly brackets are Wigner-6j symbols.

It can be observed from Eq. 6.3, that the scalar polarisability depends on the wavelengths of transitions from $|i\rangle$ that are allowed by electric dipole selection rules, and that the polarisability diverges at these transition frequencies. For ground state atoms red (blue) detuned frequencies leading to positive (negative) polarisability and hence attractive (repulsive) trapping potentials. For atoms in the ground state, there are scalar tune-out wavelengths between all pairs of transitions at a wavelength where the red-detuned contribution to the polarisability from one transition is cancelled by the blue detuned contribution from the other transition. Fig. 6.1 shows the calculated scalar polarisability of ground state Cs around the D_1 and D_2 transitions at 894.6 nm and 852.3 nm, respectively. Between these two trans-

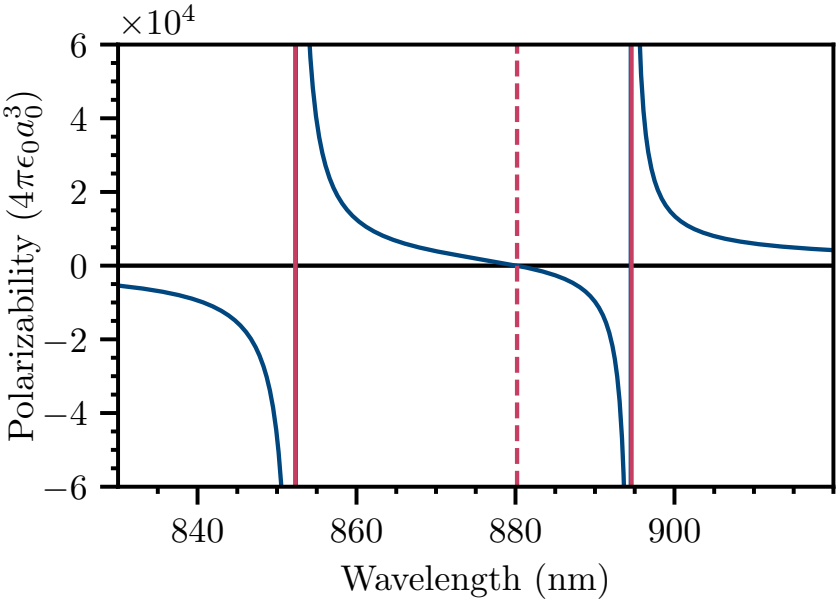

Figure 6.1: Calculated scalar polarisability of ground state Cs in the vicinity of the D_1, $6S_{1/2} \rightarrow 6P_{1/2}$, transition at 894.6 nm, and the D_2, $6S_{1/2} \rightarrow 6P_{3/2}$, transition at 852.3 nm. Between these two transitions the polarisability changes signs and passes through zero at the tune-out wavelength $\lambda_0 \approx$ 880 nm as indicated by the dashed line.

itions, the polarisability goes to zero at $\lambda_0 \approx 880$ nm. This is the tune-out wavelength that we measure in Sec. refsec:Analysis.

We now consider the impact of the vector and tensor polarisability terms in Eq. 6.1 on the value of the tune-out wavelength. The vector polarisability can cause substantial shifts to the tune-out wavelengths. The reason for this is selection rules for transitions. To illustrate the importance of these selection rules, we consider Cs atoms in the $|4, +4\rangle$ ground state. If the atoms interact with a pure σ^+ polarised light ($|\xi| = 1$) then transitions to the $6P_{1/2}$ state are not allowed by selection rules. This lack of coupling to the $6P_{1/2}$ state means that no tune-out wavelength will be present between the D_1 and D_2 lines for this specific light polarisation. For the case studied here of atoms in $|3, +3\rangle$, all polarisations can couple to both the $6P_{3/2}$ and $6P_{1/2}$ states but the position of the tune-out wavelength is still strongly influenced by the vector polarisability and can move on the order of ~ 10 nm. We observe from Eq. 6.1 that the vector polarisability contribution is

proportional to the ellipticity of the light as well as the term $\hat{\mathbf{k}} \cdot \hat{\mathbf{B}}$. We can therefore suppress the vector polarisability by ensuring the light polarisation is highly linear and aligning the laser beam orthogonal to the magnetic field, so that $\hat{\mathbf{k}} \cdot \hat{\mathbf{B}} \to 0$. Details of how this is achieved in our experiment are presented in Sec. **??**.

The tensor polarisability term is relevant to the measurements performed here. There is no contribution from the core electrons since the core is isotropic ($\alpha_i^{(2)} = \alpha_{v,i}^{(2)}$) [81]. In the absence of hyperfine structure, the tensor polarisability is zero for the ground state. However, including the hyperfine structure the tensor polarisability of $|i\rangle$ is non-zero, and can also be written as a sum over states as [79]

$$\begin{aligned}\alpha_{\mathrm{v},i}^{(2)}(\omega) = \frac{2}{\hbar}\sqrt{\frac{10F(2F-1)(2F+1)}{3(F+1)(2F+3))}}\sum_{k\neq i}\frac{\omega_{k,i}\left|d_k\right|^2}{\omega_{k,i}^2-\omega^2} \\ \times(-1)^{F+F'}(2F'+1)\begin{Bmatrix} F & 1 & F' \\ 1 & F & 2\end{Bmatrix}\begin{Bmatrix} F' & I & J' \\ J & 1 & F\end{Bmatrix}^2 .\end{aligned} \tag{6.4}$$

For the ground state alkali atoms the tensor term typically leads to corrections of less than a part-per-million. Therefore, the polarisability for linearly polarised light is dominated by contributions from the scalar polarisability but small corrections due to the tensor polarisability need to also be taken into account.

6.2.2 Kapitza-Dirac Scattering

Precision measurements of polarisability are difficult due to the need to determine the beam intensity accurately. However, measurements of wavelengths where the polarisability is zero are not influenced by accurate experimental determination of intensity. To measure these tune-out wavelengths, where the polarisability is zero, We use a Kapitza-Dirac scattering [87] to measure the trap depth of a lattice, and hence deduce the atomic polarisability. The Kapitza-Dirac scattering has been ubiquitously observed in many experiments. For instance, Gould et. al. [88] demonstrated it using a collimated beam of sodium atoms deflected by a standing-wave laser field due to a stimulated Compton scattering. The diffraction pattern of the

atomic waves results from the momentum transfer in even multiples ($2n$) of the photon's momentum. The probability for the atom to be in a momentum state $2n\hbar k_{\mathrm{L}}$ is the modulus-squared of the Fourier transform of the atomic wave function and found to be generally proportional to a Bessel function distribution [88, 89]. The experiment by [90] extended the use of the BECs to exhibit strong oscillations on the diffraction pattern. Interestingly, a spinor BEC subject to a pulsed optical lattice was proposed to realise a quantum random walk [91], which could be used as algorithms for quantum computing applications.

Kapitza-Dirac scattering is also routinely used in atomic physics experiments to measure optical lattice trap depths [92–94] and has previously been shown to be a useful tool for measuring tune-out wavelengths [75, 77]. The technique has been extended to measure low lattice depths by applying multiple pulses of the lattice potential to the atoms [62, 77].

Kapitza-Dirac scattering occurs when the lattice is pulsed onto a Bose-Einstein condensate (BEC) and atoms in the condensate undergo stimulated two-photon scattering events [90]. Photons are scattered from one lattice beam to the other and therefore momentum transfer occurs in units of $2\hbar k_{\mathrm{lat}}$, where k_{lat} is the lattice wavevector. The momentum transfer can occur in either direction along the beam to give both positive and negative momentum states. As the lattice pulse time is varied the population will oscillate between the different $2l\hbar k_{\mathrm{lat}}$ momentum states (l is an integer). The momentum states separate in a time-of-flight expansion after a lattice pulse allowing the populations to be measured and fitted to extract the corresponding lattice depth. In the Raman-Nath regime, the atomic motion during the lattice pulse can be neglected and analytic relations for the population dynamics can be used.

In the work studied here, we consider Kapitza-Dirac scattering beyond the Raman-Nath regime [94]. In this regime the pulses are no longer short compared to the oscillation period of atoms in the lattice. We therefore cannot use analytic relations for the different momentum state populations and a numerical model is required. The Hamiltonian for atoms of mass m in a periodic potential of depth V_0 and wavevector k_{lat} applied in the x direction

is given by

$$H = -\frac{\hbar^2}{2m}\frac{d^2}{dx^2} + V_0 \sin^2(k_{\text{lat}}x). \tag{6.5}$$

To calculate the populations in each momentum state, we diagonalise the Hamiltonian using a plane wave basis including both positive and negative orders up to $|l| = 20$. Convergence of solutions is found for $|l| > |l_{\text{max}}|$, where $|l_{\text{max}}|$ is the maximum observed occupied states. In the measurements performed here we observe populations up to $|l_{\text{max}}| = 5$. The evolution of all momentum states are fit simultaneously, with the $\pm|l|2\hbar k_{\text{lat}}$ averaged during fitting due to the symmetry of the scattering process to these momentum states. The atom numbers in each momentum state are determined by summing optical depths along the vertical lines of pixels of an absorption image and then normalised by the total number of atoms in each image to avoid issues from changes in atom number. The only free parameters in the fit are the lattice depth and the overall population amplitude.

6.3 Overview of the apparatus and BEC production

A schematic overview of our apparatus is shown in Fig. 6.2. Below we give brief details of the stages used to produce Cs BECs. We start with a high-flux source of laser-cooled atoms from a $2D^+$ magneto-optical trap (MOT). These atoms are collected in a 3D MOT in the center of a 12-port stainless steel chamber. After sub-Doppler molasses cooling, degenerate Raman sideband cooling [28] is performed which polarises the atoms into the $|F = 3, m_F = +3\rangle$ ground state and cools them to ~ 1 μK. To cool the atoms further we follow the method used to create the first BECs of Cs [12]. In this approach, we implement a large volume reservoir trap consisting of two beams with waists of ~ 500 μm at the atoms and crossing at an angle of 90 degrees. This light is derived from a broadband Ytterbium fiber laser (IPG Photonics) with a wavelength around 1070 nm. The trap is setup in a bowtie configuration where the power is recycled and used in both of the trapping beams, as shown in Fig. 6.2. This reservoir trap requires a magnetic levitation gradient to support the atoms against gravity.

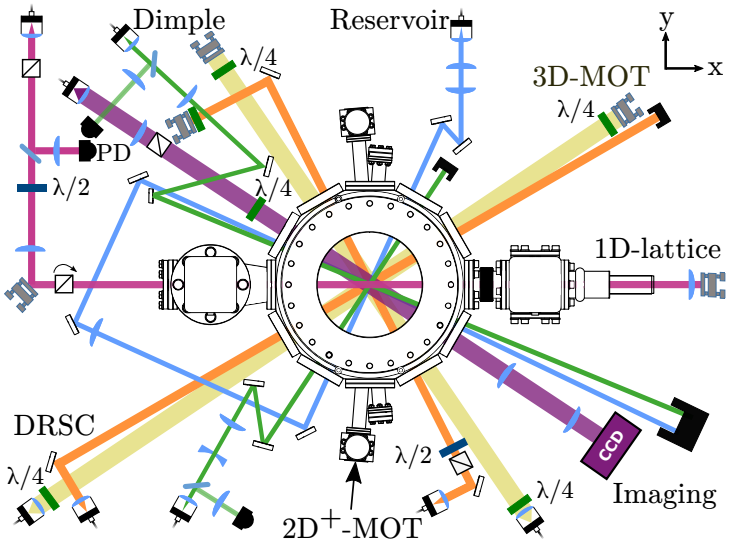

Figure 6.2: Schematic of the apparatus highlighting the optical beam layout in the x-y plane. All beams used for cooling, trapping, and imaging of atoms are shown. The 1D optical lattice used for measuring the polarisability is aligned along the x-direction (left-right in the diagram). Absorption imaging is performed at an angle of 33°with respect to the lattice direction. Electromagnetic coils (not shown) above and below the chamber provide a magnetic bias field in the vertical direction. The MOT and degenerate Raman sideband cooling beams in the z direction are not shown for clarity.

Approximately 10% of the atoms are then transferred from the reservoir trap into a tighter crossed optical dipole trap (xODT) at 1064 nm derived from a ND:YAG laser (Coherent, Mephisto). The two beams forming the trap have waists of 51(1) μm and 103(2) μm at the atoms. Forced evaporation is then performed by reducing the powers of these xODT beams whilst applying a bias field of 23.4(1) G to suppress the 3-body loss rate [12]. Typically, pure BECs containing 2×10^4 atoms in the $|3, +3\rangle$ ground hyperfine state are created.

The lattice light used for the Kapitza-Dirac measurements is generated from a tunable Ti:sapphire laser (M Squared, SolsTiS) pumped by a 18 W pump laser at 532 nm (Lighthouse Photonics, Sprout). Fig. 6.3 shows an optical setup for the light preparation. The light intensity sent to the experiment is controlled by an acousto-optical modulator (AOM) in a single-pass configuration that uses a fast RF switch (Mini-Circuits, ZASWA2-50DR-

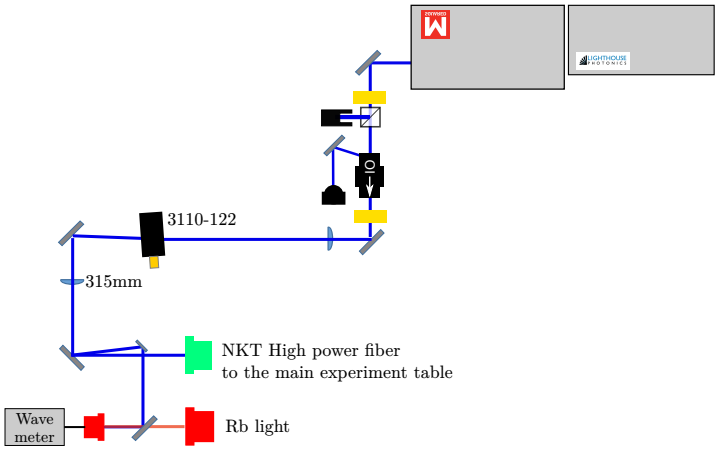

Figure 6.3: Schematic of the apparatus used to generate the lattice light on a separate laser table. The main laser is the Ti:sapphire laser from M Squared, SolsTiS. The light traverses a polarizing beam splitter and an isolator to achieve the horizontal polarization and protect the laser from a back reflection respectively. A single-pass AOM is used to shift a fixed frequency, mainly for fast intensity control before the light is coupled into one end of the high-power fiber. The other end is on the main experiment table (See Fig. 6.2. The zeroth-order light is picked off to compare its wavelength to the locked-reference light from Rb using a wavemeter for an accurate wavelength readout. (More details in texts)

FA+) to generate the short pulses required for the measurements. The light from the AOM is coupled into an optical fiber to avoid changes in the lattice alignment as the wavelength of the laser is adjusted. The power output of the fiber is monitored using a photodiode as shown in Fig. 6.2. This photodiode is used to correct for small power changes between polarisability measurements. Before passing through the vacuum chamber, the lattice light passes through a Glan-Laser polariser (Thorlabs, GL10-B). This polariser minimizes ξ and achieves a highly polarised lattice beam which is linearly polarised with an extinction ratio of better than 10^{-5}. The waist of the ingoing lattice beam is measured to be 99(5) μm at the position of the atoms. After the light has passed through the chamber, it is collimated and retro-reflected onto the atoms to create the lattice potential. The lattice laser frequency is measured via the pick-off zeroth order light and stabilised using a HighFinesse WS-U wavemeter with an absolute accuracy of 30 MHz. We reference the wave-

meter to the laser locked to the $5^2S_{1/2}(F = 2) \rightarrow 5^2P_{3/2}(F' = 3)$ transition in ^{87}Rb. Note that to achieve the accuracy of the wavemeter, either the lattice light or the Rb light is coupled to a single mode APC fiber connector to the non polished fiber that remains unplugged.

To perform the measurements of polarisability, the BEC is released from the dipole trap and after a 100 μs delay the lattice is pulsed on for a variable time. The atoms are then levitated using a magnetic field gradient of $\approx$ 30 G/cm and imaged after 40 ms allowing the different momentum peaks to separate spatially. Example images from these diffraction measurements are shown in Fig. 6.4 (a) for a lattice created using $\sim$ 300 mW of 881 nm light and for varying lattice pulse duration. Fig. 6.4 (b) shows the extracted populations of each of the momentum states for each of these images.

Birefringence in the viewports of the vacuum chamber can cause the highly linearly polarised light to acquire a circularly polarised component. In order to remove this effect, we perform separate measurements using two orthogonal linear polarisations [62]. By performing measurements in this way and averaging the measured tune-out wavelengths we can suppress any vector polarisability contribution caused by the vacuum viewports. We choose the two lattice polarisation alignments to be parallel and orthogonal to the applied magnetic field. This choice of orthogonal polarisations has the advantage that the changes in tune-out wavelength due to the tensor polarisability are less sensitive to alignment of the polarisation in these orientations.

We initially measure the trap depth of the lattice using a power of $\sim$ 300 mW. We measure trap depths for different lattice wavelengths and different orientations of the lattice polarisation with respect to the magnetic field. Fig. 6.5 (a) shows the results of these measurements. The data in Fig. 6.5 (a) is fit using Eq. 6.2. In the fit, the weighting of the polarisability contributions from the D_1 and D_2 transitions is a free parameter and the polarisability contributions from the other transitions is assumed to be wavelength independent over this range. The overall amplitude of the fit is also a fit parameter to convert from polarisability to trap depth.

To measure the tune-out wavelength, we increase the power to $\sim$ 1 W, increasing our sensitivity to small polarisabilities and allowing measurements

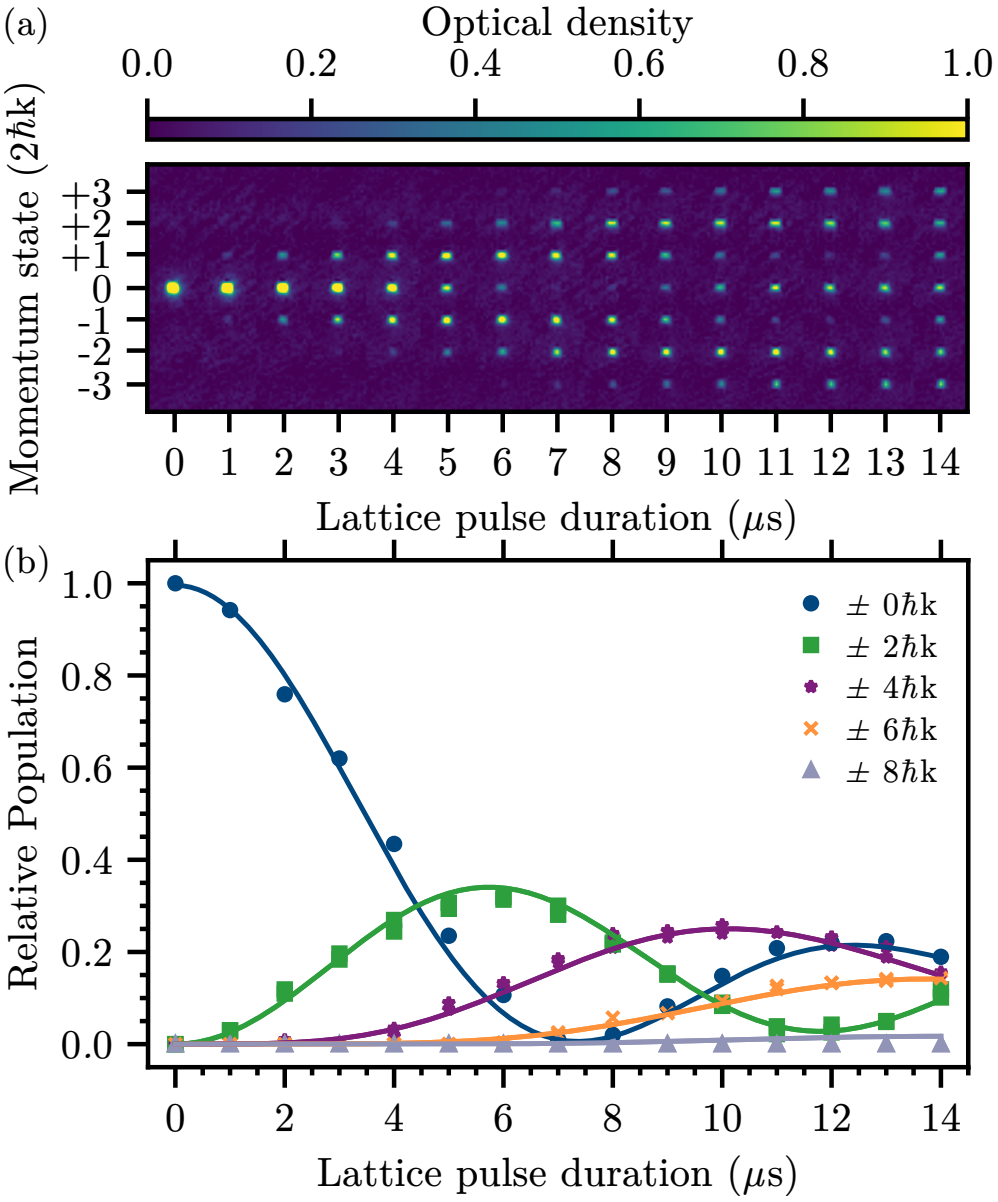

Figure 6.4: An example of a Kapitza-Dirac measurement for a lattice of power $P \sim 300$ mW, at 881 nm. (a) Absorption images of the different BEC momentum states for varying lattice pulse durations, measured after a 40 ms time-of-flight. (b) The relative atom number of the different diffracted momentum states are extracted from the images and fit using the method described in the text to give a trap depth of 4.96(2) μK.

to be made closer to λ_0. We then performed measurements of the trap depth over a $\sim$ 0.5 nm wavelength range centred on the tune-out wavelength, as shown in Fig. 6.5 (b). The polarisability can be extracted from the trap depth if the powers, beam waists and beam overlap are all known. However, to determine the tune-out wavelength only relative changes in polarisability are required if the lattice beam parameters remain constant. We therefore use the extracted trap depth to determine the tune-out wavelength.

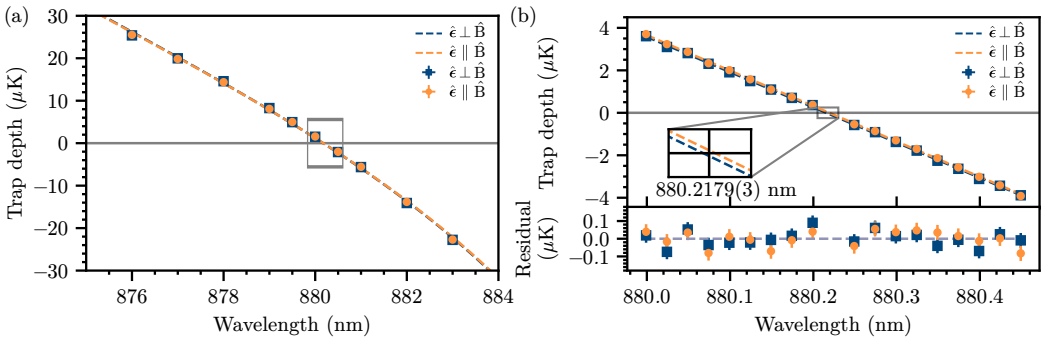

Figure 6.5: Trap depth measurements using Kapitza-Dirac scattering for polarisation vector, $\hat{\boldsymbol{\epsilon}}$, parallel (//, orange, circles) and perpendicular ($\perp$, blue, squares) to the magnetic field $\hat{\boldsymbol{B}}$. (a) A broad wavelength scan of trap depth using $P \sim 300$ mW. Dashed lines are fitted trap depths (see text for details). (b) Narrow wavelength scan across the range of wavelengths shown by the grey box in (a). Trap depths are measured using a lattice power of $P \sim 1$ W, and are fitted with straight line functions to extract tune-out wavelengths λ_0 for each polarisation. The residuals are plotted in the lower panel. The fitted tune-out wavelengths are $\lambda_0^{\perp} = 880.2164(6)$ nm and $\lambda_0^{//} = 880.2195(6)$ nm for lattice polarisations perpendicular and parallel to $\hat{\boldsymbol{B}}$, respectively. The difference in these values is highlighted in the inset of (b).

6.4 Analysis of results

In order to extract the tune-out wavelength, from the measurements shown in Fig. 6.5 (b), we first fit the data using a linear function which is a good approximation to the polarisability over this wavelength range. We separately fit the data for the orthogonal linear polarisations. The fits yield the

tune-out wavelengths of $\lambda_0^{\perp} = 880.2164(6)$ nm and $\lambda_0^{//} = 880.2195(6)$ nm, where $\perp(//)$ indicates that the linear polarisation of the lattice is orthogonal (parallel) to the magnetic field. To extract the scalar tune-out wavelength from these measurements we rely on some theoretical corrections detailed below.

6.4.1 Corrections to Measurements

The first correction that is taken into account is to remove the shifts from the tensor polarisability. From Eq. 6.1 we see that the shift depends on the relative orientation of the magnetic field and the polarisation of the lattice. Using Eq. 6.4, we determine the tensor shifts to be 473 fm when $\hat{\boldsymbol{\epsilon}} \cdot \hat{\mathbf{B}} = 1$ and -237 fm when $\hat{\boldsymbol{\epsilon}} \cdot \hat{\mathbf{B}} = 0$. We note that the uncertainties in these calculated values are irrelevant compared to our statistical uncertainty.

After applying this correction the tune-out wavelengths become $\lambda_0^{\perp} = 880.2166(6)$ nm and $\lambda_0^{//} = 880.2190(6)$ nm. The remaining difference between these two values comes from two factors: The first of these differences is statistical uncertainty where the two values agree at the 2σ level. The second difference can also come from any remaining vector polarisability. Any vector polarisability shift coming from the viewports can be cancelled by averaging the tune-out wavelength measurements from the two orthogonal polarisations, giving the result $\lambda_0 = 880.2178(4)$ nm.

The next correction we make is for the applied magnetic bias field. We calibrate this field using the known Cs Feshbach resonances up to 50 G [95]. We wish to extrapolate our measurements to the case of zero applied magnetic field. The shift is calculated following the method given in [71]. We consider only the transitions to the $6P_J$ states and calculate the shift to be 65(3) fm. Including transitions to the $7P_J$ states results in shifts of ~ 0.002 fm. Applying this correction gives the frequency-dependent scalar tune-out wavelength to be $\lambda_0 = 880.2179(4)$ nm where the error bar is purely statistical.

We must also include the systematic errors in our final result. The first systematic error comes from our wavelength measurement. The wavemeter has an uncertainty of 30 MHz corresponding to 78 fm at this wavelength. The

other major error comes from the vector polarisability which we calculate to have a conservative upper bound of 24 fm assuming we have aligned the lattice within 10 degrees of being orthogonal to the magnetic field quantization axis. This gives us the final result for the tune-out wavelength $\lambda_0 = 880.21790(40)_{\text{stat}}(8)_{\text{sys}}$ nm where we separate the statistical and systematic uncertainties.

There are a number of theoretical predictions for λ_0 [61, 80, 82]. However, only one of these theoretical values takes into account the hyperfine structure of the atoms [82] and gives a predicted tune-out wavelength of 880.20(5) nm. Our measured tune-out wavelength agrees well with this result.

6.4.2 Ratio of Matrix Elements

The error in the theoretical value of the tune-out wavelength is dominated by the ratio of the $6P$ matrix elements. We can use our measurements to extract a value for this ratio of $6P$ matrix elements where this ratio is defined as

$$R = \frac{\left|\left\langle 6P_{3/2}||d||6S_{1/2}\right\rangle\right|^2}{\left|\left\langle 6P_{1/2}||d||6S_{1/2}\right\rangle\right|^2} = \frac{|d_{6P_{3/2}}|^2}{|d_{6P_{1/2}}|^2} \quad . \tag{6.6}$$

When considering degeneracies of states only, this ratio is expected to be $R = 2$. However, including relativistic corrections, which are large for Cs compared to other alkali atoms due to the large atomic mass, this ratio is reduced with a theoretical value of $R = 1.984(10)$ [82].

Table 6.1 shows the contributions to the frequency dependent scalar polarisability at the theoretical tune-out wavelength, between the D line transitions, of $\lambda_0^{\text{th}} = 880.2456$ nm. To determine λ_0^{th}, we use the matrix elements given in Table 6.1 which come from a mixture of both experimentally measured and theoretically calculated values. From the table it can be seen that the main contributions to the polarisability at this tune-out wavelength are from the transitions to the $6P_{1/2}$ and $6P_{3/2}$ states, with the other values constant around this value. Therefore by adjusting the ratio R the theoretical value of the tune-out wavelength can be adjusted to agree with the measured value.

In order to determine this ratio of matrix elements, the scalar polarisability can be expressed in the following form [71]

$$\alpha^{(0)}_{6S_{1/2}}(\omega) = \alpha_{\text{offset}} + \left|d_{6P_{1/2}}\right|^2 \left(K_{6P_{1/2}} + K_{6P_{3/2}}R\right), \tag{6.7}$$

where $\alpha_{\text{offset}} = 17.5(3) \times 4\pi\epsilon_0 a_0^3$ includes all contributions to the scalar polarisability that are not from the $6P_{1/2}$ and $6P_{3/2}$ states. $K_{6P_J} = \alpha^{(0)}_{6P_J}/|d_{6P_J}|^2$ where $\alpha^{(0)}_{6P_J}$ are the polarisability contributions to the $6S$ state from the $6P_J$ states.

Setting $\alpha = 0$ in Eq. 6.7 and using our experimentally measured value for the tune-out wavelength we extract the ratio $R = 1.9808(2)$. The error in R contains contributions from $d_{6P_{1/2}}$, α_{offset} and the determination of the tune-out wavelength. However, the dominant contribution comes from the calculation of the α_{core}. Using the experimentally measured values of the $6P_J$ states given in Table 6.1, the value of the ratio is $R = 1.984(4)$ which agrees well with our value extracted from the measured tune-out wavelength.

6.5 Summary and Outlook

We have used Kapitza-Dirac scattering of atoms from a standing wave of light to measure the tune-out wavelength of Cs in the ground hyperfine state, $|F = 3, m_F = 3\rangle$, around 880 nm between the D_1 and D_2 transitions. We are able to eliminate the influence of the vector Stark shift by using linearly polarised light and performing the measurements for orthogonal polarisation. By correcting the measured wavelength to remove the influence of the tensor polarisability and magnetic field, we find the scalar tune-out wavelength to be $880.21790(40)_{\text{stat}}(8)_{\text{sys}}$ nm. This is in good agreement with theoretical value of 880.20(5) nm from [82].

We have used this measurement to determine the ratio of the reduced matrix elements for transitions from the ground state to the $6P_J$ states. We have found this ratio to be $R = 1.9808(2)$ which is consistent with previous measurements and with a reduction in the error by a factor of more than 10. This ratio of reduced matrix elements is also important for determining other atomic properties such as oscillator strengths, and state lifetimes.

Table 6.1: The theoretical contributions to the $6S$ scalar polarisability of Cs at $\lambda_0^{th} = 880.2456$ nm. polarisability contributions are given in units of $(4\pi\epsilon_0 a_0^3)$. Uncertainties are given in parentheses. Experimental energies ΔE are measured from the ground state and given in cm^{-1} [96]. The reduced electric-dipole matrix elements d in atomic units are from experimental and theoretical data.

State	$\Delta E(\mathrm{cm}^{-1})$	d (ea_0)	$\alpha^{(0)}$ (at λ_0^{th})	Ref.
$6P_{1/2}$	11178.26816	4.498(6)	-4029(11)	[97]
$7P_{1/2}$	21765.348	0.2781(5)	0.3573(12)	[98]
$8P_{1/2}$	25708.8547	0.092(10)	0.030(7)	[81]
$9P_{1/2}$	27636.9966	0.043(7)	0.006(2)	[81]
$10P_{1/2}$	28726.8123	0.0248(5)	0.0019(8)	[81]
$11P_{1/2}$	29403.42310	0.0162(4)	0.0008(4)	[81]
$12P_{1/2}$	29852.43153	0.012(3)	0.0004(2)	[81]
$6P_{3/2}$	11732.3071	6.335(5)	4011(6)	[99]
$7P_{3/2}$	21946.397	0.5742(6)	1.501(3)	[98]
$8P_{3/2}$	25791.508	0.232(14)	0.19(2)	[81]
$9P_{3/2}$	27681.6782	0.130(10)	0.053(8)	[81]
$10P_{3/2}$	28753.6769	0.086(7)	0.022(4)	[81]
$11P_{3/2}$	29420.824	0.063(6)	0.011(2)	[81]
$12P_{3/2}$	29864.345	0.049(5)	0.0068(13)	[81]
$n > 12$			0.16(16)	
α_{core}			15.84(16)	[81]
α_{vc}			-0.67(20)	[81]
α_{offset}			17.5(3)	[81]
Total			0(13)	[81]

The measurement of this tune-out wavelength will be useful in future studies of atomic mixtures involving Cs. For example, using a stirring beam to create vortices in only one of the species trapped. Future work can also include measuring further tune-out wavelengths for Cs to put restraints on further dipole matrix elements. Such measurements are also more sensitive to changes in α_{core} and together these measurements can aim to put further restraints on this parameter [74].

Bibliography

[1] T. Köhler, K. Góral and P. S. Julienne, "Production of cold molecules via magnetically tunable Feshbach resonances", Rev. Mod. Phys. **78**, 1311–1361 (2006) (cited on page 1).

[2] D. DeMille, J. M. Doyle and A. O. Sushkov, "Probing the frontiers of particle physics with tabletop-scale experiments", Science **357**, 990–994 (2017) (cited on page 1).

[3] R. Barnett, D. Petrov, M. Lukin and E. Demler, "Quantum Magnetism with Multicomponent Dipolar Molecules in an Optical Lattice", Phys. Rev. Lett. **96**, 190401 (2006) (cited on page 1).

[4] M. A. Baranov, A Micheli, S Ronen and P Zoller, "Bilayer superfluidity of fermionic polar molecules: Many-body effects", Phys. Rev. A **83**, 43602 (2011) (cited on pages 1–2).

[5] P. A. Lee, N. Nagaosa and X.-G. Wen, "Doping a Mott insulator: Physics of high-temperature superconductivity", Reviews of Modern Physics **78**, 17–85 (2006) (cited on page 1).

[6] J. L. Bohn, A. M. Rey and J. Ye, "Cold molecules: Progress in quantum engineering of chemistry and quantum matter", Science **357**, 1002–1010 (2017) (cited on page 1).

[7] N. R. Cooper and G. V. Shlyapnikov, "Stable Topological Superfluid Phase of Ultracold Polar Fermionic Molecules", Physical Review Letters **103**, 155302 (2009) (cited on pages 1–2).

[8] B. Sundar, B. Gadway and K. R. Hazzard, "Synthetic dimensions in ultracold polar molecules", Scientific Reports **8**, 10.1038/s41598-018-21699-x (2018) (cited on page 1).

[9] A Pikovski, M Klawunn, G. V. Shlyapnikov and L Santos, "Interlayer Superfluidity in Bilayer Systems of Fermionic Polar Molecules", Phys. Rev. Lett. **105**, 215302 (2010) (cited on page 2).

[10] W. Ketterle, D. S. Durfee and D. M. Stamper-Kurn, "Making, probing and understanding Bose-Einstein condensates", (1999) (cited on pages 2–3).

[11] A. Ratkata, "A Two-Species Magneto-Optical Trap Using $ˆ{39}\mathrm{K}$ and $ˆ{133}\mathrm{Cs}$", PhD thesis (Durham University, 2017) (cited on page 5).

[12] T. Weber, J. Herbig, M. Mark, H. C. Nägerl and R. Grimm, "Bose-Einstein condensation of cesium", Science **299**, 232–235 (2003) (cited on pages 7, 61, 73–74).

[13] T. Kraemer, J. Herbig, M. Mark, T. Weber, C. Chin, H. C. Nägerl and R. Grimm, "Optimized production of a cesium Bose-Einstein condensate", Applied Physics B: Lasers and Optics **79**, 1013–1019 (2004) (cited on page 7).

[14] D. J. Mccarron, "A Quantum Degenerate Mixture of 87 Rb and 133 Cs", PhD thesis (2011) (cited on pages 7, 51, 53).

[15] R. Pires, J. Ulmanis, S. Häfner, M. Repp, A. Arias, E. D. Kuhnle and M. Weidemüller, "Observation of Efimov resonances in a mixture with extreme mass imbalance", Physical Review Letters **112**, 10.1103/PhysRevLett.112.250404 (2014) (cited on page 7).

[16] A. Guttridge, "Photoassociation of Ultracold CsYb Molecules and Determination of Interspecies Scattering Lengths Photoassociation of Ultracold CsYb Molecules and Determination of Interspecies Scattering Lengths", PhD thesis (Durham University, 2018) (cited on pages 7–8, 26, 38, 44–45, 61–62).

[17] K. Dieckmann, R. J. Spreeuw, M. Weidemüller and J. T. M Walraven, "Two-dimensional magneto-optical trap as a source of slow atoms", Physical Review A - Atomic, Molecular, and Optical Physics **58**, 10.1016/S0030-4018(98)00499-4 (1998) (cited on pages 7, 29).

[18] M. W. Gempel, T. Hartmann, T. A. Schulze, K. K. Voges, A. Zenesini and S. Ospelkaus, "Versatile electric fields for the manipulation of ultracold NaK molecules", New Journal of Physics **18**, 10.1088/1367-2630/18/4/045017 (2016) (cited on pages 16, 18–19).

[19] K. L. Butler, "A dual species MOT of Yb and Cs A dual species MOT of Yb and Cs", Thesis (2014) (cited on page 20).

[20] M Gröbner, P Weinmann, F Meinert, K Lauber, E Kirilov and H.-C. Nägerl, "A new quantum gas apparatus for ultracold mixtures of K and Cs and KCs ground-state molecules", Journal of Modern Optics **63**, 1829–1839 (2016) (cited on page 21).

[21] A. L. Marchant, S. Händel, T. P. Wiles, S. A. Hopkins, C. S. Adams and S. L. Cornish, "Off-resonance laser frequency stabilization using the Faraday effect", Optics Letters **36**, 64 (2011) (cited on pages 23, 50, 56–57).

[22] T. Pyragius, "Developing and building an absorption imaging system for Ultracold Atoms", 1–28 (2012) (cited on pages 26, 28).

[23] P. Tierney, "Magnetic Trapping of an Ultracold 87 Rb - 133 Cs Atomic Mixture Magnetic Trapping of an Ultracold 87 Rb - 133 Cs Atomic Mixture", PhD thesis (2009) (cited on page 28).

[24] Bastian Hoeltkemeier, "2D MOT as a source of a cold atom target", PhD thesis (2011), page 84 (cited on pages 30, 32).

[25] H. Busche, "Efficient loading of a magneto-optical trap for experiments with dense ultracold Rydberg gases", PhD thesis (University of Heidelberg, 2012) (cited on page 30).

[26] K. Brugger et al., "Nanofabricated atom optics: Atom chips", Journal of Modern Optics **47-14**, 2789–2809 (2000) (cited on page 31).

[27] D. W. Sesko and C. E. Wieman, "Behavior of neutral atoms in a spontaneous force trap", Collected Papers of Carl Wieman **8**, 281–293 (1991) (cited on page 38).

[28] A. J. Kerman, V. Vuletić, C. Chin and S. Chu, "Beyond optical molasses: 3D raman sideband cooling of atomic cesium to high phase-space density", Physical Review Letters **84**, 439–442 (2000) (cited on pages 38, 40–42, 50, 73).

[29] C. Braun, "Implementation of a Raman Sideband Cooling for 87Rb", PhD thesis (2015) (cited on pages 43–44).

[30] G. E Marti, D. M Kurn, M. Inguscio, W. Ketterle and S. Stringari, *Quantum Matter at Ultralow Temperatures* (2016), page 570 (cited on page 45).

[31] K. Pilch, "Optical trapping and Feshbach spectroscopy of an ultracold Rb-Cs mixture", PhD thesis (2009) (cited on pages 48, 51).

[32] A. Lercher, "Doppel-Spezies Bose-Einstein-Kondensat von Rubidium und Caesium Atomen in raeumlich getrennten optischen Fallen", PhD thesis (2010) (cited on page 48).

[33] KAUSHAL SK and WETHERILL GW, "Rubidium 87- strontium 87 age of carbonaceous chondrites", J Geophys Res **75**, 463–468 (1970) (cited on page 50).

[34] J. Appel, A. MacRae and A. I. Lvovsky, "A versatile digital GHz phase lock for external cavity diode lasers", Measurement Science and Technology **20**, 10.1088/0957-0233/20/5/055302 (2009) (cited on pages 50, 52).

[35] L. Antunes, "Constructing an Optical Phase-Locked Loop for Partial-Transfer Imaging of Bose-Einstein Condensates", PhD thesis (2014) (cited on pages 50, 52).

[36] P. Siddons, C. S. Adams and I. G. Hughes, "Optical control of Faraday rotation in hot Rb vapor", Physical Review A - Atomic, Molecular, and Optical Physics **81**, 10.1103/PhysRevA.81.043838 (2010) (cited on page 56).

[37] S. L. Kemp, I. G. Hughes and S. L. Cornish, "An analytical model of off-resonant Faraday rotation in hot alkali metal vapours", Journal of Physics B: Atomic, Molecular and Optical Physics **44**, 0–6 (2011) (cited on page 56).

[38] R. Grimm, M. Weidemüller and Y. B. Ovchinnikov, "Optical dipole traps for neutral atoms", in , Vol. 42, edited by B. Bederson and H. Walther, Advances In Atomic, Molecular, and Optical Physics (Academic Press, 2000), pages 95 –170 (cited on page 66).

[39] I. Bloch, "Ultracold quantum gases in optical lattices", Nature Physics **1**, 3517 (2005) (cited on page 66).

[40] A. Ramanathan et al., "Superflow in a toroidal bose-einstein condensate: An atom circuit with a tunable weak link", Phys. Rev. Lett. **106**, 130401 (2011) (cited on page 66).

[41] S. Moulder, S. Beattie, R. P. Smith, N. Tammuz and Z. Hadzibabic, "Quantized supercurrent decay in an annular Bose-Einstein condensate", Phys. Rev. A **86**, 013629 (2012) (cited on page 66).

[42] A. L. Gaunt, T. F. Schmidutz, I. Gotlibovych, R. P. Smith and Z. Hadzibabic, "Bose-Einstein condensation of atoms in a uniform potential", Phys. Rev. Lett. **110**, 200406 (2013) (cited on page 66).

[43] B. Mukherjee, Z. Yan, P. B. Patel, Z. Hadzibabic, T. Yefsah, J. Struck and M. W. Zwierlein, "Homogeneous Atomic Fermi Gases", Phys. Rev. Lett. **118**, 123401 (2017) (cited on page 66).

[44] R. Bause et al., "Collisions of ultracold molecules in bright and dark optical dipole traps", (2021) (cited on page 66).

[45] S. Ebadi et al., "Quantum Phases of Matter on a 256-Atom Programmable Quantum Simulator", (2020) (cited on page 66).

[46] P. Scholl et al., "Programmable quantum simulation of 2D antiferromagnets with hundreds of rydberg atoms", arXiv:2012.12268 (2020) (cited on page 66).

[47] A. D. Ludlow, M. M. Boyd, J. Ye, E. Peik and P. O. Schmidt, "Optical atomic clocks", Rev. Mod. Phys. **87**, 637–701 (2015) (cited on page 66).

[48] N. Schlosser, G. Reymond, I. Protsenko and P. Grangier, "Sub-poissonian loading of single atoms in a microscopic dipole trap", Nature **411**, 1024–1027 (2001) (cited on page 66).

[49] M. A. Norcia, A. W. Young and A. M. Kaufman, "Microscopic Control and Detection of Ultracold Strontium in Optical-Tweezer Arrays", Physical Review X **8**, 41054 (2018) (cited on page 66).

[50] A. Cooper, J. P. Covey, I. S. Madjarov, S. G. Porsev, M. S. Safronova and M. Endres, "Alkaline-Earth Atoms in Optical Tweezers", Phys. Rev. X **8**, 41055 (2018) (cited on page 66).

[51] L. R. Liu, J. D. Hood, Y. Yu, J. T. Zhang, N. R. Hutzler, T. Rosenband and K. K. Ni, "Building one molecule from a reservoir of two atoms", Science **360**, 900–903 (2018) (cited on page 66).

[52] L. Anderegg, L. W. Cheuk, Y. Bao, S. Burchesky, W. Ketterle, K. K. Ni and J. M. Doyle, "An optical tweezer array of ultracold molecules", Science **365**, 1156–1158 (2019) (cited on page 66).

[53] I. Bloch, J. Dalibard and W. Zwerger, "Many-body physics with ultracold gases", Rev. Mod. Phys. **80**, 885–964 (2008) (cited on page 66).

[54] M. Lewenstein, A. Sanpera and V. Ahufinger, *Ultracold atoms in optical lattices* (Oxford University Press, 2012) (cited on page 66).

[55] I. Bloch, J. Dalibard and S. Nascimbène, "Quantum simulations with ultracold quantum gases", Nature Physics **8**, 267–276 (2012) (cited on page 66).

[56] C. Gross and I. Bloch, "Quantum simulations with ultracold atoms in optical lattices", Science **357**, 995–1001 (2017) (cited on page 66).

[57] L. Amico *et al.*, "State of the art and perspective on Atomtronics", (2020) (cited on page 66).

[58] D. Awschalom *et al.*, "Development of quantum interConnects (QuICs) for Next-Generation information technologies", Physical Review X Quantum **2**, 017002 (2021) (cited on page 66).

[59] E. Altman *et al.*, "Quantum simulators: Architectures and opportunities", Physical Review X Quantum **2**, 017003 (2021) (cited on page 66).

[60] L. J. Leblanc and J. H. Thywissen, "Species-specific optical lattices", Phys. Rev. A **75**, 053612 (2007) (cited on pages 66–67).

[61] B. Arora, M. S. Safronova and C. W. Clark, "Tune-out wavelengths of alkali-metal atoms and their applications", Physical Review A - Atomic, Molecular, and Optical Physics **84**, 10.1103/PhysRevA.84.043401 (2011) (cited on pages 66–67, 80).

[62] C. D. Herold, V. D. Vaidya, X. Li, S. L. Rolston, J. V. Porto and M. S. Safronova, "Precision measurement of transition matrix elements via light shift cancellation", Phys. Rev. Lett. **109**, 243003 (2012) (cited on pages 66–67, 72, 76).

[63] R. Trubko, M. D. Gregoire, W. F. Holmgren and A. D. Cronin, "Potassium tune-out-wavelength measurement using atom interferometry and a multipass optical cavity", Phys. Rev. A **95**, 052507 (2017) (cited on pages 66–67).

[64] T. L. Nicholson et al., "Systematic evaluation of an atomic clock at 2×10^{-18} total uncertainty", Nat. Commun. **6**, 6896– (2015) (cited on page 67).

[65] G. Lamporesi, J. Catani, G. Barontini, Y. Nishida, M. Inguscio and F. Minardi, "Scattering in mixed dimensions with ultracold gases", Phys. Rev. Lett. **104**, 153202 (2010) (cited on page 67).

[66] J. Catani, G. Barontini, G. Lamporesi, F. Rabatti, G. Thalhammer, F. Minardi, S. Stringari and M. Inguscio, "Entropy exchange in a mixture of ultracold atoms", Phys. Rev. Lett. **103**, 140401 (2009) (cited on page 67).

[67] O. Mandel, M. Greiner, A. Widera and T. Rom, "Controlled collisions for multi- particle entanglement of optically trapped atoms", Nature **425**, 937–940 (2003) (cited on page 67).

[68] L. W. Clark, L.-C. Ha, C.-Y. Xu and C. Chin, "Quantum Dynamics with Spatiotemporal Control of Interactions in a Stable Bose-Einstein Condensate", Phys. Rev. Lett. **115**, 155301 (2015) (cited on page 67).

[69] Y. Wang, X. Zhang, T. A. Corcovilos, A. Kumar and D. S. Weiss, "Coherent Addressing of Individual Neutral Atoms in a 3D Optical Lattice", Phys. Rev. Lett. **115**, 043003 (2015) (cited on page 67).

[70] A. Heinz, A. J. Park, N. Šantić, J. Trautmann, S. G. Porsev, M. S. Safronova, I. Bloch and S. Blatt, "State-Dependent Optical Lattices for the Strontium Optical Qubit", Phys. Rev. Lett. **124**, 203201 (2020) (cited on page 67).

[71] R. H. Leonard, A. J. Fallon, C. A. Sackett and M. S. Safronova, "High-precision measurements of the ^{87}Rb D-line tune-out wavelength", Phys. Rev. A **92**, 052501 (2015) (cited on pages 67–68, 79, 81).

[72] E. Copenhaver, K. Cassella, R. Berghaus and H. Müller, "Measurement of a ^{7}Li tune-out wavelength by phase-patterned atom interferometry", Phys. Rev. A **100**, 063603 (2019) (cited on page 67).

[73] B Décamps, J Vigué, A Gauguet and M Büchner, "Measurement of the 671-nm tune-out wavelength of ^{7}Li by atom interferometry", Phys. Rev. A **101**, 033614 (2020) (cited on page 67).

[74] W. F. Holmgren, R. Trubko, I. Hromada and A. D. Cronin, "Measurement of a wavelength of light for which the energy shift for an atom vanishes", Phys. Rev. Lett. **109**, 243004 (2012) (cited on pages 67, 83).

[75] F. Schmidt, D. Mayer, M. Hohmann, T. Lausch, F. Kindermann and A. Widera, "Precision measurement of the ^{87}Rb tune-out wavelength in the hyperfine ground state F=1 at 790 nm", Phys. Rev. A **93**, 022507 (2016) (cited on pages 67, 72).

[76] B. M. Henson, R. I. Khakimov, R. G. Dall, K. G. Baldwin, L. Y. Tang and A. G. Truscott, "Precision Measurement for Metastable Helium Atoms of the 413 nm Tune-Out Wavelength at Which the Atomic Polarizability Vanishes", Phys. Rev. Lett. **115**, 043004 (2015) (cited on page 67).

[77] W. Kao, Y. Tang, N. Q. Burdick and B. L. Lev, "Anisotropic dependence of tune-out wavelength near Dy 741-nm transition", Optics Express **25**, 3411 (2017) (cited on pages 67, 72).

[78] R. Bause, M. Li, A. Schindewolf, X. Y. Chen, M. Duda, S. Kotochigova, I. Bloch and X. Y. Luo, "Tune-Out and Magic Wavelengths for Ground-State ^{23}Na^{40}K Molecules", Phys. Rev. Lett. **125**, 23201 (2020) (cited on page 68).

[79] F. Le Kien, P. Schneeweiss and A. Rauschenbeutel, "Dynamical polarizability of atoms in arbitrary light fields: General theory and application to cesium", Eur. Phys. J. D **67**, 92 (2013) (cited on pages 68–69, 71).

[80] W. W. Yu, R. M. Yu, Y. J. Cheng and Y. J. Zhou, "Tune-out wavelengths for the alkaline-metal atoms", Chin. Phys. B **25**, 023101 (2016) (cited on pages 68, 80).

[81] M. S. Safronova, U. I. Safronova and C. W. Clark, "Magic wavelengths, matrix elements, polarizabilities, and lifetimes of Cs", Phys. Rev. A **94**, 012505 (2016) (cited on pages 68–69, 71, 82).

[82] J. Jiang, X. J. Li, X. Wang, C. Z. Dong and Z. W. Wu, "Tune-out wavelengths of the hyperfine components of the ground level of Cs 133 atoms", Phys. Rev. A **102**, 042823 (2020) (cited on pages 68, 80–81).

[83] L. Essen and J. Parry, "An atomic standard of frequency and time interval: a caesium resonator", Nature **176**, 280–282 (1955) (cited on page 68).

[84] M. S. Safronova, B. Arora and C. W. Clark, "Frequency-dependent polarizabilities of alkali-metal atoms from ultraviolet through infrared spectral regions", Phys. Rev. A **73**, 022505 (2006) (cited on page 68).

[85] M. Auzinsh, D. Budker and S. M. Rochester, *Optically Polarized Atoms* (Oxford University Press, 2010) (cited on page 68).

[86] M. S. Safronova, W. R. Johnson and A Derevianko, "Relativistic many-body calculations of energy levels, hyperfine constants, electric-dipole matrix elements, and static polarizabilities for alkali-metal atoms", Phys. Rev. A **60**, 4476–4487 (1999) (cited on page 69).

[87] P. L. Kapitza and P. A. M. Dirac, "The reflection of electrons from standing light waves", Proc. Cambridge Phil. Soc. **29**, 297–300 (1933) (cited on page 71).

[88] P. L. Gould, G. A. Ruff and D. E. Pritchard, "Diffraction of atoms by light: the near-resonant kapitza-dirac effect", Physical Review Letters **56**, 827–830 (1986) (cited on pages 71–72).

[89] C. S. Adams, M Sigel and J Mlynek, "Atom optics", Physics Reports **240**, 143–210 (1994) (cited on page 72).

[90] Y. B. Ovchinnikov, J. H. Müller, M. R. Doery, E. J. D. Vredenbregt, K Helmerson, S. L. Rolston and W. D. Phillips, "Diffraction of a released bose-einstein condensate by a pulsed standing light wave", Physical Review Letters **83**, 284–287 (1999) (cited on page 72).

[91] G. Summy and S. Wimberger, "Quantum random walk of a Bose-Einstein condensate in momentum space", Physical Review A **93**, 23638 (2016) (cited on page 72).

[92] J. Hecker Denschlag et al., "A Bose-Einstein condensate in an optical lattice", J. Phys. B: At. Mol. Opt. Phys. **35**, 3095–3110 (2002) (cited on page 72).

[93] K. Viebahn, M. Sbroscia, E. Carter, J. C. Yu and U. Schneider, "Matter-Wave Diffraction from a Quasicrystalline Optical Lattice", Phys. Rev. Lett. **122**, 110404 (2019) (cited on page 72).

[94] B. Gadway, D. Pertot, R. Reimann, M. G. Cohen and D. Schneble, "Analysis of Kapitza-Dirac diffraction patterns beyond the Raman-Nath regime", Optics Express **17**, 19173 (2009) (cited on page 72).

[95] C. Chin, V. Vuletić, A. J. Kerman, S. Chu, E. Tiesinga, P. J. Leo and C. J. Williams, "Precision Feshbach spectroscopy of ultracold Cs_2", Phys. Rev. A **70**, 032701 (2004) (cited on page 79).

[96] J. E. Sansonetti, "Wavelengths, transition probabilities, and energy levels for the spectra of cesium (Cs I-Cs LV)", J. Phys. Chem. Ref. Data **38**, 761–923 (2009) (cited on page 82).

[97] R. J. Rafac, C. E. Tanner, A. E. Livingston and H. G. Berry, "Fast-beam laser lifetime measurements of the cesium $6p^2P_{1/2,3/2}$ states", Phys. Rev. A **60**, 3648–3662 (1999) (cited on page 82).

[98] A. Damitz, G. Toh, E. Putney, C. E. Tanner and D. S. Elliott, "Measurement of the radial matrix elements for the $6s^2S_{1/2} \rightarrow 7p^2P_J$ transitions in cesium", Phys. Rev. A **99**, 1–11 (2019) (cited on page 82).

[99] B. M. Patterson, J. F. Sell, T. Ehrenreich, M. A. Gearba, G. M. Brooke, J. Scoville and R. J. Knize, "Lifetime measurement of the cesium $6P_{3/2}$ level using ultrafast pump-probe laser pulses", Phys. Rev. A **91**, 012506 (2015) (cited on page 82).